



Tomas Bata University
Faculty of Technology

Doctoral Thesis

**Testing of Pressure Sensitive Adhesives
for Transdermal Therapeutic Systems**

**Testování adheziv v transdermálních terapeutických
materiálech**

Michael Meurer

Zlín 2024

Doctoral study program

P3909 Process Engineering

Degree course

3909V013 Tools and Processes

Supervisor: Prof. Ing. Berenika Hausnerová, Ph.D.

Consultant: Prof. Dr.-Ing. Bernhard Möglinger

© Meurer, Michael

Published by Tomas Bata University in Zlin in the Edition Doctoral Thesis

The publication was submitted in the year 2023

The defense was scheduled for January 2024

Keywords: adhesion, rheology, pressure sensitive adhesives, transdermal therapeutic systems, diffusion

Klíčová slova: adheze, reologie, tlakově senzitivní adheziva, transdermální terapeutické materiály, difúze

Resume

Traditional and newly developed testing methods were used for extensive application-related characterization of transdermal therapeutic systems (TTS) and pressure sensitive adhesives (PSA). Large amplitude oscillatory shear measurements of PSAs were correlated to the material behavior during the patient's motion and showed that all PSAs were located close to the gel point. Furthermore, an increase of the strain amplitude results in stretching and yielding of the PSA's microstructure causing first a consolidation of the network and then a release with increasing strain amplitude. *RheoTack* approach was developed to allow for an advanced tack characterization of TTS with visual inspection during the measurement. The *RheoTack* results showed a clear resin content and rod geometry dependent behavior, and displays the PSA's viscoelasticity which results in either high tack values and long stretched fibrils or non-adhesion and brittle behavior. Moreover, diffusion of water or sweat during TTS's application could influence its performance. Therefore, a dielectric analysis based evaluation method displayed occurring water diffusion into the PSA from which the diffusion coefficient can be determined, and showed clear material and resin content dependent behavior. All methods allow for an advanced product-oriented material testing that can be utilized within further TTS development.

Resumé in Czech

Tradiční a nově vyvinuté testovací metody byly použity pro rozsáhlou charakterizaci transdermálních terapeutických systémů (TTS) a adheziv citlivých na tlak (PSA). Měření PSA v LAOS (Large Amplitude Oscillatory Shear) režimu korelovala s chováním materiálu při pohybu pacienta a ukázala, že všechna PSA se nacházejí v blízkosti bodu gelace. Zvyšování amplitudy deformace má navíc za následek roztahování a poddajnost mikrostruktury PSA, což způsobuje nejprve konsolidaci sítě a následně její uvolnění s rostoucí amplitudou deformace. V rámci disertační práce byla vyvinuta nová metoda *RheoTack*, která umožňuje pokročilou charakterizaci přilnavosti TTS s vizuální kontrolou během měření. Výsledky *RheoTack* ukázaly zřetelně vliv obsahu pryskyřice i geometrie nástroje. Vysoké adhezní hodnoty jsou spojeny s protaženými fibrilami těchto viskoelastických materiálů, nepřilnavost znamená naopak křehký lom. Difúze vody nebo potu během aplikace TTS může ovlivnit jejich výkonnost. Proto byla difúze vody do PSA hodnocena pomocí metody založené na dielektrické analýze. Získané difúzní koeficienty ukázaly jasné rozdíly v závislosti na materiálu a obsahu pryskyřice. Navržené a otestované metody umožňují pokročilé hodnocení materiálů orientované na aplikaci, které lze využít v rámci dalšího vývoje TTS.

Abstract

Transdermal therapeutic systems (TTS) are medical patches for the systematic treatment of e.g. severe pain, Parkinson or Alzheimer disease by releasing active pharmaceutical ingredients through the human skin. For successful medication, good adhesion of the TTS starting from the application on the patient's skin, during the application time 12 hours to 7 days taking patient's sweating, movement and friction into account, and traumaless removal from the skin are required. To fulfill these requirements, development of TTS is based on standardized testing methods taken from technical bonding for short- and long-term adhesion characterization. Unfortunately, these testing methods do not provide suitable information about the high requirements of TTS behavior on human skin.

This thesis addresses short and large amplitude oscillatory shear measurements of pressure sensitive adhesives (PSA) which can be correlated the patient's movement. Moreover, a dielectric analysis based method was developed, investigating diffusion kinetics of water diffusing into PSA. Further, new tack testing approach called *RheoTack* was developed, and implemented on a plate-plate rotational rheometer for tack testing of TTS.

The large amplitude oscillatory shear measurements can be related to deformation states which TTS experiences during daily life motion of a patient. These results showed that the investigated PSAs were located close to the gel point and that increasing strain amplitudes caused a consolidation of the gelled network, being stretched and released with a further increase of the strain amplitudes. Evaluation of the elastic and viscous Lissajous Bowditch diagrams revealed that a higher resin content caused higher shear thickening and shear thinning effects which resulted in a considerably more yielded and stretched microstructure of the PSA.

The influence of water and isotonic NaCl solution on the ion/dipole mobility was recorded with dielectric analysis, showing that this diffusion process was dependent on the PSA's chemical composition, the resin content with its resulting free volume in the PSA, and the diffusant itself. From these measurements, the diffusion coefficient can be determined being in accordance with literature values.

Newly developed *RheoTack* approach allows for an extensive characterization of the adhesion and release behavior of TTS together with a visual inspection of occurring detaching processes. Quantitative data evaluation showed that PSA type, resin content, retraction speed, and rod geometry influenced *RheoTack* parameters of TTS clearly. Extensive fibrillation and high tackiness were recorded for lower retraction speeds with lower resin contents, while brittle failure with non-tackiness was observed for higher retraction speeds and resin contents.

Furthermore, for the flat rods the highest stresses occurred at the circumferential stripe, while the center exhibited the highest stresses for the rounded rod. This stress differences caused contrasting release behavior, resulting in one force maxima for the flat rods, while the rounded rod reveals a plateau or a second force maxima. This displays that the rod geometry influences the tack behavior clearly.

The results from these developed testing methods give a better and more comprehensive insight into the PSA's and the TTS's material performance, leading to an approved application-related characterization than from standardized methods. As a result, this new knowledge contributes to further TTS development, and a higher livability for the patients.

Acknowledgements

First of all, I would like to thank sincerely my great Ph.D. supervisor Berenika Hausnerová for your enthusiastic interest towards my research topic, your unlimited support towards my concerns, worries and all questions which arise when you are doing a Ph.D. and a semester abroad. It was a real pleasure to work with such a professional person like you, being so relaxed and cool at the same time. I learned scientifically and personally lessons for life from you!

Next, I would like to thank my wise supervisor Bernhard Möginger! You supervised me during my Bachelor-, my Master- and my Ph.D. thesis. You believed in me and you gave me the possibility to do my scientific experiences and let me grow. You really thought me lessons for life, scientifically and personally! Thank you for being my mentor for more than 13 years!

Then, I have to thank you, Esther!!! I experienced your unlimited supported, scientifically and personally in all concerns, even though when you had trouble with your own health, unbelievable! Without you, I would have not finished the Ph.D. You are our “PuV-mother” 😊!

Thank you very much Roland Kádár for this indescribable semester abroad at the Chalmers, wow!!! It was an experience for life & I learned that much. Would love to work with you again.

Next, I have to thank you, Johannes Steinhaus! You believed in me since I met you as a student in the FKM lecture. Thanks to you I experienced these nice years at our university!!!

Special thanks to Christian Dresbach! You supported me although you were totally busy. THX!!

Of course I would like thank my great colleagues from the university Bonn-Rhein-Sieg. The material scientists: Klaus Schmitz, Astrid Beninde, Christina Mekelburger, Tatjana Radowitz, Hannah Rohde, Cassandra Moers, Alexander Jaekel, additionally my skiing colleagues and from our working group Lara Kehret, Mandy Gieler, Daniela Bornstein and Julian Rech, thank you for being our Diva 😊! You all were there for me and helped me with my research issues!!!

Great thanks goes to my students: Lucca Retterath, Tim Prescher, Bruno Gonzalves, Lisabeth Drewler, Simon Münchrath, Christian Grünewald, Gatien Kamsu Fogain, Lukas Werz, Sarah Klaes, and Maike Unkelbach. It was a pleasure to working with you!

Special thanks goes to all persons of the cooperating partners from the MOTTSAAL and the AdTTSWes project: LTS Lohmann Therapie-Systeme, DuPont, Thermo Fischer Scientific, Lohmann Tapes, NETZSCH Gerätebau, C+K electronics.

Special thanks goes to the TBU for the ERASMUS+ scholarship for the semester abroad and great thanks goes to Lada Vojáčková and all other TBU persons, who helped me. THX 😊!!!

Thank you very much Marc Williams for proof reading my thesis. 😊!!!

I would like to thank especially the team of the TREE-institute, and Graduate institute for your great personal and financial support including my Ph.D. scholarship. It helped that much!!!

Last but not least, I have to thank my best friends for life “De Joode Jonge and Mädche” and especially my family. First my brothers Markus and Thomas, her wife’s Sonja and Sabine and my nephews Marlon and Mias. Then, my great parents Gerlinde and Klemens, you all were always there and gave me unlimited support in all concerns. And finally, my wonderful girlfriend Ann-Cristin and your family, for the access to the Uni Bonn library ;-)) and much more! You are so smart, clever and cool, that working with you feels most of the time like vacation. We will have a nice renovated house with a great garden that fulfills all of our dreams.

Contents

1. State of the Art	1
1.1. Introduction	1
1.1.1. Historical development of TTS	2
1.1.2. PSAs for medical patches – TTS.....	3
1.1.3. Production of TTS	7
1.2. Adhesion of PSAs	8
1.3. Methods to determine adhesive properties	9
1.3.1. Probe tack test and loop tack test	9
1.3.2. Peel adhesion.....	11
1.3.3. Static shear test.....	12
1.4. Methods to determine rheological properties	13
1.4.1. General considerations	13
1.4.2. Shear rheometry	13
1.5. Methods to determine diffusion properties.....	17
1.5.1. Sorption experiments.....	18
1.5.2. Dielectric analysis	19
2. Aim of the work	23
3. Materials and Methods	24
4. Discussion of the results.....	26
4.1. Rheological properties – shearing of PSA and TTS.....	26
4.1.1. Amplitude sweeps of PSAs within short amplitude oscillatory shear [99]	26
4.1.2. Rheological characterization of PSA within large amplitude oscillatory shear [99].....	28
4.2. Diffusion properties [100]	30
4.2.1. Diffusion into PSA monitored with DEA [100].....	31
4.3. Adhesion properties.....	37
4.3.1. Standardized tests – probe tack and shear strength	37
4.3.2. <i>RheoTack</i> development [101].....	38
4.3.3. <i>RheoTack</i> data evaluation and results [101]	39
5. Conclusion.....	47
6. Contribution to Science & practice	48
References	50
List of Figures	57
List of Tables.....	60
Abbreviations and symbols	61
Publications, Posters and Presentations.....	63
Curriculum Vitae.....	64

Appendix A 65
Appendix B 66
Appendix C 71

1. State of the Art

1.1. Introduction

Transdermal therapeutic systems (TTS) are medical patches basing on pressure sensitive adhesives (PSA) which contain active pharmaceutical ingredients (API) and are applied to the patients' skin who suffer from e.g. severe pain, Parkinson or Alzheimer. Compared to the intake of pills, the use of TTS is advantageous for patients due to a better compliance, a continuous drug level in a blood system, and therefore friendly for the patient's stomach. Furthermore, the first-pass-effect, which presents the chemical or enzymatic modification and degradation within the gastrointestinal tract or liver, does not occur [1].

TTS are categorized in drug-in-adhesive matrix and drug reservoir type, **Fig. 1**. The first patch consists of a protective backing membrane, a drug-in-adhesive layer and a release liner. The drug-in-adhesive layer controls both the adhesion on and the drug release into the skin. The second patch contains an additional drug reservoir, a semi permeable membrane and a contact adhesive layer. While skin adhesion is secured by the contact adhesive layer, the API release from the reservoir is controlled by the semi-permeable membrane.

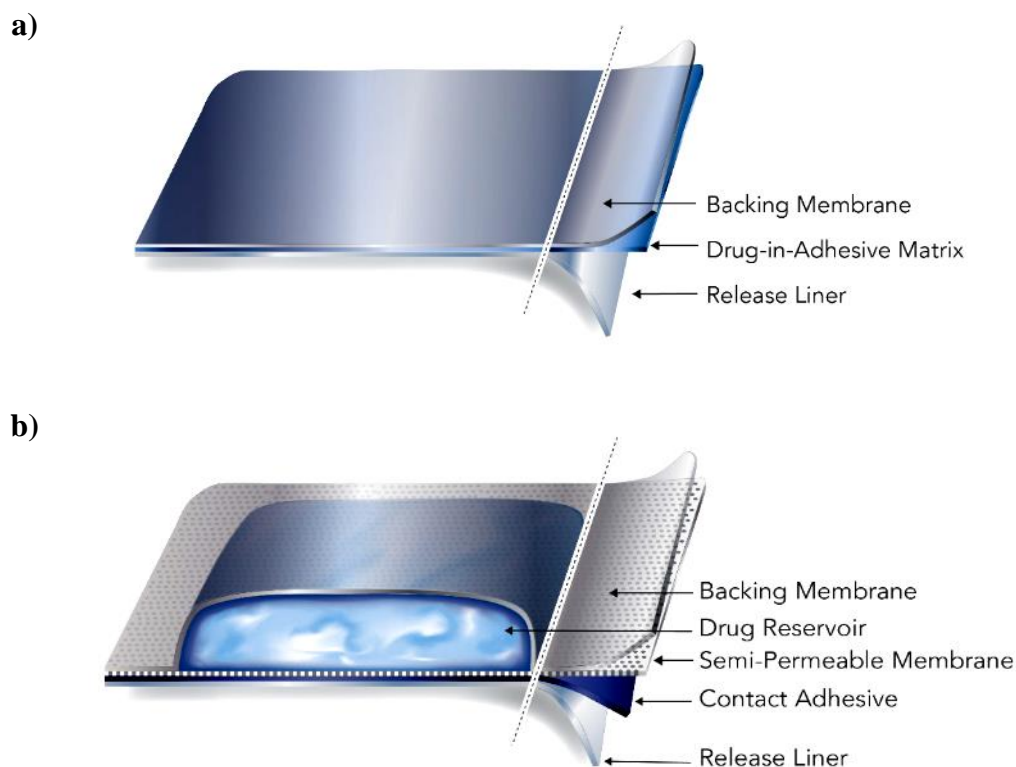


Fig. 1: Design of transdermal therapeutic systems (TTS) – a) drug-in-adhesive matrix type and b) drug reservoir type [2].

A continuous release of the API through the patient's skin leads to a uniform level of API in the blood system. Usually, the TTS have to be renewed between 12 hours and 7 days which leads to a better compliance for the patient instead of a constant intake of pills [3]. Currently, the application time represents a challenge for the PSA as e.g. detaching of the patch may cause an uncontrolled medicine release and "cold flow" due to the static low viscosity flow of the PSA from underneath the backing layer reduces the application duration. The successful

application of patches on the patient's skin requires adhesion of the entire TTS for the complete application time as well as a traumaless and easy removal afterwards [4].

1.1.1. Historical development of TTS

Transdermal administrations of herbal substances or essences were used since the origin of men. The Chinese (2000 BC) produced predecessors of TTS containing herbal substances [5]. From the early Egyptians (1550 BC) more than 800 prescriptions are reported for topical skin treatments of e.g. burned skin, wounds, blisters, headache or belly pain caused by the tapeworm [6]. The Greek physician Galen (AD 129-199), the "Father of pharmacy", developed dosage forms like the cold cream against dry skin whose composition is still in use [7]. Although in the late 19th century intact human skin was still suggested as totally impermeable [1], lethal cases of systemic poisoning after external contact with belladonna were reported [8, 9]. At the same time, the German pharmacopoeia reported skin tape based systemic developments for the treatment of stomach issues with peppermint oil, or the treatment of tuberculosis and tumors with belladonna. In the 20th century, after different lethal exposures to phenol [10] or hexachlorophene [11], first *in vivo* studies of the systemic uptake of mercury, methyl salicylate, testosterone and estrogen were performed [12-16]. In the 1950s due to the accidental discovery of side effects (headache, change of blood pressure and pulse) from people handling nitroglycerine, a nitroglycerine containing ointment was developed for the treatment of angina pectoris (circulatory disorder of the heart) [17].

Although all aforementioned forms administered active substances somehow on a transdermal way, Wurster's diffusion cell in the 1960s delivered defined doses of salicylate esters through the skin for the first time and can be regarded as the ancestor of TTS [18]. Ten years later, Zaffaroni [19] patented a rate controlling membrane for continuous drug flow through the skin. This was used within the first reservoir TTS (Transderm Scop[®], Alza Cooperation, 1979 on the US market) against motion induced nausea containing scopolamine [20]. In the following ten years, five different TTS with e.g. nitroglycerine, fentanyl, testosterone or nicotine were developed and commercialized [21-28]. Especially, the nicotine and fentanyl TTS were the most popular and successful ones leading to a broad acceptance in the 1990s [29].

Today TTS are widely accepted and represent a billion-dollar business. Recent research revealed that APIs up to 500 Da can pass the lipid bilayer of the skin [1]. Hence, more than 50 different patches with 18 different APIs from several producers are available on the market [1]. TTS are mainly used for pain management, and hormone and addictive therapies represent the leading areas [30]. Thus, the drug release from the TTS, the permeation through the skin and the adhesion of the entire patch for the complete application time are key issues of TTS [1]. Recently developed methods e.g. iontophoresis, sonophoresis, photochemical waves, electroporation, thermal ablation or microneedles (MN) open new possibilities to increase the size of the passing of APIs through human skin [31]. Especially the research and development interest within the field of MN is high as they pierce the superficial layer without pain and guide the API directly to blood capillaries for an active absorption [31]. Furthermore, the size of the patches can be reduced because the amount of diffused API per skin area is higher compared to the drug in adhesive or reservoir TTS. Today seven MN products made of various materials for skin treatment, vaccination or drug delivery against Alzheimer or cancer are available on the market [32].

1.1.2. PSAs for medical patches – TTS

Most widely used soft polymers for PSAs are acrylates, polyisobutylene, silicones and their mixtures. Other co-adhesives can be carboxymethyl cellulose, ethylene vinyl acetate and polyvinylpyrrolidone [33]. The use of a PSA on a skin is performed by applying slight pressure to attach to skin and is to be removed without a residue. Thus, the requirements of an appropriate adhesion consist of good flowability and wetting of the PSA towards the substrate surface. Additionally, the residue-free removal demands sufficiently stiff behavior and cohesion of the PSA. Hence, during the application time between 12 hours and 7 days, the entire TTS has to follow the skin motions without detaching to guarantee a successful medication [33, 34]. Furthermore, good gas and vapor permeation properties (water from outside is avoided by the backing layer, while sweat should be released through the TTS) are favorable as a possible maceration of the skin increases the risk of infections caused by bacteria or fungi. Considering the complex requirements of PSAs for TTS, the pros and cons of the most important criteria are presented in **Table 1**.

Table 1: Pros and cons of PSAs that are used for TTS [35-37].

	Acrylates	Polyisobutylenes	Silicones
Pro's	good adhesion properties	high tack weak adhesive properties	adhesion towards surfaces having a low surface energy
	good resistance towards aging	good thermal stability good oxidative stability good chemical resistance	good chemical resistance low chemical reactivity and toxicity good temperature stability
	high vapor transmission		high gas and vapor permeability
		low toxicity no skin irritation	low skin irritation and sensitizing
	relatively cheap		
Con's	low adhesion to surfaces with low surface energies	bad adhesion to many surfaces due to low polarity	lower adhesion strength than comparable organic PSAs
	skin irritation and sensitizing	costly production process of final products	costly flourosiliconated release liner necessary
		low air, moisture and gas permeability	

Acrylic PSAs

Acrylic PSAs consist of copolymers from different acrylic homopolymers to fulfill the required adhesion properties. The general molecular structure of a methacrylic ester (monomer) is shown in **Fig. 2**, where $R = \text{CH}_3$ and $R' = \text{alkyl group}$ [35, 38].

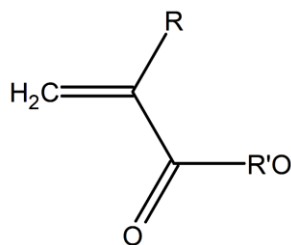


Fig. 2: General molecular structure of a methacrylic ester (monomer) with $R = \text{CH}_3$ and $R' = \text{alkyl group}$ (according to [35]).

Although various acrylic monomers are available on the market, three monomers are mainly used for PSAs: 2-ethylhexyl acrylate, butyl acrylate and iso-octyl acrylate [38]. They are produced by a free radical polymerization in an emulsion or solution reaction and started by thermal or redox initiators. The PSAs properties, e.g. adhesion and release behavior, can be influenced by using special monomers during polymerization or adding additives to the PSA. Monomers having low glass transition temperatures (T_g) increase tackiness and adhesion, while multifunctional monomers lead to a higher cohesion of the PSA. Monomers with acidic, basic or other functional groups are used for better adhesion and solubility for certain APIs through polar groups. After polymerization, PSAs can be modified by resins, tackifiers, plasticizers, and/or radiation for cross-linking to optimize and adapt the copolymers adhesion and release properties [35, 38].

Acrylic PSAs are low priced compared to other PSAs, feature high vapor transmission properties and exhibit good performance variability through the use of various monomers or post-polymerization. This results in a good adhesion and release behavior. However, residual initiators or monomers can lead to skin irritation or sensitization effects [35-38].

Polyisobutylenes PSAs

Polyisobutylenes (PIB) PSAs consist of an isobutylene (IB) homopolymer or an IB and isoprene (IP) copolymer. Both are produced by a cationic polymerization, **Fig. 3**.

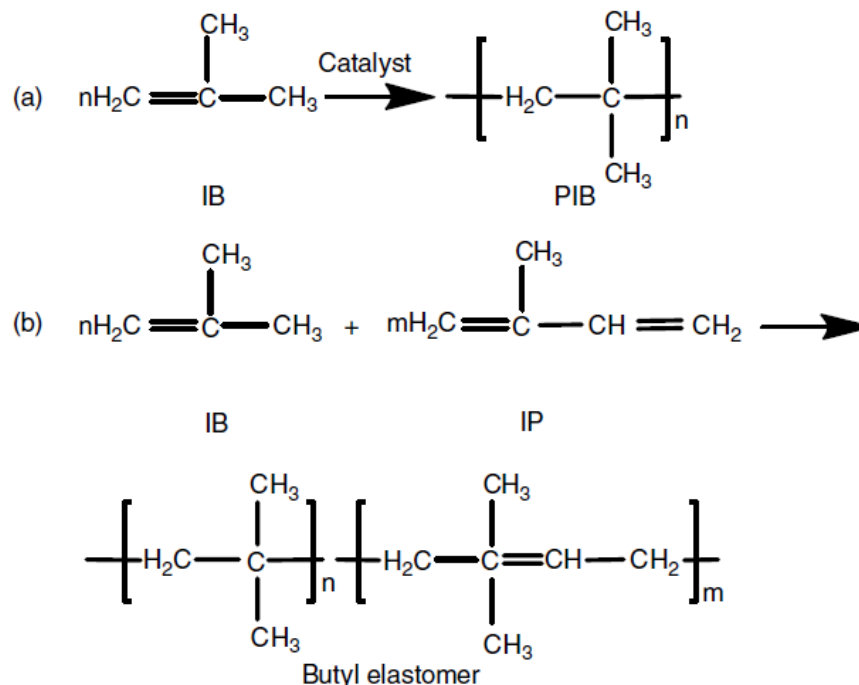


Fig. 3: Polymerization of polyisobutylene (PIB) as a) homopolymer from isobutylene (IB), b) copolymer from IB and isoprene (IP) [35].

PIB PSAs are synthetic rubbers having a linear and nonpolar molecular structure. While the nonpolarity causes permanent and high tack, the resulting adhesion to many surfaces is poor. To achieve better adhesion, the polarity of PIB is increased by tackifiers, waxes, oils or fillers or PIB mixtures having different molecular weights. The PIB PSAs exhibit low air, moisture and gas permeability as well as good thermal and highly oxidative stabilities. Furthermore, PIB is not skin irritant, reveals good resistance towards chemicals and features high oxidative stabilities. On the market no “ready to use PIB PSAs mixtures” are available, therefore every patch manufacturer has to compound their own PIB recipe for the intended application [35, 38].

Silicone PSAs

Silicone PSAs consist of linear high molecular weight silicone polymers with a composition of up to four oxygen bonds and highly branched silanol functional siloxane resins, having a complex three dimensional structure [34, 35], **Table 2**. The polymer and resin are chemically cross-linked during a base-catalyzed polycondensation reaction through the silanol functionalities on the resin and the terminal silanols of the polymer.

Table 2: Building blocks for silicones [35].

Formula Type	Stereo Model	Symbol	No. Linkage to Oxygen	Wt % [SiO] (Inorganic) (%)
$(\text{CH}_3)_3\text{SiO}_{1/2}$		M	Mono	44.5
$(\text{CH}_3)_2\text{SiO}$		D	Di	59.5
$(\text{CH}_3)\text{SiO}_{3/2}$		T	Tri	77.6
$\text{SiO}_{4/2}$		Q	Quadri	100.0

The use of non-amine compatible (NAC) PSA is limited only for APIs, which do not contain amine functionalities due to a possible reaction between terminal OH- and amine-groups. The NAC PSA, the result of a “boding process”, is a broad network consisting of polymer chains connected to resin molecules with OH- groups at the end of the polymer chains, **Fig. 4**. A further chemical treatment of the NAC leads to the amine compatible (AC) PSA having relatively inert trimethylsilyl end groups, which prevent possible reactions between PSA and API [34,35].

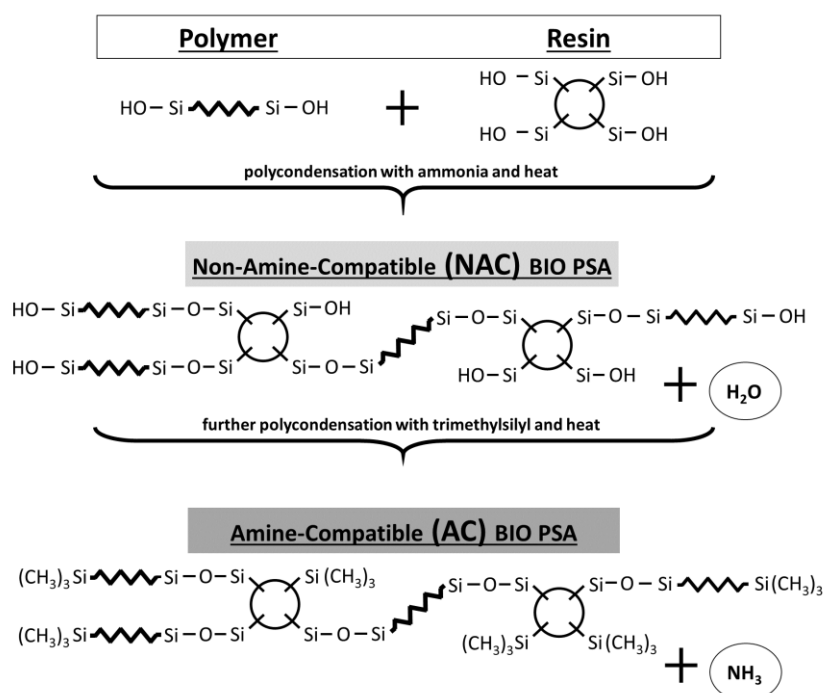


Fig. 4: Chemical structures of the non-amine compatible (NAC) and amine-compatible (AC) PSA and the steps of their synthesis (according to [39]).

Silicone PSAs are well suited for applications as TTS due to their appropriate properties for medical usage. Firstly, their low toxicity towards skin represents a key-feature that results in various skin applications. Secondly, the low chemical reactivity with respect to API and skin ensures a chemically stable system for the time of application. Thirdly, the excellent chemical resistance towards acids or bases and the environmental stability with respect to moisture make them suitable for skin applications. In addition to that the low surface-energy adhesion enables adhesion of the silicone PSAs also to surfaces having low surface energies. Although silicone PSAs have fairly good adhesion properties to many substrates, the final adhesion strength of organic PSAs are higher. Besides higher material prices for silicone PSAs, special and expensive flourosiliconisated release liners are necessary to enable easy removal of the backing layer from the silicone PSAs. Based on these arguments, especially the low toxicity for skin applications, silicone PSAs were chosen for this work.

1.1.3. Production of TTS

The production of TTS is a multistage process that starts with the mixing of the dissolved PSA in a system related organic solvent with the API. The concentration of the API is close to the maximum solubility limit. This high API level is needed to ensure sufficient medication release during application time. This limit shall not be exceeded to prevent possible API crystallization during storage [40]. During the mixing process further substances can be added e.g. penetration enhancers to increase skin permeability [41-46], plasticizers to improve flexibility and patch removability [47, 48], solubilizers to achieve high API concentrations in the PSA by the creation of micelles, and finally fillers [49] which increase the cohesiveness of the patch.

After the mixing process, the drug containing adhesive mixture is introduced to the coating process consisting of the following steps, **Fig. 5**:

- drug containing adhesive mixture is coated on the release liner by a doctor roll at the coating head
- the adhesive film is dried in the drying channel
- the backing layer is attached onto the adhesive system
- the adhesive system is rolled to master rolls for further processing.

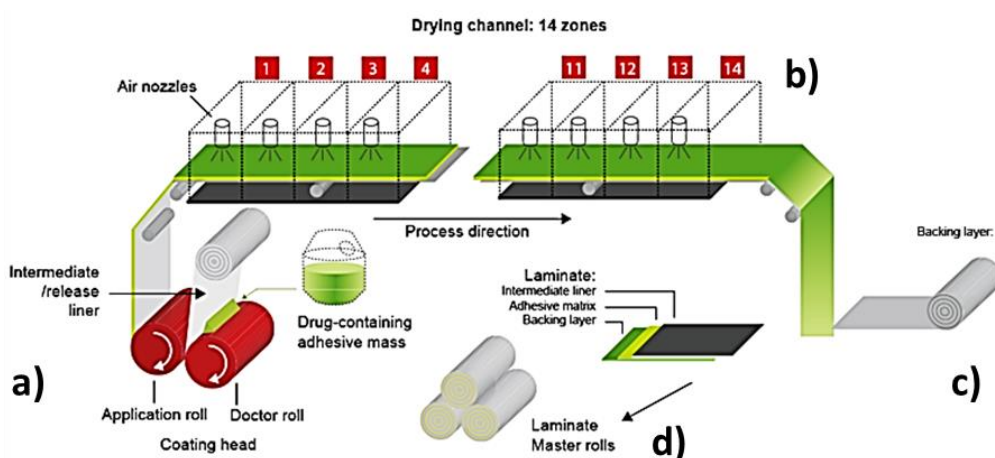


Fig. 5: Scheme of TTS manufacturing with a coating head, drying zone and laminating zone (according to [50]).

The final step of the TTS production is the cutting and packaging to single pouches according to customers' requirements. The production of these medical patches demands high standards

according to e.g. Transdermal and Topical Delivery Systems – Product Development and Quality Considerations FDA [2], EMA [3], ICH Q8(R2) [51] and ICH Q2(R1) [52], and requires clean rooms to avoid contaminations.

1.2. Adhesion of PSAs

Adhesives join two or more materials to each other. Their most important characteristics are adhesion and cohesion. The cohesion describes the inner strength of the adhesive. The adhesion is the ability to stick to other materials and is governed by interacting forces modeled with dispersive, diffusive, mechanical, electrostatic and chemical contributions, **Fig. 6**.

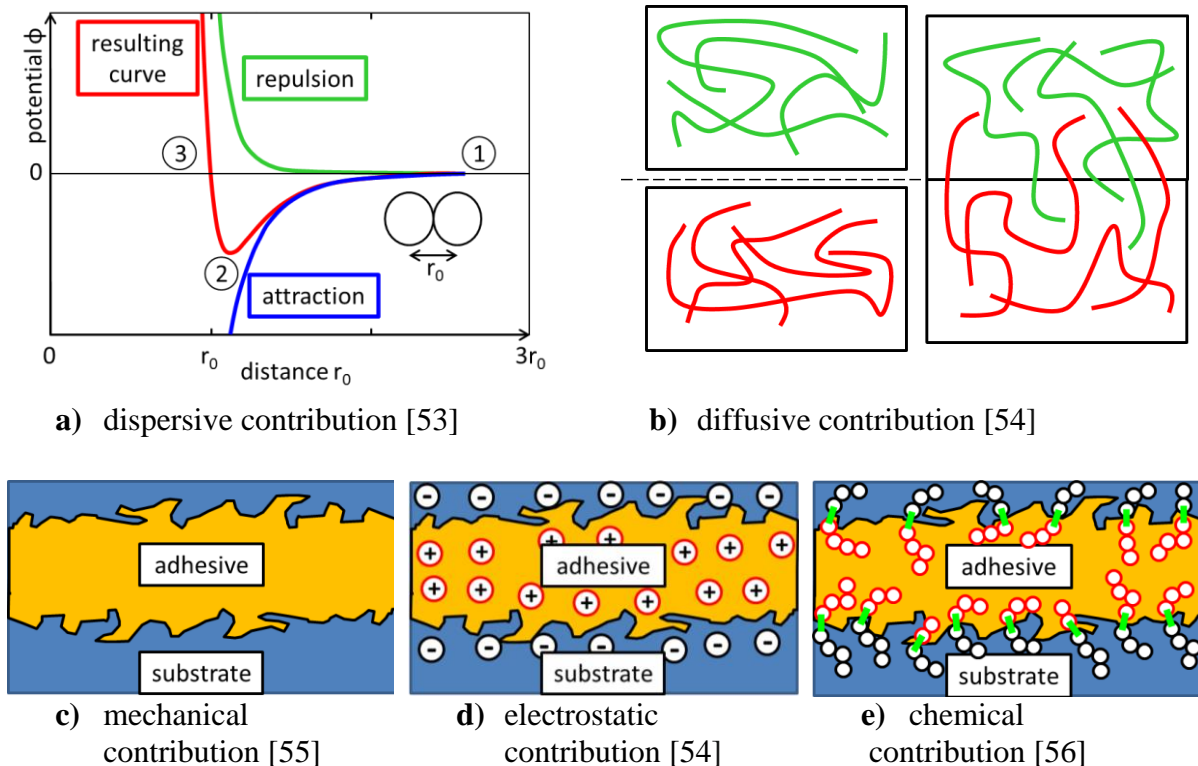


Fig. 6: Schematic representation of models describing adhesive effects: a) adsorption contribution; b) mechanical anchoring; c) diffusive contribution; d) electrostatic contribution; e) chemical bonding.

The dispersive contribution is a universal process describing physical adsorption between atoms and must be taken into account for all adhesion cases of substrates independently of their surface properties and topographies. Based on the adjacency between a liquid adhesive and a solid substrate on atomic level, attractive or repulsive forces act distance dependently between atoms, **Fig. 6 a)**. Large distances may allow for only attraction due to Van de Waals or other intermolecular forces (blue curve). At small distances the interaction of electron shells causes increasing repulsive forces (green curve). The resulting distance dependent force is e.g. described by the Lennard-Jones potential (red curve) [56, 57]

The diffusion contribution is based on Brownian motion of molecules and chains between two polymers leading to an interdiffusion of polymer chains and is observed e.g. for polyvinylchloride and rubber materials, **Fig. 6 b)** [58].

Mechanical contribution focus on the flowability of the adhesive material into the porous or rough surfaces structures of substrates or the wetting behavior. The evaporation of solvents out

of adhesives lets harden it and interlocks adhesive and substrate mechanically, **Fig. 6 c**). The wetting is determined by the surface energy of the substrate and can be described by the surface energy G_0 :

$$G_0 = G - \psi \quad (1)$$

with G as the fracture energy and ψ representing the adsorption energy (both given as energy per area). This leads to the conclusion that the “true” area and its surface energy G_0 are greater for rough surfaces than for smooth ones, demonstrated e.g. by [59].

Electrostatic contribution regards the adhesive bonding analogous to electrical capacitors, **Fig. 6 d**). In any material layer there are free electric charges (ions, permanent dipoles) evoking the generation of electric double layers due to the electrochemical potential difference between the substrate and adhesive. In contrast to interface bonding, where charge transfers occur at the interface, electrostatic adhesion is based on attractive forces due to electric double layers.

The chemical contribution is founded on forming covalent or ionic bonds between substrate and adhesive, **Fig. 6 e**), e.g. the fixation of the front windshield of a car or the repair of a bicycle’s tube with a repair kit.

1.3.Methods to determine adhesive properties

Most measuring techniques which characterize adhesion behavior and determine adhesive properties were developed in adhesive bonding and led to many standardized adhesion testing methods such as probe tack, loop tack, peel adhesion and shear resistance. They are also used for quality assurance purposes of medical patches and are performed mainly on stainless steel or aluminum substrates, not on skin-like substrates.

1.3.1. Probe tack test and loop tack test

The short-term adhesion behavior of patches is determined by either probe tack test according to ASTM D2979 [60], **Fig. 7 a**), or loop tack test according to DIN EN 1719 [61], **Fig. 7 b**). In a probe tack test a stainless steel probe rod with a diameter of 5 mm is compressed to the adhesive with 9.79 ± 0.10 kPa for a dwell time of 1 s. Then the probe is pulled off with a speed of 10 ± 0.01 mm/s. For loop tack testing, a looped adhesive stripe is lowered on a stiff substrate until the contact area reaches 25 x 25 mm. After a dwell time of 1 s, the loop is pulled off with a retraction speed of 5 mm/s. From both tests the maximum force represents a measure for the tackiness of adhesives during detaching.

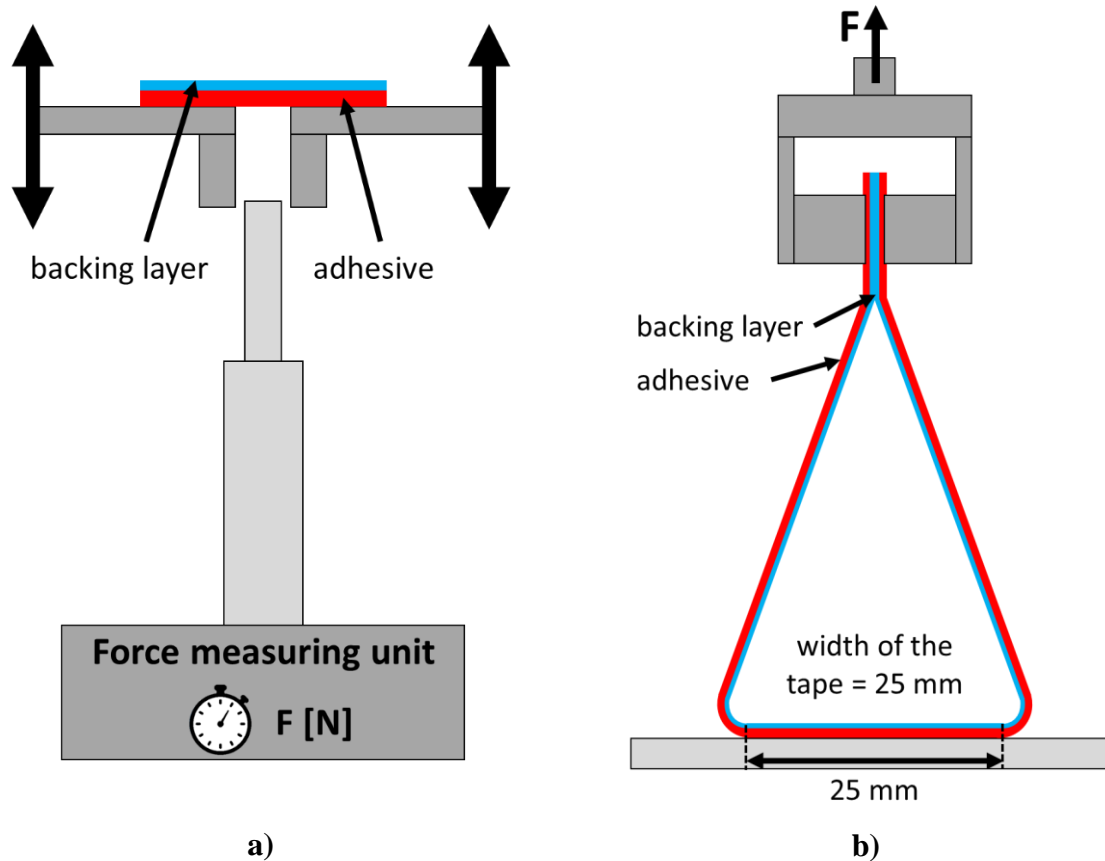


Fig. 7: Scheme of a) probe tack test according to ASTM D2979 [60] and b) loop tack test according to DIN EN 1719 [61].

Instrumented tack tests provide more information of the adhesion behavior as they allow for generating retraction rate dependent force time or retraction force displacement curves [62], **Fig. 8**. The compression force increases during loading. After the dwell time the retraction starts, the force decreases and changes to the tensile force during detaching measured as the negative force. The force decreases further until the tack strength (the maximum force) is reached. Subsequently, the force increases again until the complete detaching of the probe and the sample is reached at the zero force. Instrumented tack tests provide further adhesion parameters e.g. maximum tack force (= minimum force in curve) and tack energy (= area under the tensile curve). The tack energy is a measure of the detaching work after short application time.

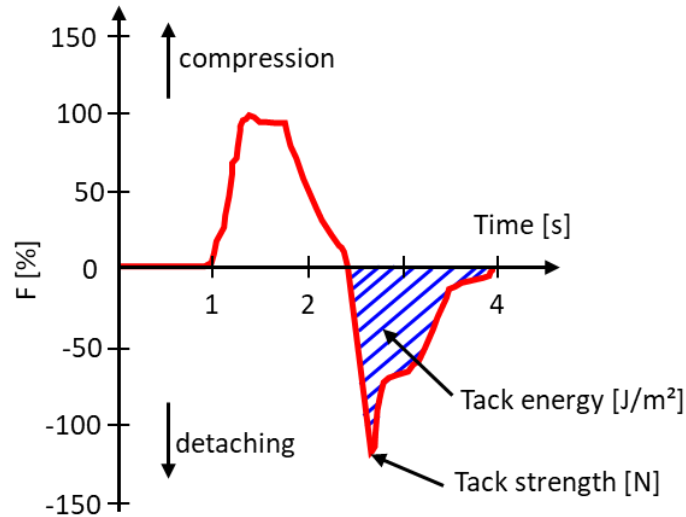


Fig. 8: Force-time curve of an instrumented tack test with a compressive force during loading and a tensile force during detaching [62].

1.3.2. Peel adhesion

Peel adhesion properties of patches are determined on stainless steel plates according to DIN EN ISO 29862 [63] with angles either 90° or 180°, **Fig. 9**. An adhesive strip with dimensions 24 x 300 mm is pressed with a 2 kg roll to a stainless steel plate without enclosing air.

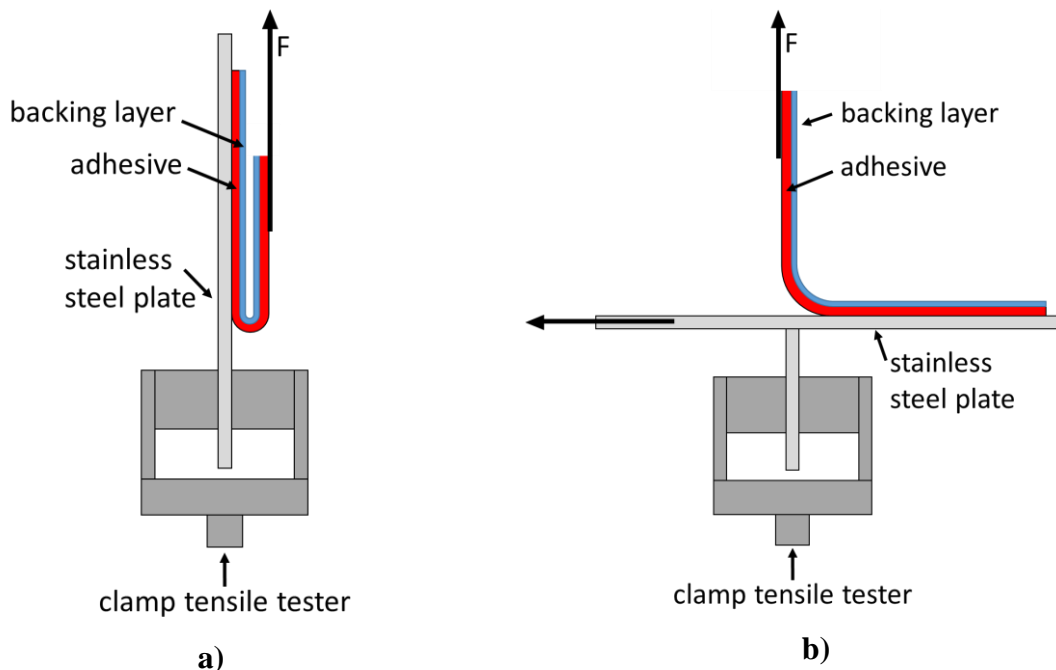


Fig. 9: Scheme of the peel adhesion tests with peel angle 180° a) on a stainless steel plate and with peel angle 90° b) with a horizontally moveable stainless steel plate.

After a dwell time of 1 minute, the peel adhesion measurement is performed using a tensile tester with a retraction speed of 300 mm/s. From the measured curve, the force values of the first 25 mm are discarded. Then, the mean force of the following 50 mm is evaluated as peel adhesion force, **Fig. 10**. The load increases sharply at the beginning of the peel extension, and

reaches the scattered steady state load level indicating that the detaching happens stepwise. The peel adhesion force quantifies the mean force necessary to remove an adhesive tape from a metal substrate under given angle and velocity.

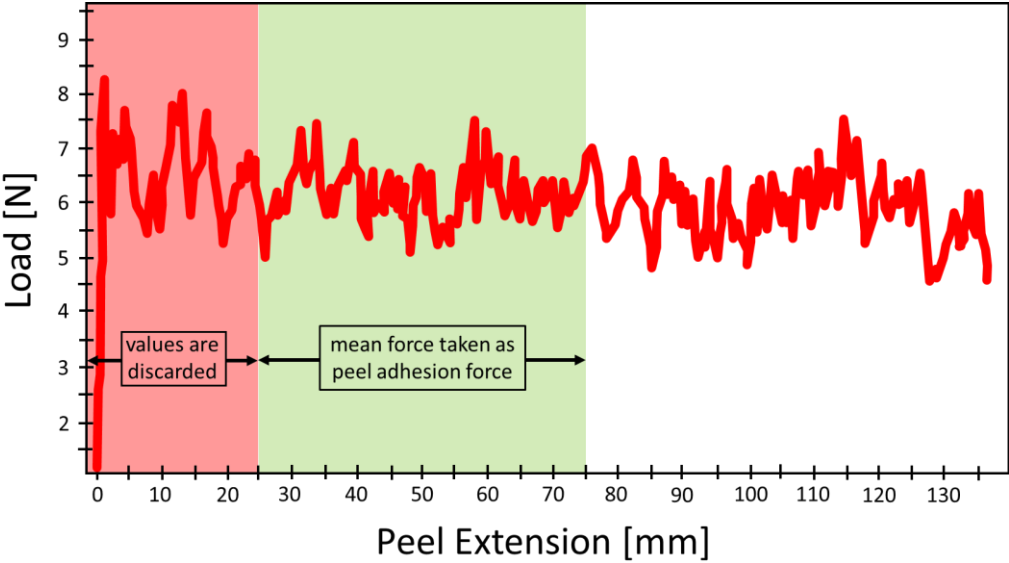


Fig. 10: Evaluation of an instrumented peel adhesion test (according to [64]).

1.3.3. Static shear test

Static shear test characterizes the uniformity of adhesion properties of patches by measuring the time to failure according to DIN EN ISO 29863 [65]. A patch having a cross-section 144 mm² is adhered to a stainless steel plate, tilted by 2°, and loaded with a weight of 1000 g, Fig. 11. Time of failure is reached if the patch with the weight is separated from the substrate. Short failure times indicate low cohesion properties and good flowability of adhesives. Due to the composition of a patch, cohesive or adhesive failure may occur. Residual PSA on the stainless steel plate after the measurement indicates that the adhesion exceeds the cohesion.

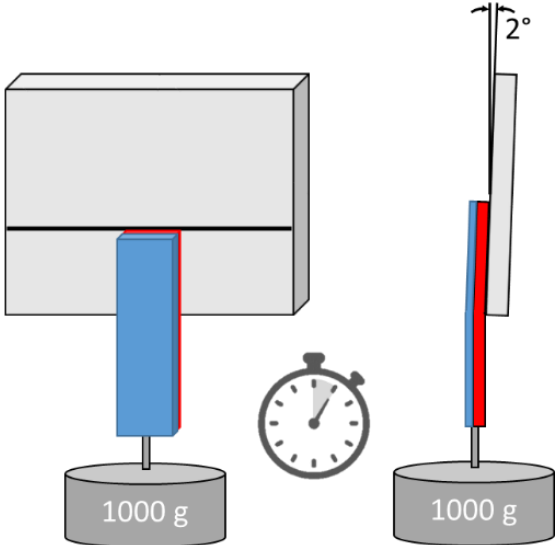


Fig. 11: Scheme of a static shear testing device with a 2° twisted stainless steel plate and a 1000 g weight.

1.4. Methods to determine rheological properties

1.4.1. General considerations

Newton's law links stresses to deformation rates introducing the viscosity as a measure of internal resistance of a fluid against flow:

$$\text{Shear flow} \quad \tau(\dot{\gamma}) = \eta_{\text{shear}} * \dot{\gamma} \quad (2)$$

with shear stress $\tau(\dot{\gamma})$, shear viscosity η_{shear} and shear rate $\dot{\gamma}$.

During the manufacturing the dissolved PSA experiences (mixing process and the following coating of the dissolved PSA onto the release liner) shear flow and extensional flow. Whereas, during the TTS's application the solid-like PSA is subjected to shear flow stresses. When removed from a skin, both extensional and shear stress occur in different ratios depending on the peel-off angle and retraction velocity.

1.4.2. Shear rheometry

A capillary rheometer determines a pressure loss of polymer melts if flowing through a temperature-controlled capillary at shear rates being in the range $\sim 10^{-1}$ to 10^6 s^{-1} . This allows for the calculation of the viscosity using the Hagen-Poiseuille equation:

$$\dot{Q} = \frac{\Delta V}{\Delta t} = \frac{\pi R^4 \Delta p}{8 \eta l} \Rightarrow \eta = \frac{\Delta V}{\Delta t} = \frac{\pi R^4 \Delta p}{8 l \dot{Q}} \quad (3)$$

with volume flow \dot{Q} , radius of capillary R , pressure difference Δp , viscosity η , and capillary length l . Eq. 3 is valid for Newtonian fluids. To obtain the real viscosity of nonlinear viscoelastic melts, the real shear stresses and real shear rates have to be calculated using Bagley and Rabinowitsch corrections, respectively.

For low shear rates and/ or oscillatory measurements, rotational rheometers with a plate-plate, cone-plate or cylinder (Couette/Searle) geometries are used, **Fig. 12**.

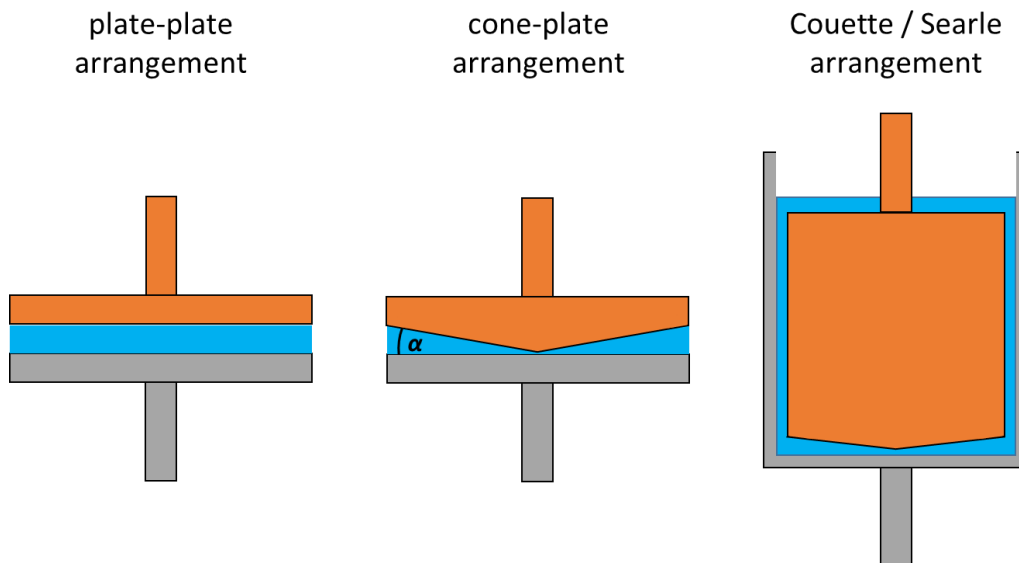


Fig. 12: Geometries of rotational rheometers: plate-plate, cone-plate (with the cone angle α) and Couette/Searle arrangement; the gap, where the sample is strained, indicated in blue.

Some commercially available rheometers feature normal force sensors to monitor normal stress differences which may occur under certain flow conditions. The normal force sensor offers the possibility to perform instrumented tack measurements with a rotational rheometer [66-69].

The short amplitude oscillatory shear (SAOS) rheology measurement, **Fig. 13a**), according to DIN EN ISO 53019-4 [70] allows for standardized determination of viscoelastic properties as a function of temperature and frequency of fluids, gels and soft solids. A plate-plate geometry is used either in a controlled stress mode (CS) or a controlled deformation mode (CD). Viscoelastic materials exhibit a phase shift between sinusoidal excitation and sinusoidal response, **Fig. 13 b**).

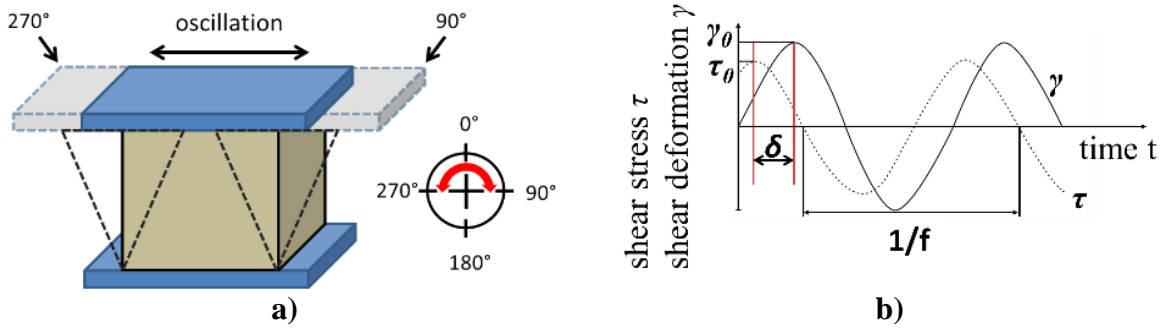


Fig. 13: Scheme of the oscillatory shear measurement a) sample is loaded in an oscillatory manner between two plates, b) sinusoidal excitation (γ), response signal (τ) and phase angle(δ).

The deformation $\gamma(\omega, t)$ is given by

$$\gamma(\omega, t) = \gamma_0(\omega) \sin(\omega, t) = \gamma_0 * e^{i(\omega t)} \quad (4)$$

with frequency ω and deformation amplitude $\gamma_0(\omega)$. The stress response is

$$\tau(\omega, t) = \tau_0(\omega) \sin(\omega t + \delta(\omega)) = \tau_0 * e^{i(\omega t + \delta(\omega))} \quad (5)$$

This yields the complex shear modulus G^* :

$$G^*(\omega, \delta) = \frac{\tau_0(\omega) * e^{i(\omega t)} * e^{i(\delta)}}{\gamma_0(\omega) * e^{i(\omega t)}} = \underbrace{G_0(\omega) \cos(\delta(\omega))}_{\text{storage modulus } G'} + i \underbrace{G_0(\omega) \sin(\delta(\omega))}_{\text{loss modulus } G''} \quad (6)$$

The real part of G^* represents the storage modulus G' , which is a measure of the elastically stored energy, and the imaginary part of G^* represents the loss modulus G'' , which is a measure of the dissipated energy. A further important quantity is the loss factor characterizing the damping behavior:

$$\tan \delta(\omega) = \frac{G''}{G'} \quad (7)$$

With increasing shear amplitude, the originally sinusoidal stress becomes distorted indicating the end of the linear viscoelastic region (LVE), where G' and G'' are independent of the applied strain amplitude γ_0 . This end is determined by an amplitude sweep at constant frequency and temperature, **Fig. 14**. At higher amplitudes G' and G'' decrease. The transition strain amplitude between LVE and non-LVE can be evaluated using models of e.g. Carreau-Yasuda, Ellis or Cross-Williams [71].

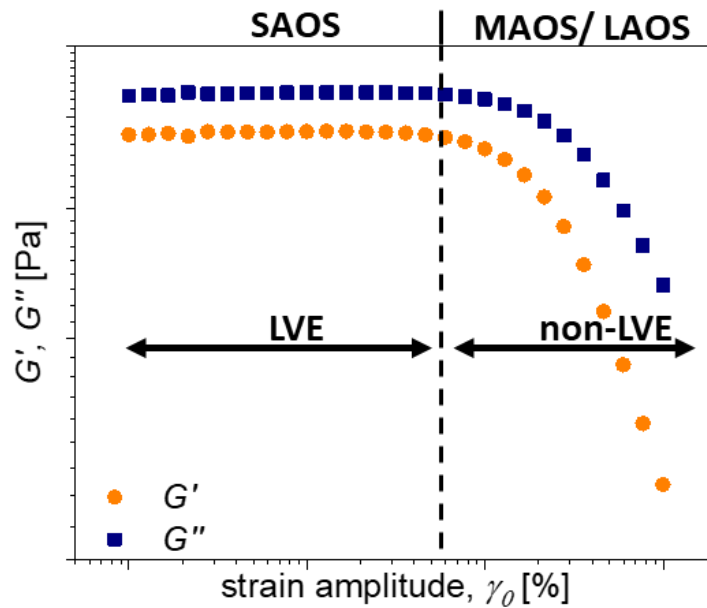


Fig. 14: G' and G'' being independent from strain amplitude γ_0 in the LVE or SAOS region and dependent from the strain amplitude γ_0 in the middle and large amplitude oscillatory shear region (MAOS, LAOS).

Fig. 15 shows the frequency dependent G' and G'' of a PSA showing a cross over point (COP) or gel point. Below COP, the PSA behaves rather viscous and above rather solid.

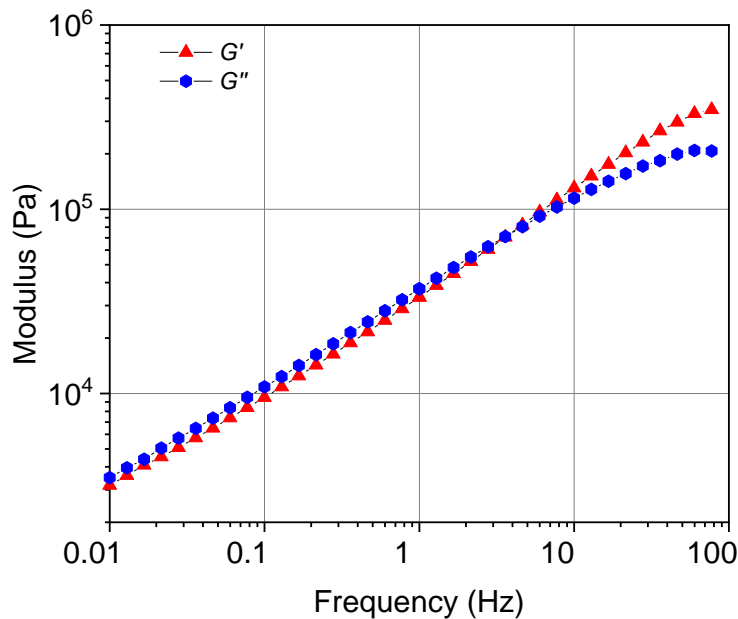


Fig. 15: Frequency dependent storage G' and loss modulus G'' of a PSA at $T = 30^\circ\text{C}$.

Using frequency sweeps, the viscoelastic properties of soft solids can be determined over a frequency range of 4 to 6 orders of magnitude, **Fig. 16**. In the case of PSA, G' and G'' at low frequencies can be correlated to peel adhesion and tack during bonding and at high frequencies to peel adhesion and tack during debonding or detaching [72].

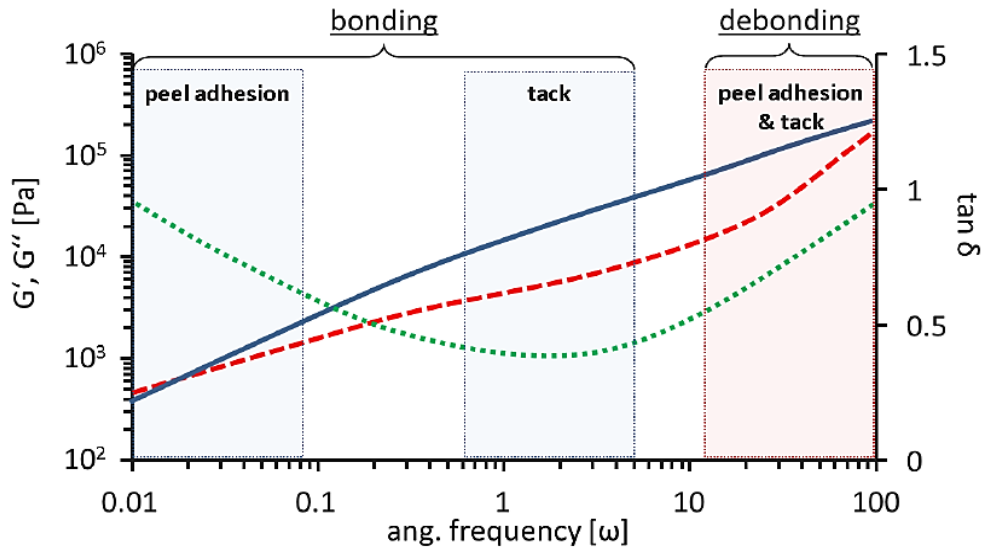


Fig. 16: Frequency dependent G' and G'' of a PSA and its correlation to bonding and debonding [72].

Large amplitude oscillatory shear (LAOS) measurement allows for the determination of rheological behavior beyond the LVE range, where moduli are dependent on strain amplitudes. LAOS is a relevant method for materials which are subjected to large and fast deformations during application. The non-sinusoidal character of the response signal requires data evaluation by Fourier analysis providing relevant intensities in terms of higher harmonics. In the SAOS range only the 1st harmonic I_1 is not zero, while in MAOS the 3rd harmonic I_3 becomes relevant and in the LAOS range there may occur 5th and 7th harmonics. Therefore, the ratio $I_{3/1}$ is used as a measure of a nonlinear behavior.

Fig. 17 exhibits the strain amplitude dependent behavior of G' and G'' and the corresponding ranges of SAOS, MAOS and LAOS. Fourier transformation-data evaluation shows a decrease of $I_{3/1}$ with increasing strain amplitude accompanied by significant scatter due to instrument noise. In the MAOS range, $I_{3/1}$ increases quadratically with strain amplitude: $I_{3/1} \propto \gamma_0^2$ [73, 74]. Other researchers report a non-quadratic dependency in the MAOS and LAOS region [75-78].

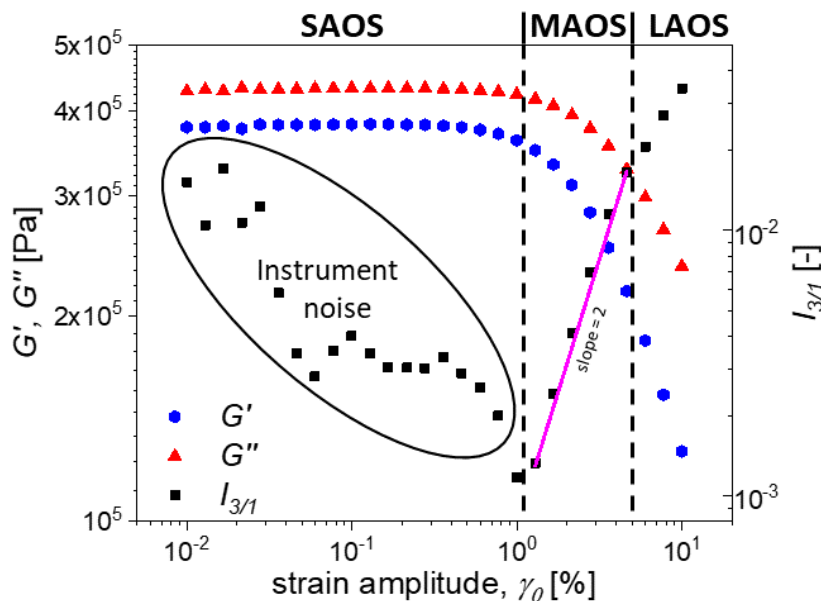


Fig. 17: Strain amplitude dependent moduli G' and G'' as well as $I_{3/1}$ – nonlinear behavior starts above strain amplitudes of 1%.

Strain amplitude dependent moduli G' and G'' can also be evaluated in the LAOS range using Lissajous-Bowditch diagrams, **Fig. 18**. Therefore, inter-cycle (between different γ_0) and intra-cycle (within a cycle) nonlinear behavior is characterized by the quantities

$$\text{Zero-strain modulus} \quad G'_M(\gamma) = \left. \frac{d\sigma}{d\gamma} \right|_{\gamma=0} \quad (8)$$

$$\text{Maximum-strain modulus} \quad G'_L(\gamma) = \left. \frac{\sigma}{\gamma} \right|_{\gamma=\pm\gamma_0} \quad (9)$$

$$\text{Zero-rate dynamic viscosity} \quad \eta'_M(\dot{\gamma}) = \left. \frac{d\sigma}{d\dot{\gamma}} \right|_{\dot{\gamma}=0} \quad (10)$$

$$\text{Maximum-rate dynamic viscosity} \quad \eta'_L(\dot{\gamma}) = \left. \frac{\sigma}{\dot{\gamma}} \right|_{\dot{\gamma}=\pm\dot{\gamma}_0} \quad (11)$$

γ_0 strain amplitude, $\dot{\gamma}(t)$ the time dependent shear rate and $\dot{\gamma}_0$ the shear rate amplitude. These quantities can be used to define further LAOS quantities:

$$\text{Strain stiffening ratio} \quad S(\gamma_0) \equiv \frac{G'_L(\gamma_0) - G'_M(0)}{G'_L(\gamma_0)} \quad (12)$$

$$\text{Shear thickening ratio} \quad T(\dot{\gamma}_0) \equiv \frac{\eta'_L(\dot{\gamma}_0) - \eta'_M(0)}{\eta'_L(\dot{\gamma}_0)} \quad (13)$$

$S > 0$ indicates intra-cycle strain stiffening behavior and $S < 0$ intra-cycle strain softening behavior. The $T > 0$ indicates intra-cycle shear thickening behavior and $T < 0$ intra-cycle shear thinning behavior. If $S = 0$ and $T = 0$, the material behaves linear viscoelastic.

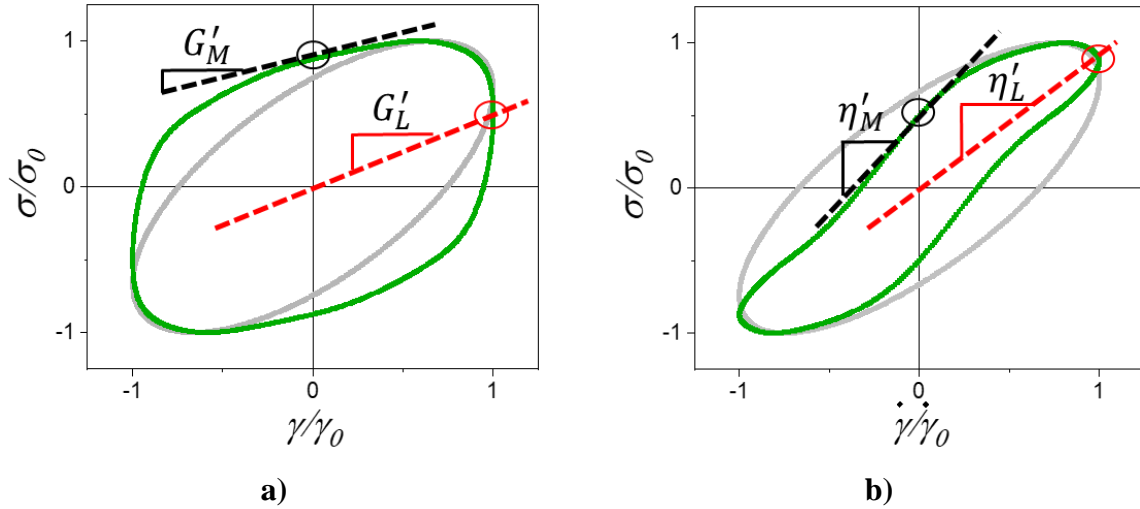


Fig. 18: Normalized elastic a) and viscous b) Lissajous-Bowditch diagrams for linear viscoelastic behavior (light grey) and nonlinear behavior (green) with determination of zero-strain modulus G'_M , maximum strain modulus G'_L , zero-rate dynamic viscosity η'_M , and maximum-rate dynamic viscosity η'_L .

1.5. Methods to determine diffusion properties

Diffusion describes processes in which matter is transported from one part of a system to another by random molecular motions. The first mathematical description of diffusion was postulated by Fick in 1855 [79]. Fick's 1st law describes the diffusion of a substance in isotropic materials under a concentration gradient at steady state conditions [71, 80, 81]:

$$J = -D \frac{\partial c}{\partial x} \quad (14)$$

with J as flow density of diffusing substance through unit area, D representing diffusion coefficient, C standing for concentration of diffusing substance, x as a space coordinate.

Fick's 2nd law describes the time and space dependent (unsteady state) diffusion in a 1D representation [71, 79]:

$$\frac{\partial C}{\partial t} = \frac{\partial}{\partial x} \left[D \frac{\partial C}{\partial x} \right] \quad (15)$$

with t as time, where diffusion is measured. The permeation process through polymers consists of three steps:

- sorption of the diffusing substance at the contact surface,
- diffusion through the polymer due to the concentration gradient,
- desorption and evaporation of the diffusing substance at the other surface.

Factors such as solubility, macromolecular density, side group complexity, polymer polarity, crystallinity and preferential orientation of macromolecules, filler shape and content, filler distribution and orientation, plasticization and humidity affect the permeation and diffusion behavior of substances through polymers [71]. Common methods to investigate diffusion and permeation behavior are time lag experiments, sorption experiments, chromatographic experiments, and dielectric analysis (DEA) [71, 80-82].

1.5.1. Sorption experiments

Sorption experiments are performed in a cell having a defined diffusant concentration and a temperature control. At $t = 0$, the polymer sample is introduced to the cell and the diffusants uptake is measured in terms of weight increase of the polymer. Sorption experiments can be performed pressure dependently due to the sensitivity of the measuring devices [81]. If low molecular substances diffuse into a polymer sheet of thickness $2l$, the solution of Eq. (14) leads to:

$$\frac{M_t}{M_\infty} = 1 - \frac{8}{\pi^2} \sum_{n=0}^{\infty} \frac{1}{(2n+1)^2} \exp \left\{ \frac{-D(2n+1)^2 \pi^2 t}{4l^2} \right\} \quad (16)$$

where M_t is time dependent relative mass of diffusant, M_∞ is relative mass at saturation, n means order of terms of Fourier series, and D is diffusion coefficient [80, 82].

This equation can be graphically solved with respect to the diffusion coefficient D using a plot of M_t/M_∞ versus $\sqrt{D \frac{t}{l^2}}$ [82], **Fig. 19**, showing sorption curves for different percentages of diffusant uptake. The measured $\frac{M_t}{M_\infty}$ curves increase with different slopes in the short term range before reaching saturation [80].

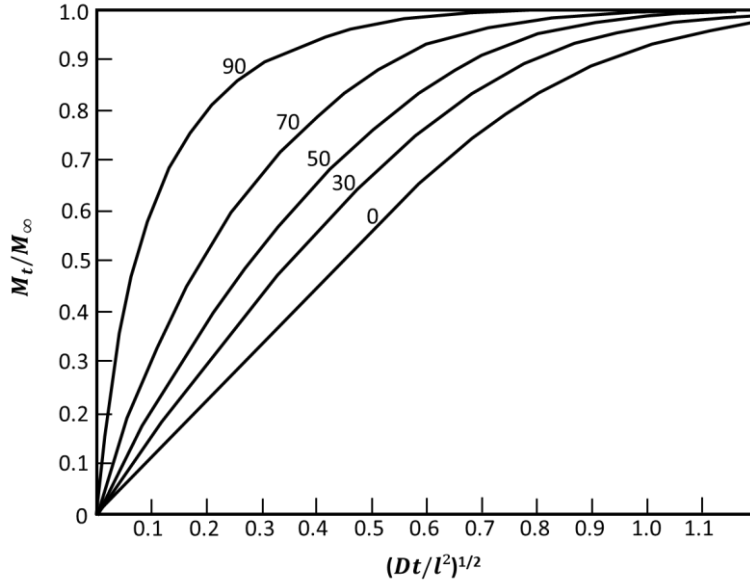


Fig. 19: Sorption curves of a polymer sheet showing different percentages of sorption uptake [80].

For short times with $\frac{M_t}{M_\infty} \leq 0.5$, an approximation is described in literature [83, 84]:

$$\frac{M_t}{M_\infty} = \frac{2\sqrt{Dt}}{l\pi} \quad (17)$$

For long times with $\frac{M_t}{M_\infty} \geq 0.5$ the following approximation is described in literature [80, 82, 84]:

$$\text{sorption} \quad \frac{M_t}{M_\infty} = 1 - \frac{8}{\pi^2} \exp\left(\frac{-D\pi^2 t}{4l^2}\right) \quad (18)$$

$$\text{desorption} \quad \frac{M_t}{M_\infty} = \frac{8}{\pi^2} \exp\left(\frac{-D\pi^2 t}{4l^2}\right) \quad (19)$$

1.5.2. Dielectric analysis

The dielectric analysis (DEA) allows for monitoring of dielectric changes of polymers e.g. during crosslinking of thermosets or to analyze diffusion processes within polymeric materials [82, 85]. The sample is exposed to an alternating external electric field forcing ions to move and dipoles to orientate with respect to this field, **Fig. 20**. Both effects are linked to dissipation of energy due to internal friction. In particular, the motion of an ion in a viscous liquid driven by the electric field corresponds to the motion of a ball in a viscous liquid driven by gravitation.

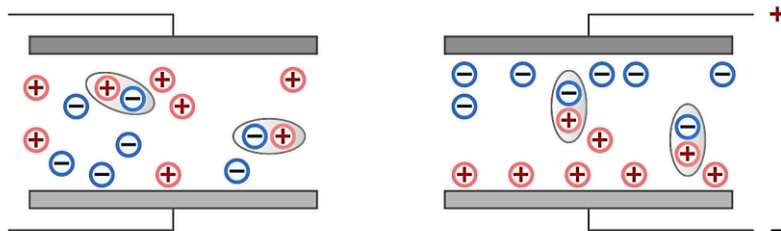


Fig. 20: Measuring principle of the dielectric analysis (DEA) with moving ions and orienting dipoles forced by the applied alternating external electric field.

Commonly, a parallel plate capacitor is used for DEA analysis as it provides a homogeneous electric field in a sample. The use of interdigitated electrode (IDEX) sensors allows to measure at the bottom of the sample and to manipulate on the top for e.g. determining depth dependent curing rates of dental resins [86, 87]. IDEX sensors with comb-shaped and intermeshing electrodes measure the dielectric properties over an area of (5x7) mm² of a sample, **Fig. 21**.

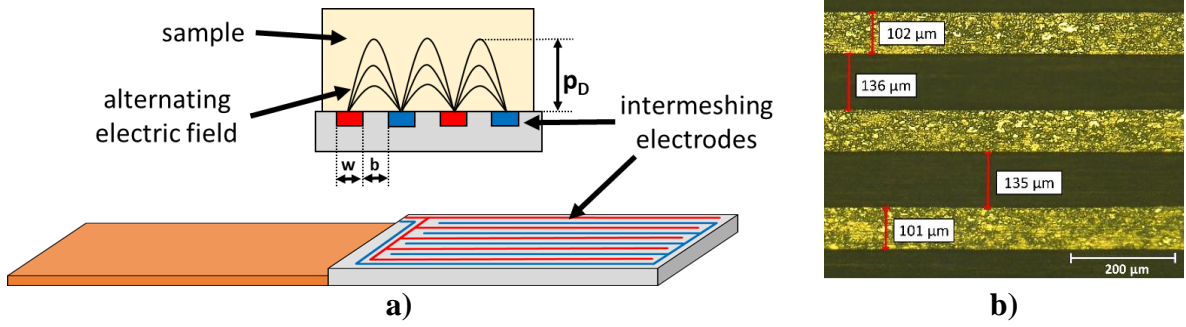


Fig. 21: Design of an IDEX sensor with intermeshing electrodes and resulting alternating electric field a). Microscopic picture of IDEX sensor with an electrode width $w \approx 100 \mu\text{m}$ and a distance between electrodes $b \approx 130 \mu\text{m}$ b).

The penetration depth of the electric field of a comb-shaped IDEX sensor depends on the width of the electrodes and the electrode distance [88]:

$$p_D \cong \frac{b+w}{\pi} \quad (20)$$

For the Mini-IDEX sensor having the dimensions - width $w \approx 100 \mu\text{m}$ and electrode distance $b \approx 130 \mu\text{m}$ - the penetration depth of the electric field into the sample is given by $p_D \approx 75 \mu\text{m}$.

The investigated quantity during monitoring resin curing processes or diffusion experiments is the frequency dependent ion viscosity η^{ion} being the reciprocal to the ion conductivity σ :

$$\eta^{\text{ion}}(f) = \frac{1}{\sigma(f)} = \frac{1}{2\pi f \epsilon_0 \epsilon''(f)} \quad (21)$$

with frequency f , dielectric loss ϵ'' and dielectric constant ϵ_0 [89, 90]. According to Wittchen et al. [82], Penon et al. [91], Gong et al. [92] and Ollivier-Lamarque et al. [93] the ion viscosity η^{ion} can be used to investigate diffusion processes as it is sensitive to changes of macromolecule mobility and ion concentration. Both are affected if low molecular substances diffuse into PSA. Therefore, the measured η^{ion} is related to the diffusion coefficient. Wittchen et al. [82] derived:

$$\log \eta^{\text{ion}}(t) = \log A_0 + \frac{B'}{V_g} \frac{1}{1 - \frac{M_\infty \frac{8}{\pi^2} \exp\left(-\frac{D\pi^2 t}{(4l)^2}\right)}{\rho_{\text{solv}}}} \quad (22)$$

where A_0 is pre-exponential factor, B' represents fractional free volume being relevant for mobility and transport, V_g is volume of dry coating, M_∞ stands for amount at infinite time, D is diffusion coefficient and ρ_{solv} is density of the solvent. They verified eq. 22 for swelling polyurethane coatings with respect to temperature and composition, **Figs. 22 and 23**.

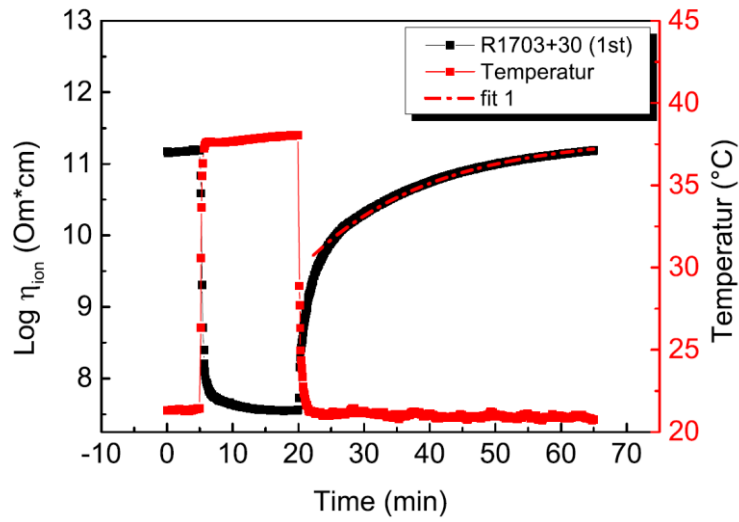


Fig. 22: Effect of temperature on the ion viscosity during desorption [82].

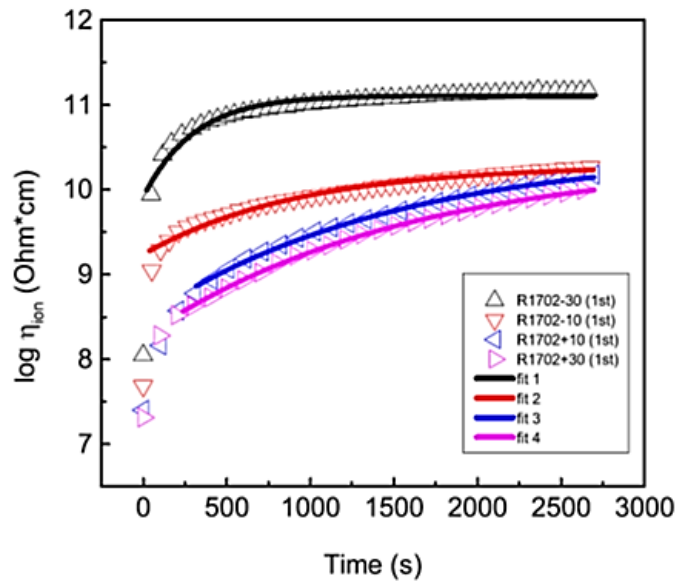


Fig. 23: Desorption curve of polyurethane with different hardener quantities [82].

Fitting of the η^{ion} curves allows for determining the diffusion coefficient, **Fig 24**.

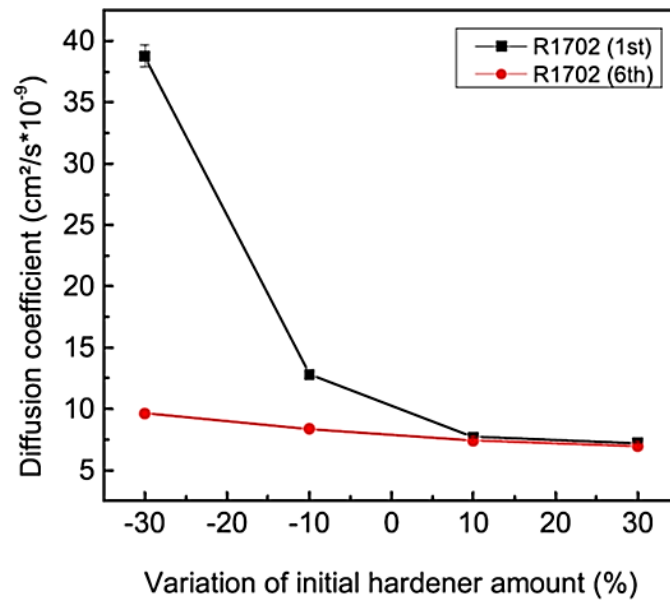


Fig. 24: Effect of variation of hardener amount on diffusion coefficients of two resin compositions [82].

2. Aim of the work

The medical transdermal therapeutic system (TTS) consists of pressure sensitive adhesive (PSA) containing active pharmaceutical ingredient (API) and a protective backing layer, and have to meet high and often opposing requirements arising from a multi-day application time and a traumaless removal.

Standardized testing methods adopted from technical bonding to characterize short- and long-term adhesion of TTS (probe tack, peel and static shear adhesion) use stainless steel or aluminum plates. This does not correspond to application conditions of TTS with respect to adhesion and detaching processes on skin. As a consequence, these methods represent only quality assurance tools and are not capable to provide information about the TTS behavior on human skin (or polymer substrates). Furthermore, it is known that the surface properties and texture of skin differ significantly between human individuals, thus, bad instantaneous adhesion on skin or detaching during the application may endanger the therapy. Optimized performance requires an individualized design of TTS with respect to human skin properties. Therefore, the aim of this work is the development of application related and tailor-made characterizing and testing methods for TTS with the focus on:

- development of a testing approach to determine adhesion and detaching of PSA/TTS
- viscoelastic properties of PSA/TTS subjected to small and large deformations
- determination and evaluation of the diffusion behavior of water-based liquids into the PSA, also considering cross-interactions with API and their effects on the viscoelastic properties.

The viscoelastic properties at application-relevant frequencies determine the adhesion and detaching behavior of PSA (investigated by SAOS measurements). For high skin motion, LAOS can be used to correlate the adhesive behavior at large deformation amplitudes. As standardized testing methods are not sufficient to characterize application relevant adhesion behavior, a new testing approach has to be developed regarding the stiffer and flexible backing layer.

The dielectric analysis using IDEX sensors allows for the investigation of the diffusion behavior of e.g. water under conditions close to application, as water absorption affects the mobility of ions and dipoles in the polymer. In principle, it can be used on the patients' skin during therapy.

The long-term goal of this work is to provide a methodology of an application-related TTS characterization leading to the development of individualized medical patches with optimized performance resulting in safer TTS products.

3. Materials and Methods

The materials used in this study were commercially available amine-compatible (AC) BIO PSA 7-4201 (medium tack) [94] and BIO PSA 7-4301 (high tack) [95] along with non-amine compatible (NAC) BIO PSA 7-4501 (high tack) [96] and BIO PSA 7-4601 (medium tack) [97] silicone PSA's (DuPont and Dow Health Care Solutions.) with resin contents between $v_F = 49.1$ and 54.2 Vol% and mixtures of it according to **Table 3**.

Table 3: Composition of PSA samples used [94-98].

Amine compatible (AC)			Non-amine compatible (NAC)		
ratio BIO PSA 4201:4301	Weight content (%)	Volume content (%)	ratio BIO PSA 4501:4601	Weight content (%)	Volume content (%)
100:0	60.00	54.2	100:0	60.00	54.2
75:25	58.75	52.9	-	-	-
50:50	57.50	51.6	50:50	57.50	51.6
25:75	56.25	50.4	-	-	-
0:100	55.00	49.1	0:100	55.00	49.1

PSA laminates of these compounds with a thickness of (150 ± 15) μm were produced on a release liner by using a coating box. These PSA layers were either laminated with a second release liner or a PET/EVA backing layer (3M Scotchpak™ 9732) [98], resulting in AC- and NAC-PSA or AC- and NAC-TTS samples, respectively.

Testing of the PSA / TTS characteristic properties was performed with the following measuring devices, **Table 4**:

Table 4: Measured properties, determined quantities, tested samples and instruments.

Category/ property	Measured quantity	Tested sample	Instrument
Probe Tack [60]	F	TTS	Polyken Probe Tack Tester (ChemInstruments, Fairfield, USA)
Adhesion strength [63]	$F(t)$	TTS	ZwickRoell Z005 with force transducer Zwick 100 N (Zwick, Ulm, Germany)
Rheology - amplitude sweeps (SAOS/LAOS) [99]	$G'(\gamma_0); G''(\gamma_0); I_{3/1}(\gamma_0); S(\gamma_0); T(\gamma_0)$	PSA	MCR702 TwinDrive® (Anton Paar, Austria)
Diffusion kinetics [100]	$\eta^{\text{ion}}(t)$	PSA	DEA288 Ionic (NETZSCH Gerätebau, Germany)
Water absorption [100]	$m(\text{H}_2\text{O}; 0.9\% \text{ NaCl})$	PSA	Mettler Toledo AX205 DeltaRange (MettlerToledo, Columbus, USA)
Glass temperature, thermal expansion [100]	$T_g; \alpha_{L,G}; \alpha_{L,L}$	PSA	DMA 242 E Artemis (NETZSCH Gerätebau, Germany)
<i>RheoTack</i> [101, 102]	$F(h)$	TTS	Haake MARS III (Thermo Fischer Scientific, USA)

Probe Tack measurements were performed after instrument calibration in accordance to the manufacturer's procedure according to ASTM D2979 [60] with a stainless steel plate P5 $\text{\O} = 5$ mm.

Peel adhesion properties of TTS were measured towards stainless steel plates according to DIN EN ISO 29862 [63] in 180° angle. Therefore, TTS were applied on stainless steel plates by hand and pressed with a 2 kg roll. After a dwell time of 1 min, peel adhesion was measured within a tensile testing machine with a retraction speed of 300 mm/s.

The SAOS/LAOS amplitude sweeps of PSA's were performed within a separate motor-transducer (strain controlled) mode with a plate-plate arrangement having a diameter of $\text{\O} = 15$ mm at 30°C and testing frequencies of $\omega = 0.6, 1, 2,$ and 4 rad/s. To ensure contact, an initial axial compression force of 5 N was applied for 15 s and released afterwards to 0 N to allow the PSA's a relaxation time of 600 s ($v_F = 49.1$ to 50.4%) or 900 s ($v_F = 51.6$ to 54.2%), before the measurement started [99].

Diffusion kinetics of 300, 600, and 900 μm thick PSA's were investigated within a temperature controlled ($T = 30^\circ\text{C}$) setup, where a mini-IDEX sensor monitors the ion viscosity change η^{ion} at 10 Hz from the bottom after adding deionized water or a 0.9 % NaCl solution on the PSA's top surface [100].

Saturation level of PSA's water and 0.9 % NaCl-solution absorption within 24 h at 30°C immersion was determined of stacked PSA films having a sample size of $20 \times 40 \times 0.6$ mm³, after the PSA films were dried at 80°C for 24 h [100].

DMA tension mode measurements of stacked PSA sheets with a sample size of $6.5 \times 12 \times 1$ mm³ were performed after instrument calibration in accordance to the manufacturer's procedure at a frequency of 1 Hz, a clamping length of 10 mm, a dynamic force amplitude of 25 μm , and a maximum force amplitude of 10.9 N between -170 and $+80^\circ\text{C}$ with a 40 min isothermal conditioning step and a subsequent heating rate of $2^\circ\text{C}/\text{min}$. From these measurements, the glass transition temperature T_g at the maximum of the loss modulus $E''(T)$ and loss factor $\tan(\delta)(T)$ were determined. Additionally, the coefficient of thermal expansion (CTE) by the length change of the $\Delta L(T)$ -curve were evaluated in the glassy and the liquid state $\alpha_{L,G}$ and $\alpha_{L,L}$, respectively [100].

During the *RheoTack* measurements the force-retraction displacement (F - h) curves were measured in tension and compression mode within a commercially available rheometer that allows the installation of exchangeable rod geometries as upper plate (stainless steel plate P8 $\text{\O} = 8$ mm, stainless steel plate P5 $\text{\O} = 5$ and a spherical rounded rod R5 $\text{\O} = 5$ mm and $D_{\text{sphere}} = 12$ mm). The lower plate was replaced by a temperature module plate (TMP) exhibiting a borehole of $\text{\O} = 12$ mm, where TTS samples were attached upside down. The rods were moved downward with a speed of 0.1 mm/s until a contact force of 0.2 N was reached, hold for 1 s, and then retracted with $v_{\text{retract}} = 0.01, 0.1$ and 1 mm/s [101, 102].

4. Discussion of the results

4.1. Rheological properties – shearing of PSA and TTS

TTS are applied to human skin between 1 and 7 days, where they are subjected to small and large deformations as skin can be strained up to 40 % [103-105]. Therefore, an application-related rheological frequency dependent characterization of the PSA and TTS in the short and large amplitude oscillatory shear regions was performed.

4.1.1. Amplitude sweeps of PSAs within short amplitude oscillatory shear [99]

Amplitude sweeps in the short amplitude oscillatory shear (SAOS) region allow for the determination of the viscous- and gel- or solid-like material behavior. Furthermore, information about the resin dependent shear moduli and the range of the linear viscoelastic region (LVR) can be obtained. **Fig. 25** shows standard amplitude sweeps of the PSAs with various v_F . Both PSAs exhibit increasing shear moduli (storage- G' and loss-modulus G'') with increasing v_F and a transition from solid-like ($G' > G''$) to viscous-like behavior ($G'' > G'$) within the measuring range, **Appendix Fig. A1**.

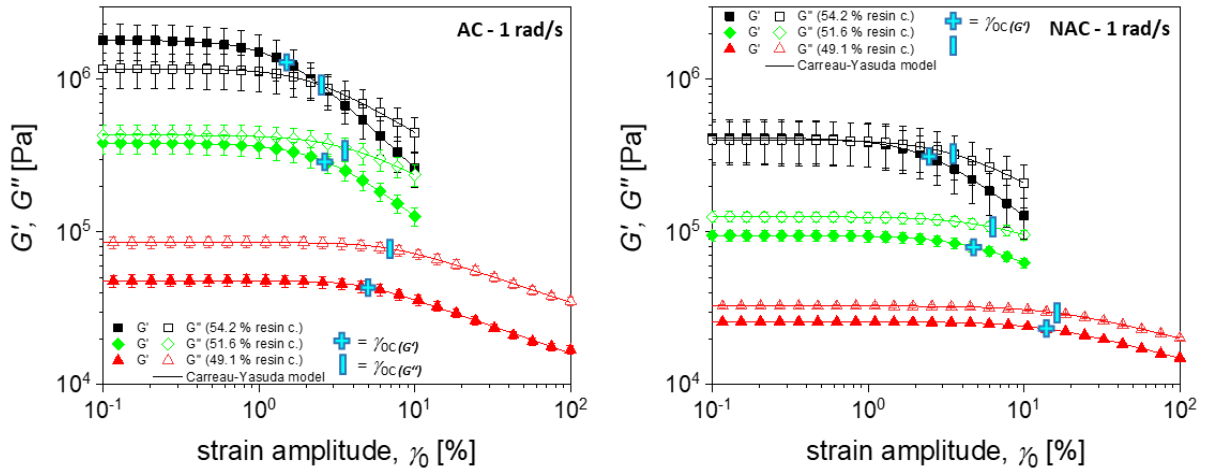


Fig. 25: Strain amplitude dependent storage G' and loss moduli G'' of AC- and NAC-PSAs for $\omega = 1$ rad/s; symbols = measured data; lines = Carreau-Yasuda-like fits [99].

The measured amplitude sweep curves, **Fig. 25**, allow for fitting according to the Carreau-Yasuda like model:

$$G'(\gamma_0) = G'_0 (1 + (C_1 \gamma_0)^{C_2})^{\frac{(C_3-1)}{C_2}} = G'_0 \left(1 + \left(\frac{\gamma_0}{\gamma_{0c}} \right)^{C_2} \right)^{\frac{(C_3-1)}{C_2}} \quad (23)$$

$$G''(\gamma_0) = G''_0 (1 + (C_1 \gamma_0)^{C_2})^{\frac{(C_3-1)}{C_2}} = G''_0 \left(1 + \left(\frac{\gamma_0}{\gamma_{0c}} \right)^{C_2} \right)^{\frac{(C_3-1)}{C_2}} \quad (24)$$

with G' as the storage modulus, G'' as the loss modulus and the parameter C_1 , which represents the transition from the linear to the nonlinear viscoelastic region. C_2 stands for the range of the transition factor for strain amplitudes from the end of the linear region to the beginning of the strain amplitude-dependent decrease. The factor C_3 defines the strain amplitude dependency of G' and G'' within the nonlinear range. As G' and G'' decrease at higher strain amplitudes,

according to the rheological interpretation of Sim et al. [106], the strain amplitude curves can be classified as type I, which is commonly reported for polymer melts or solutions.

The ν_F -dependent gel point can be estimated at $\approx 51.6\%$ (2 rad/s) for AC- and at 54.1% (1 rad/s) for NAC-PSAs, **Appendix Fig. A1**. Furthermore, AC- exhibits a two to four times higher G'_0 than NAC-PSAs, which can be explained by the second polycondensation step for the end-group replacement from $-\text{OH}$ to $-\text{CH}_3$, resulting in higher intermolecular interactions and a higher crosslinking density.

From the linear viscoelastic point of view, nonlinear behavior is reached when moduli are dependent on the applied strain amplitude at $\gamma_{0C} < 1/C_1$. For the silicone PSAs, γ_{0C} displays an increasing behavior with decreasing ν_F , whereas γ_{0C} of G'' exceeds those from G' . This can be explained by the decreasing ν_F , thus causing a lower crosslinking degree, lower molecular masses and reduced internal friction which increases the linear viscoelastic range for G' and G'' . For both AC- and NAC-PSAs, C_2 values are close to 2 and show a comparable value to the shear rate-dependent melt viscosity of polymers resulting from the original Bird-Carreau model. However, AC exhibits slightly higher values than NAC, indicating that C_2 is sensitive to the chemical modification. Thus NAC shows a broader transition zone which could indicate higher branched molecules for NAC- than AC-PSAs [107]. C_3 displays a less pronounced softening behavior the closer the values approach 1. The decreasing ν_F causes increasing C_3 values, indicating more liquid- or gel-like behavior for AC- and NAC-PSAs in terms of rubber elasticity.

Chang und Dahlquist evaluation [99]

The linear viscoelastic data allows for the representation according to Chang [108] and Dahlquist [109], which shows that the frequency-dependent data pairs (G' , G'') lay on master curves starting in the liquid phase (data points below the $\tan(\delta)=1$ line) and end up in the solid state (data points above the $\tan(\delta)=1$ line), **Fig. 26**. As the slope of the AC-PSA master curve is higher than that for NAC-PSA, the viscoelastic properties of AC-PSA vary more. Furthermore, the Dahlquist criterion line represents an estimation of the gel point as the master curves cross the Dahlquist and the $\tan(\delta)=1$ lines in the same moduli range.

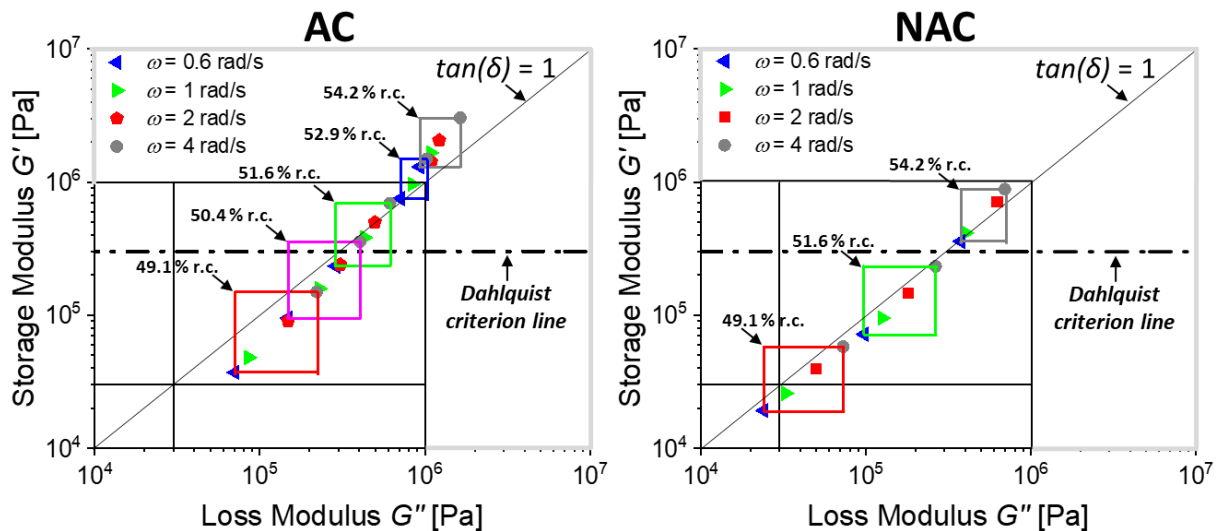


Fig. 26: Representation according to Chang and Dahlquist of SAOS data from AC- and NAC-PSAs [99].

4.1.2. Rheological characterization of PSA within large amplitude oscillatory shear [99]

In the MAOS and LAOS range, beyond the LVE, the non-sinusoidal character of the response signal contains contributions of the higher harmonics as the 3rd (I_3), 5th (I_5) and 7th (I_7). The ratio $I_{3/1}$ as a result from Fourier analysis represents a measure for the nonlinear behavior and shows a slope of $n = -1$ due to instrument noise [110] within the SAOS range until it increases in the MAOS range with a slope between $n = 1.6$ to 2.3 , **Fig. 27**. The frequency dependent nonlinear “oddities” between the instrument noise and the MAOS region range between a slope of $n = 0$ for AC-PSAs and a local maximum. Especially NAC-PSAs exhibit strong local maxima, **Fig. 27**. As $I_{3/1}$ slopes with $n = 0$ have been reported as early evidence for consolidation of percolated networks or gelation in suspensions [78], local maxima have not been reported yet, but indicate possible molecular processes as stretching or release of physical cross-links which are not accessible in SAOS rheology.

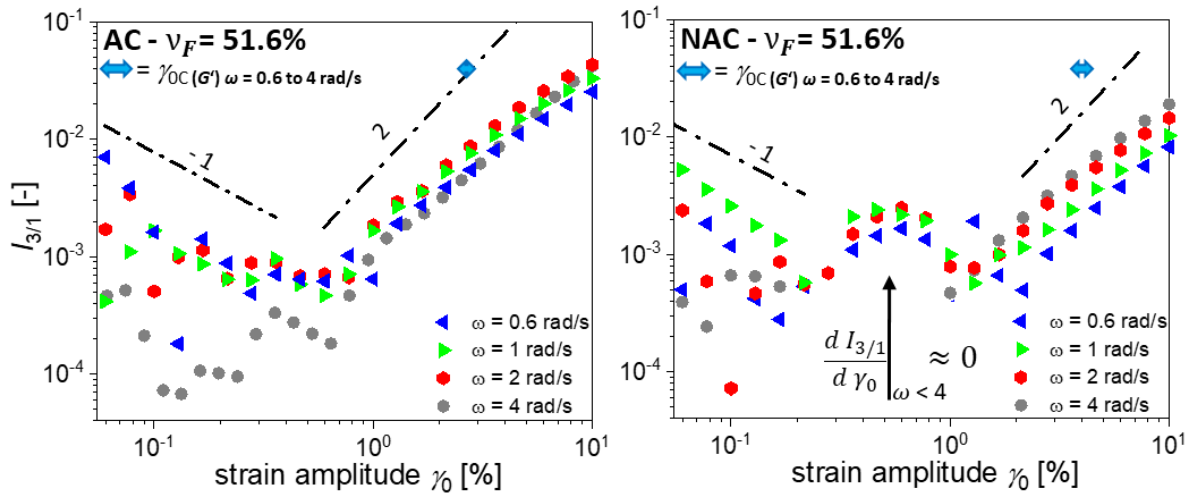


Fig. 27: Strain amplitude dependent nonlinear parameter $I_{3/1}(\gamma_0)$ for AC- and NAC-PSAs [99].

Intra-cycle quantification from monitored shape changes of the elastic and viscous Lissajous-Bowditch diagrams, results in the strain stiffening S and shear thickening T ratio, which are both approximately $S = T = 0$ for all AC- and NAC-PSAs within the linear viscoelastic range, **Fig. 28 and 29**. The onset of both parameters $S, T \neq 0$ where nonlinear behavior occurs can be detected at higher strain amplitudes than the limit of the LVE (determined from G' and G'') but is lower than from the $I_{3/1}$ data. Furthermore, the onset of the parameters $S, T \neq 0$ where intra-cycle nonlinearity occurs decreases with increasing v_F , due to a reduced chain mobility, which was also found by other researchers [78, 111-116]. The parameter S for AC-PSAs show a frequency dependency, a maximum and a wave-like response for $v_F = 49.1\%$, while the maxima is shifted to lower strain amplitudes with increasing v_F and frequency. For higher v_F , maxima may be assumed at higher strain amplitudes, outside of the measuring range. For the NAC-PSAs maxima of S cannot be observed which might be a consequence of too small strain amplitudes. This detected intra-cycle strain stiffening behavior of S , for AC- and NAC-PSAs in varying levels, might be attributed to the stretching and yielding of the molecular network as reported by [113, 116, 117].

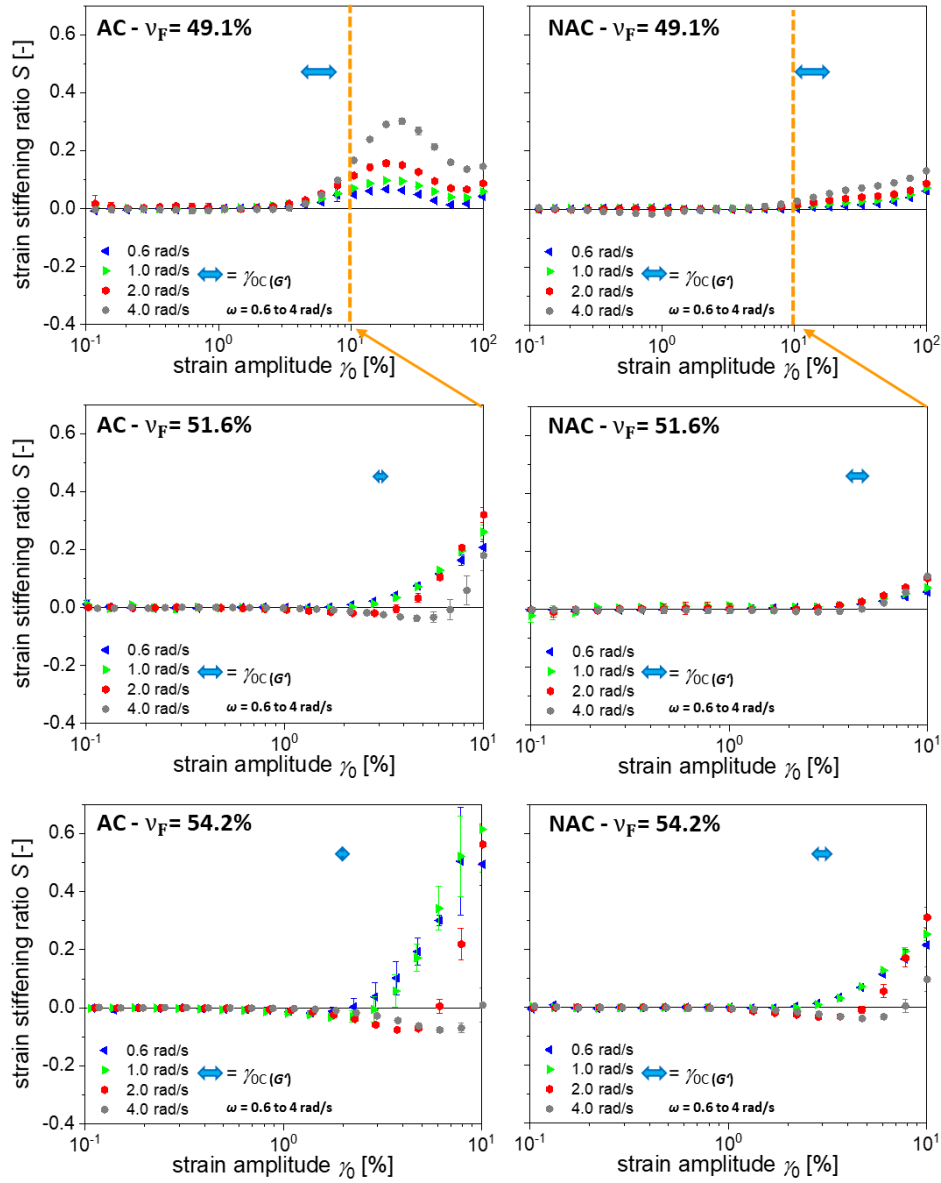


Fig. 28: Strain amplitude and frequency dependent strain stiffening ratios S for AC- and NAC-PSAs [99].

Fig. 29 shows the viscous nonlinear behavior with the shear thickening T ratio, displaying a v_F and frequency dependency for both, AC- and NAC-PSAs. AC-PSAs with $v_F = 49.1\%$ display an intra-cycle transition from shear thickening ($T > 0$) at moderate strain amplitudes to intra-cycle shear thinning ($T < 0$) at higher strain amplitudes. Whereas both PSAs with $v_F > 51.6\%$ display a strongly frequency dependent intra-cycle transition from shear thickening to shear thinning. As the shear thickening maxima are shifted to lower strain amplitudes with increasing v_F and decreasing frequencies, one may assume that the shear thickening behavior occurs initially before a shear thinning behavior is attained at higher strain amplitudes, similar to the PSAs with $v_F = 49.1\%$. Various researchers [111, 112, 115, 116] reported similar findings with increasing polymer concentrations / filler contents and explained these findings with the creation of a shear induced filler network or gelation due to particle-particle interactions or physical cross-links at moderate strain amplitudes. A further increase of the applied strain amplitude causes the orientation of the polymer chains or stretching of the network and may finally lead to the destruction of the shear induced network.

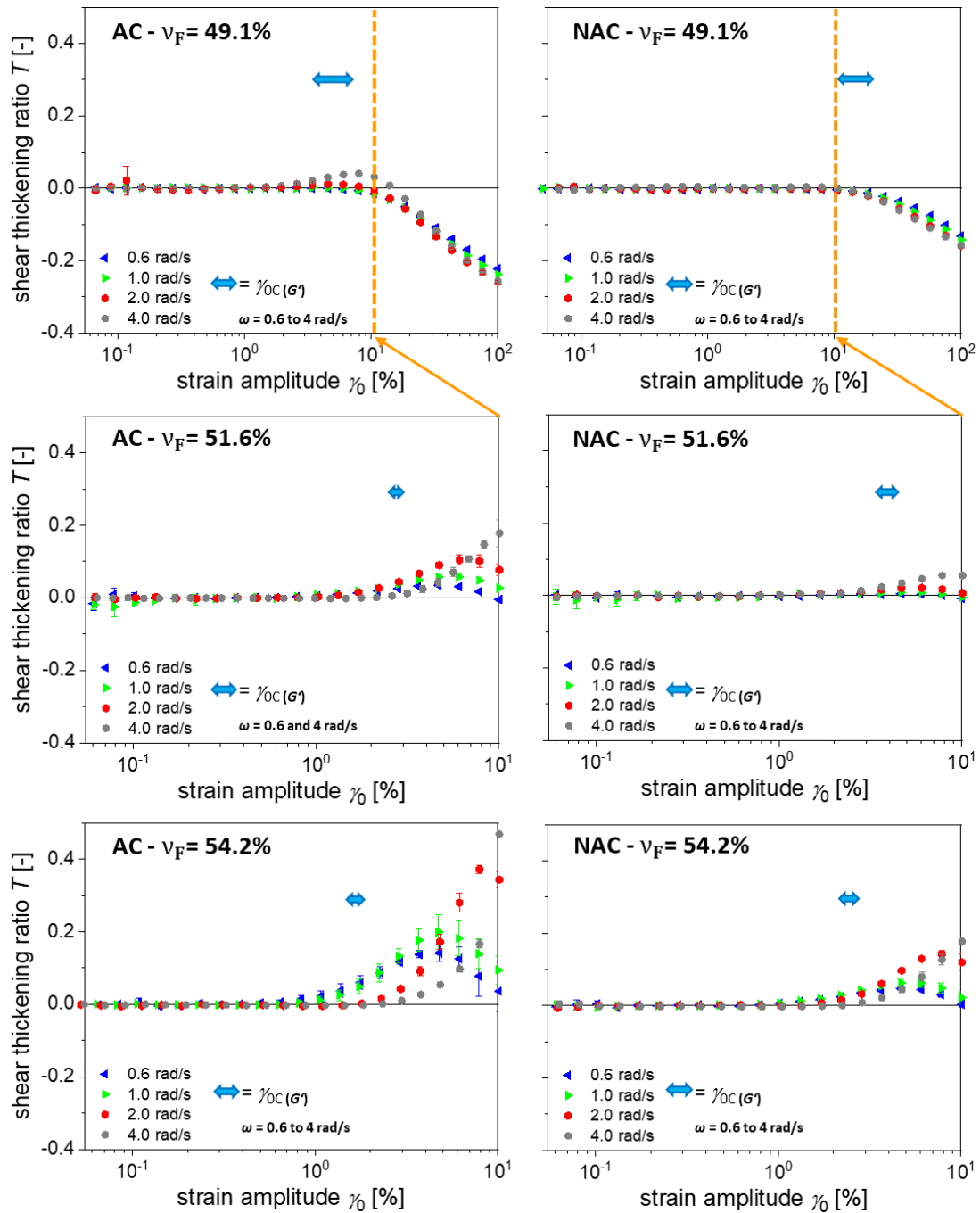


Fig. 29: Strain amplitude and frequency dependent shear thickening ratios T for AC- and NAC-PSAs [99].

4.2. Diffusion properties [100]

During the application of TTS on human skin, sweat and individual skin characteristics affect the adhesion of TTS to the skin. However, as evaporation of water molecules is prevented by an occlusive backing layer that covers TTS, water and sweat released from the skin possibly diffuses into the PSA and might affect the PSA's mechanical properties and its adhesion behavior. Therefore, the effect of diffusing molecules as deionized water and a 0.9 % NaCl solution into the PSA was investigated.

4.2.1. Diffusion into PSA monitored with DEA [100]

For monitoring the diffusion kinetics of deionized water and 0.9 % NaCl solution into silicone AC- and NAC-PSAs, the dielectric analysis (DEA) within a temperature controlled fringe field mini-IDEX sensor setup was used, **Fig. 30 a-c)**. The openings in the PTFE covering plate allowed for the installation of a thermocouple, a sealant and for the addition of the diffusant onto the PSAs surface.

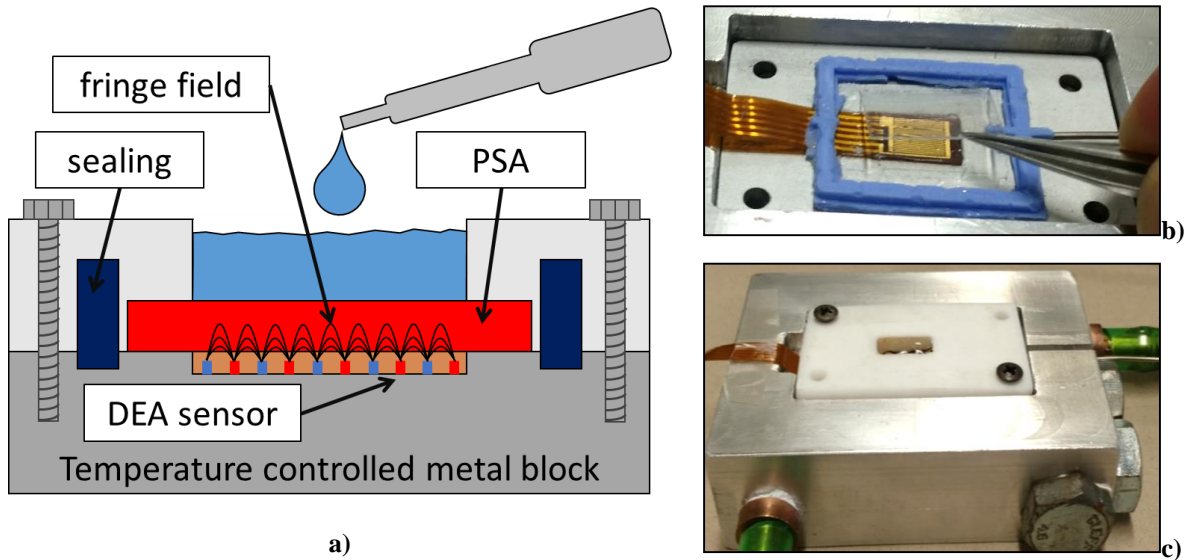


Fig. 30 a-c): Cross sectional sketch of the experimental setup with a temperature controlled metal block, sealing, the dielectric analysis mini IDEX-sensor, the fringe field of the DEA sensor, the PSA-film and the applied diffusant on the PSA-film a), stacked PSA-films are positioned on the mini-IDEX sensor, enclosed by the sealant b), water-temperature controlled aluminum-block with PTFE-covering plate, added onto the mini-IDEX sensor setup [100].

Fig. 31 shows the initial water concentration $c_{\text{H}_2\text{O}}(t=0)$ (red lines) at d_{PSA} , the final water concentration in the PSA $c_{\infty}^{\text{PSA}}(t \rightarrow \infty)$ (blue lines) and the time dependent water concentrations $c_{\text{H}_2\text{O}}(t)$ before the saturation level is reached. The water molecules diffuse from the right side, the position $x = d_{\text{PSA}}$, into the PSA of the TTS and are detected within the sensitivity range of the mini-IDEX sensor of $d_{\text{max}} = 3d_{\text{penetration}} \approx 200 \mu\text{m}$, as the electric field decreases by $1/e$ until $d_{\text{penetration}}$.

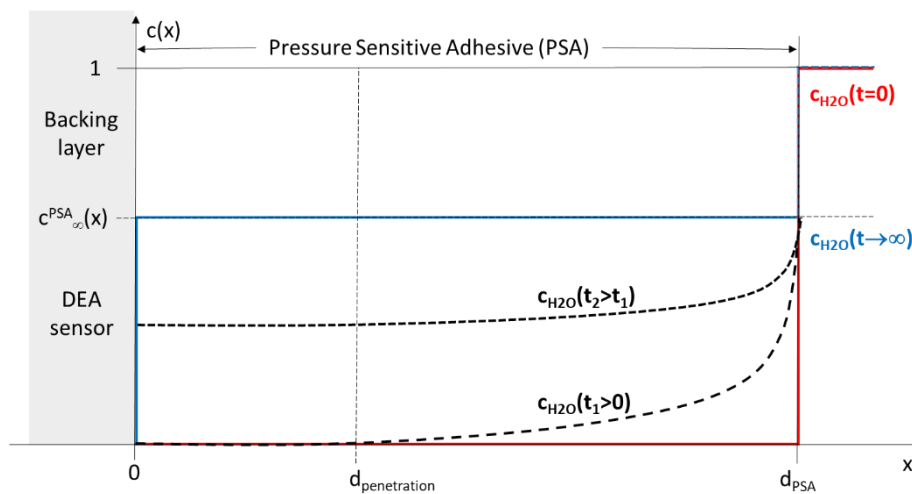


Fig. 31: Increasing water concentration in a PSA, depending on time and space [100].

Fig. 32 shows a schematic time dependent DEA curve that monitors the diffusion process of deionized water into a silicone PSA, resulting in an η^{ion} -time curve. Before the addition of water, η^{ion} displays a stable signal until it decreases asymptotically shortly after the addition of water. From that η^{ion} -time curve, the following characteristic parameters can be extracted:

- constant initial ion viscosity η_0^{ion}
- final ion viscosity η_∞^{ion}
- ion viscosity $\eta_{\tau_{25}\%}^{\text{ion}}$, 25 % below η_0^{ion}
- time $\tau_{25}\%$ at $\eta_{\tau_{25}\%}^{\text{ion}}$
- ion viscosity $\eta_{\tau_{63}\%}^{\text{ion}}$, 63 % below η_0^{ion} and
- time $\tau_{63}\%$ at $\eta_{\tau_{63}\%}^{\text{ion}}$.

Evaluation of the η^{ion} -time curves display decreasing η_0^{ion} and η_∞^{ion} with increasing thickness, at least partially, **Appendix Table B1 and B2**. It can be assumed that constant values of η_0^{ion} and η_∞^{ion} prior and after diffusant addition and saturation, respectively, occur and depend only on materials investigated but not on sample thickness. Furthermore, the relatively large STD of the ion viscosities η_0^{ion} and η_∞^{ion} indicate possible inhomogeneity's that occur during the stacking process and/or sample handling. Moreover, within the range of the experiment, η_0^{ion} and η_∞^{ion} do not show a resin dependency, which might be attributed to the fact that all investigated PSA's are in the rubbery state with highly mobile polymer phases that a variation of $\nu_F = 5\%$ does not cause large effects.

The times $\tau_{25}\%$ and $\tau_{63}\%$ increase with increasing PSA thickness. Similar findings were reported by Wang and Asaoka [118, 119] for vulcanized silicone rubber and dental resin components. Moreover, the times $\tau_{25}\%$ and $\tau_{63}\%$ of NAC are about double of the times of AC, which can be explained by the polar $-\text{OH}$ end-groups within NAC-PSA leading to polar interactions with the diffusant and therefore restraining the diffusion rate. This restraining behavior of the diffusant does not occur for AC-PSA with its $-\text{CH}_3$ end-groups. Furthermore, the times $\tau_{25}\%$ and $\tau_{63}\%$ do not show significant difference, with respect to the STD, between deionized water and 0.9 % NaCl solution, due to the low concentration of NaCl ions.

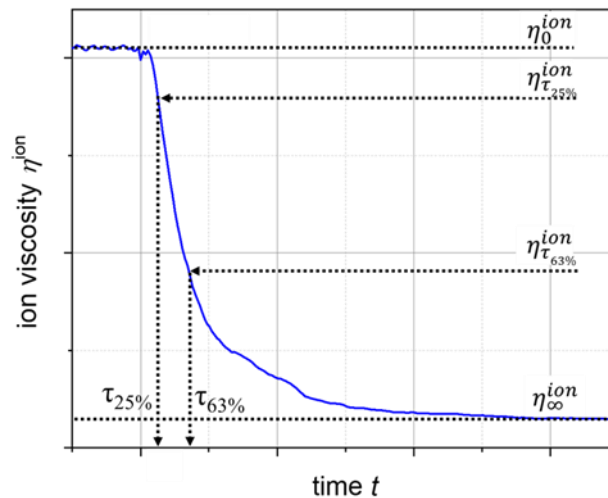


Fig. 32: Time dependent η^{ion} -time curve from the DEA to monitor the process of diffusing water into a silicone PSA, with characteristic evaluated points [100].

Thermal coefficient of expansion (CTE) before and after the glass transition temperature T_g was determined by DMA, to calculate temperature dependent relative free volume v_{free} for evaluation of η^{ion} -time curves and the diffusion coefficients. The results from DMA measurements displayed a T_g at the maximum of $\tan(\delta)$ at -120 °C, being independent of the PSA's v_F , **Appendix Table B3**. The CTE in the glassy state, approx. $450 * 10^{-6}/\text{K}$, increased with decreasing v_F and are roughly half of the CTE in the liquid state, approx. $900 * 10^{-6}/\text{K}$, which do not show a v_F dependency, from which a v_{free} of around 10 % can be calculated, **Appendix Table B3**. Furthermore, for diffusion coefficient evaluation, water uptake m_{∞} of the PSAs had to be determined. The results showed that the AC- and NAC-PSAs absorbed hardly any water but the polar $-\text{OH}$ groups of NAC cause a clearly higher water uptake than the nonpolar $-\text{CH}_3$ groups of AC, **Appendix Table B3**. Furthermore, m_{∞} displays for deionized water increasing values with decreasing v_F for AC- and NAC-PSAs due to decreasing v_F and subsequently increasing v_{free} . On the contrary, uptake of 0.9 % NaCl decreases with decreasing v_F for AC-PSAs while results remain constant for NAC-PSAs.

Based on the small amounts of water uptake, it can be assumed that the water diffuses rather as vapor within the free volume of the PSA. Therefore, the following equation can be evolved by combining the equations of Crank [80], Zahouily et al., Fieldson, Lee, Zeghbroek, and Doolittle [120-124] for describing the diffusion process for sample thicknesses ($d_{\text{max}} > d_{\text{PSA}}$), monitored with the DEA:

$$\lg \eta^{\text{ion}}(t, \omega) = A + B + \frac{\frac{B}{v_{\text{free}}}}{1 + \left\{ 1 - \frac{8}{\pi^2} \frac{d_{\text{PSA}}}{d_{\text{max}}} \sin\left(\frac{\pi d_{\text{max}}}{2 d_{\text{PSA}}}\right) \exp\left(\frac{-t}{\tau_{\text{diff}}}\right) \right\}} \quad \text{for } d_{\text{max}} > d_{\text{PSA}} \quad (25)$$

with the ion viscosity η^{ion} , the contribution of the final ion concentration to the ion viscosity A , the Doolittle material constant B , the free volume v_{free} , the thickness of the PSA d_{PSA} , the maximum range of the DEA d_{max} , the time t , and the diffusion time constant τ_{diff} . For the diffusion with ion transport, the initial ion concentration c_{ion}^0 , the constant k_2 , and the maximum diffusant concentration c_{∞}^{PSA} are unknown quantities and can be aggregated to the constant K_2 , resulting in:

$$\lg \eta^{\text{ion}}(t, \omega) = A + B + \frac{\frac{B}{v_{\text{free}}}}{1 + \left\{ 1 - \frac{8}{\pi^2} \frac{d_{\text{PSA}}}{d_{\text{max}}} \sin\left(\frac{\pi d_{\text{max}}}{2 d_{\text{PSA}}}\right) \exp\left(\frac{-t}{\tau_{\text{diff}}}\right) \right\}} - \lg \left(1 + K_2 \left\{ 1 - \frac{8}{\pi^2} \frac{d_{\text{PSA}}}{d_{\text{max}}} \sin\left(\frac{\pi d_{\text{max}}}{2 d_{\text{PSA}}}\right) \exp\left(\frac{-t}{\tau_{\text{diff}}}\right) \right\} \right), \text{ for } d_{\text{max}} < d_{\text{PSA}} \quad (26)$$

with K_2 as a measure of the maximum contribution of absorbed ions on $\eta^{\text{ion}}(t)$ on account of the diffusing ions.

The diffusion time constant τ_{diff} from eq. 25 and 26 allows for the determination of the diffusion coefficient D :

$$D = \frac{4d_{\text{PSA}}^2}{\pi^2 \tau_{\text{diff}}} \quad (27)$$

Influence of chemical composition and PSA-film thickness on the diffusion behavior [100]

The following η^{ion} -time curves were normalized to

$$\lg \eta_{\text{rel}}^{\text{ion}}(t) = \frac{\eta^{\text{ion}}(t)}{\eta_0^{\text{ion}}} \quad (28).$$

Fig. 33 show the influence of the thickness and the chemical composition for the diffusion of distilled water into AC- and NAC-PSAs. Both materials display increasing diffusion times until the final ion viscosity $\eta_{\infty}^{\text{ion}}$ is reached, which can be explained by the longer diffusion lengths which has to be passed by the diffusing water molecules. NAC- exhibits longer diffusion times than AC-PSAs. This can be attributed to the polar $-\text{OH}$ end-groups within the NAC-PSA, causing a slowdown effect due to the established hydrogen bonds with the diffusing water molecules, whereas the AC-PSA features nonpolar hydrophobic $-\text{CH}_3$ end-groups which result in weaker van der Waals forces that delay the diffusing water molecules less than the $-\text{OH}$ end-groups.

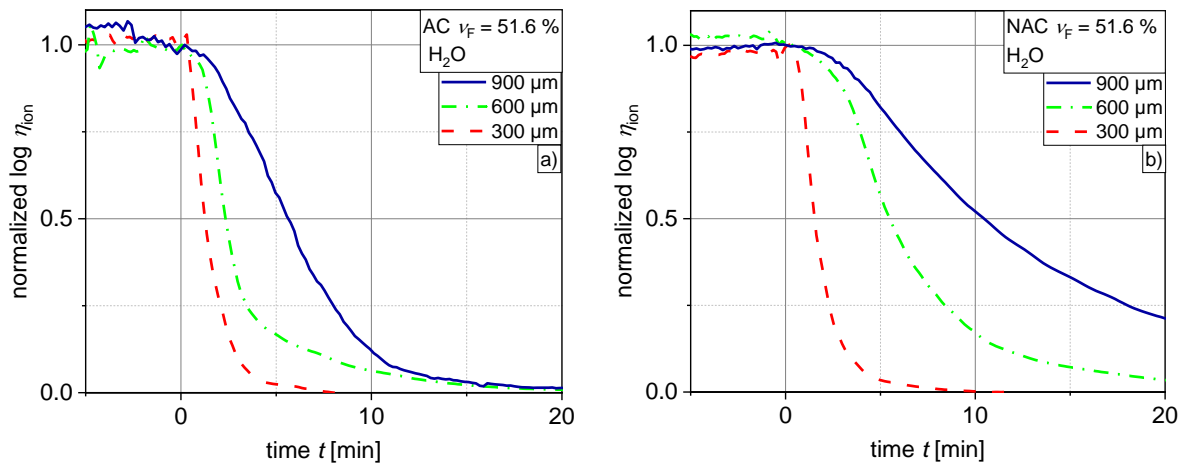


Fig. 33: Ion viscosity (η^{ion}) as a function of time (t) for various film thickness of a) amine compatible (AC) and b) non-amine compatible (NAC) PSA-films (resin content of $v_F = 51.6\%$) [100].

The diffusion coefficients D for AC- and NAC-PSAs were fitted with eq. 25 for deionized water and eq. 26 for 0.9 % NaCl solution. As eqs. 25 and 26 describe the diffusion process only for diffusion time constants $> \frac{\tau_{\text{diff}}}{2}$, starting times of 330 s, 1300 s and 3000 s were chosen for the thicknesses of 300 μm , 600 μm , and 900 μm , respectively. The diffusion coefficients D reveal no thickness dependency, with respect to STD, while D -values of NAC- are lower than those of AC-PSAs, reflecting the hindered and therefore slower diffusion within NAC-PSAs being caused by the formed hydrogen bonds with the $-\text{OH}$ end groups, **Appendix Table B4 and B5**.

Influence of the resin content and PSA-film thickness on the diffusion behavior [100]

Both AC- and NAC-PSAs reveal a v_F dependent diffusion behavior for deionized water, **Fig. 34**. A decreasing v_F leads to higher D -values for AC-PSAs and shorter diffusion times until saturation at $\eta_{\infty}^{\text{ion}}$ is reached, **Appendix Table B4 and B5**. The silicone PSAs are composed of a polymer and a resin phase, where the first phase consists of linear polydimethylsiloxane (PDMS) molecules, while the second phase is a complex cross-linked network that results in a “ball-like” structure [35]. The cross-linked structure of the resin leads to small intra- and

intermolecular distances and causes an inflexibility which results in low molecular motion. Therefore, an obstruction of the diffusing molecules within the resin can be expected. Whereas the linear PDMS molecules are able to rotate and move freely within its range of motion, easing pathways for the diffusing molecules. The increased range of motion results in a higher free Volume v_{free} with decreasing v_{F} and explains the improved diffusion of the water molecules within the non-polar AC-PSA with the lowest v_{F} .

On the other hand, NAC-PSAs displays a contrastive effect – smaller D -values and shorter diffusion times with increasing v_{F} until saturation at $\eta_{\infty}^{\text{ion}}$ is reached, **Appendix B Table 4 and 5**. This result can be explained by an effect that is caused by the polar $-\text{OH}$ end-groups. A lower v_{F} lead to increasing spatial gaps within the PSA, resulting in wider distances of the resin molecules and therefore to $-\text{OH}$ end-groups that can easily interact with diffusing water molecules and cause their obstruction. Whereas a higher v_{F} induce more compact spatial gaps in the PSA, thus leading to smaller distances of the resin molecules. This promotes the interaction of intermolecular $-\text{OH}$ end-groups of the PSA, being blocked by their selves and thus being unavailable for the diffusing water molecules which can diffuse more easily.

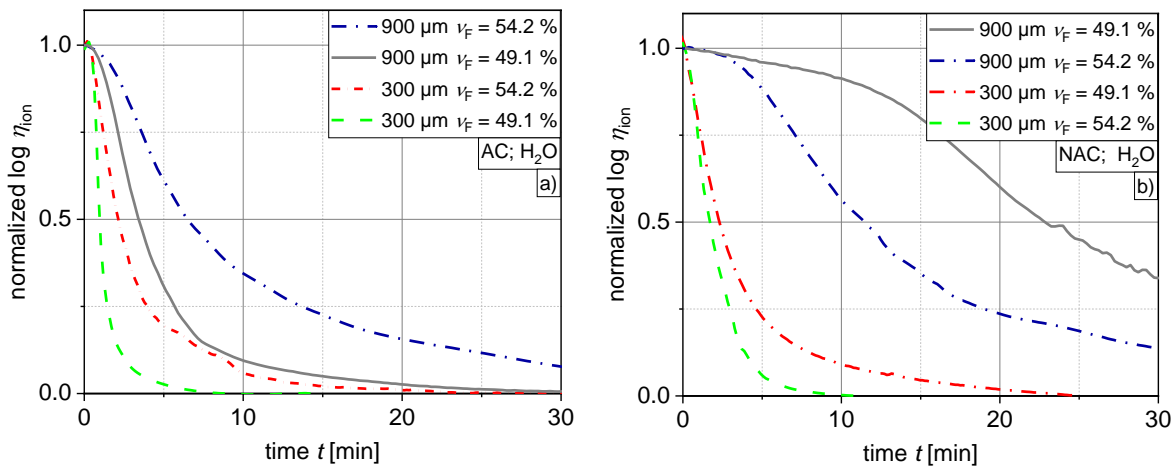


Fig. 34: Influence of the resin content and the PSA-film thickness of amine compatible (AC) a) and non-amine compatible (NAC) PSA-films b) [100].

Influence of the diffusant on the diffusion behavior [100]

The influence of the diffusant was investigated by using an isotonic 0.9 % NaCl solution for the diffusion measurements within the AC- and NAC-PSAs. The $\eta^{\text{ion}}-t$ curves were first evaluated by eq. 25 and subsequently by eq. 26 to quantify the effects of the diffusion ions. The results of eq. 25 showed that the diffusion times and the D -values increase for both PSAs, when a 0.9 % NaCl solution is used, **Fig. 35 and Appendix Table B4 and B5**. This can be explained by the formed hydration shells around the Na^+ - and Cl^- - ions, which increase the size of the diffusing molecules and thus leads to a blocking of diffusion pathways. Furthermore, Millero et al. [125], Marcus [126], Hindman [127], Impey et al. [128], and Heyrovská [129] reported hydration numbers of 3.7, 3.2, 4 and 3.4 for Na^+ and 2, 2.6 and 2.5 for Cl^- , resulting in factor 3.9 and 2.2 higher masses for Na^+ and Cl^- , respectively, thus leading to a reduced diffusion velocity for these hydrated ions. Therefore, the diffusion of NaCl-solution is hindered, and thus slower in comparison to deionized water. [130, 131].

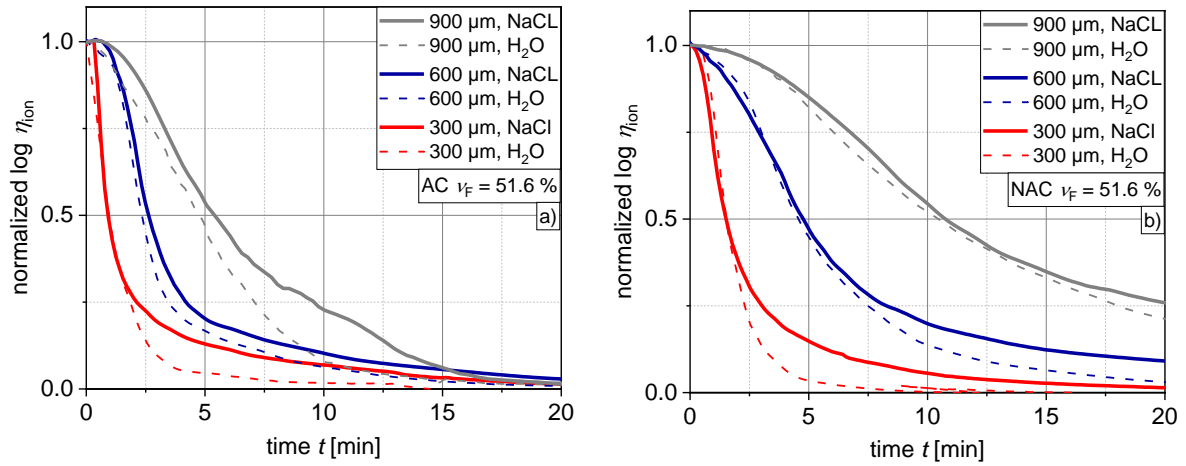


Fig. 35: Influence of the diffusant and the PSA-film thickness of amine compatible (AC) a) and non-amine compatible (NAC) PSA-films b) [100].

The results of eq. 26, with K_2 as representative parameter attributing the effect of diffusing ions, displayed essentially the same D -values from eq. 25 and very small K_2 -values with STD in the range of the mean values, **Appendix Table B6**. Therefore, the diffusion of ions within AC- and NAC-PSAs is negligible.

Additionally, parameter A , eq. 25, contains sample thickness independent initial material properties such as rheological viscosity, ion concentration and ion charge. Moreover, the Doolittle constant B represents a thickness independent material constant. Therefore, a thickness averaging showed that parameter A decreases with decreasing v_F , whereas the Doolittle constant B and D increase with decreasing v_F , **Table 5**. Although the scatter of the STD for A and B are rather large, both parameters are constant for AC- and NAC-PSAs and show a v_F dependency and a differentiation with respect to the chemical composition.

Table 5: Resin content dependent thickness averages of parameter A , parameter B and diffusion coefficients D of AC- and NAC-PSAs [100].

property	AC			NAC		
	diffusant deionized water			diffusant deionized water		
resin content v_F	54.2 %	51.6 %	49.1 %	54.2 %	51.6 %	49.1 %
parameter A	7.0 ± 0.7	6.0 ± 0.7	5.4 ± 0.4	5.8 ± 0.7	5.2 ± 0.2	3.7 ± 1.3
Doolittle constant B	12.5 ± 2.5	24.0 ± 14.9	40.3 ± 20.1	3.3 ± 9.7	41.3 ± 16.4	59.7 ± 4.7
Diffusion coefficient D in $10^{-8} \text{ cm}^2/\text{s}$	145 ± 19	246 ± 5	332 ± 42	129 ± 9	185 ± 2	193 ± 4
	diffusant 0.9 % NaCl-solution			diffusant 0.9 % NaCl-solution		
resin content v_F	54.2 %	51.6 %	49.1 %	54.2 %	51.6 %	49.1 %
parameter A	6.4 ± 0.4	5.8 ± 1.5	5.3 ± 0.7	6.5 ± 0.1	5.7 ± 0.9	5.3 ± 0.8
Doolittle constant B	15.0 ± 3.3	17.3 ± 7.4	22.2 ± 10.7	12.8 ± 5.2	20.0 ± 5.9	34.0 ± 10.2
Diffusion coefficient D in $10^{-8} \text{ cm}^2/\text{s}$	111 ± 9	146 ± 31	232 ± 13	99 ± 4	113 ± 7	172 ± 17

The DEA allows for the investigation of the diffusion properties of deionized water and an isotonic NaCl solution into AC- and NAC-PSAs. The η^{ion} and the diffusion coefficients evaluation show a clear influence of the PSAs chemical composition, its resin content and the diffusant. Therefore, these results from this method lead to a better understanding of occurring diffusion mechanisms within the PSA and this knowledge can be used within further design and development of TTS.

4.3. Adhesion properties

In this thesis, the adhesion properties of silicone-based AC- and NAC-TTS were tested according to standardized testing procedures probe tack (ASTM D2979) [60], adhesion strength (DIN EN ISO 29862) [63] and with the developed testing approach – *RheoTack* [109]. To obtain a deeper insight into these adhesion properties, standard testing was compared with the newly developed approach – *RheoTack*.

4.3.1. Standardized tests – probe tack and shear strength

From the probe tack measurements, only the maximum force during retraction of a standardized stainless steel plate $\varnothing = 5$ mm from the TTS was measured. The results show for both TTS types a decreasing probe tack with increasing v_F , **Fig. 36 a**). This can be explained by the fact that the resin serves as the crosslinking agent, resulting in a denser network [34, 35, 39]. From a higher cross-linking degree, a higher viscosity can be expected [99], leading to a reduced wettability of the probes surface. This can cause a reduced mechanical anchorage of the PSA in the rods surface's pores, and therefore the tack forces decrease with increasing v_F . Probe tack values of NAC-TTS exceed those of AC-TTS by a factor of 1.2 to 10.5 for $v_F = 49.1$ % to $v_F = 54.2$ %, respectively. This could be a result of the end-group replacement from polar –OH to non-polar –CH₃ groups during the second polycondensation step during production of AC-TTS, **Fig. 4**. As a result, a higher molecular weight and a possibly higher cross-linking degree for AC-TTS can be expected [99], leading to a reduced wettability and a lower tack force. Furthermore, these non-polar end-groups cannot create polar interaction with the polar metal surface of the stainless steel rod, and therefore leads to the reduced adhesion.

The peel adhesion testing was performed in 180° angle by retracting a TTS from stainless steel plates with 300 mm/s. As a result, **Fig. 36 b**) shows the mean force of 50 mm retraction distance, quantifying this TTS removal from the metal substrate. In contrast to the probe tack results, the peel adhesion forces increase with increasing v_F , which can be explained by the increasing crosslinking density that leads to a higher cohesiveness of the PSA. Although AC-TTS exhibit nonpolar –CH₃ end-groups, the possibly higher crosslinking density causes 1.02 to 1.2 times higher values of the peel force than those of NAC-TTS.

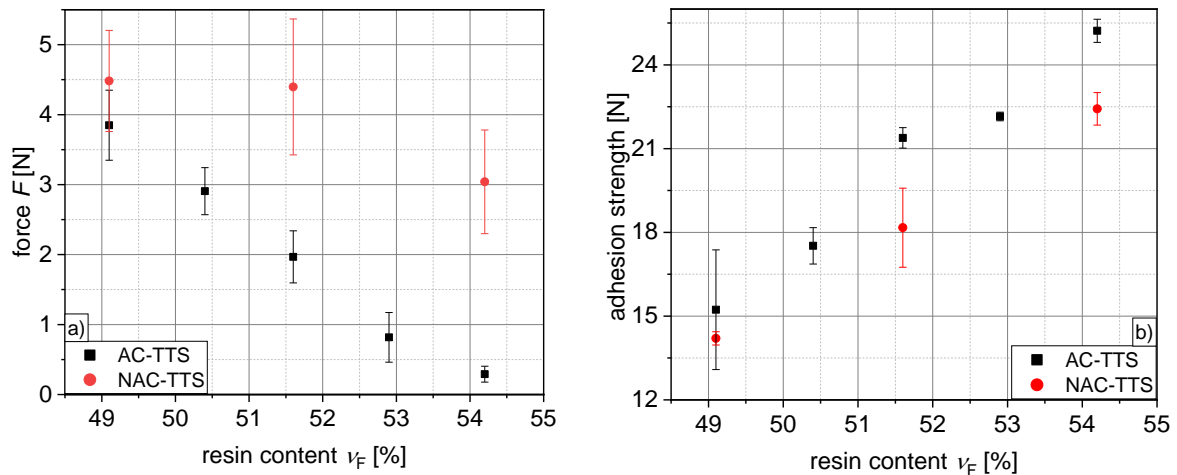


Fig. 36: Resin content dependent results from probe tack a) and peel adhesion strength testing for AC- and NAC-TTS.

4.3.2. *RheoTack* development [101]

To obtain an access to adhesion and detaching properties and detaching mechanisms, an approach using the rheometer's normal force sensor in compression and tension mode was developed. A plate and plate geometry of a rotational rheometer (Haake MARS III, Thermo Fisher Scientific, Waltham, MA, USA) was used to determine the tack behavior of adhesive patches combined with a video monitoring system to record occurring PSA deformations. The new approach called *RheoTack* includes a sample holding ring as an exchangeable temperature module plate (TMP), an optical observation unit consisting of three cameras for synchronized video monitoring, an illumination unit, and exchangeable probe rod geometries, **Fig. 37**.

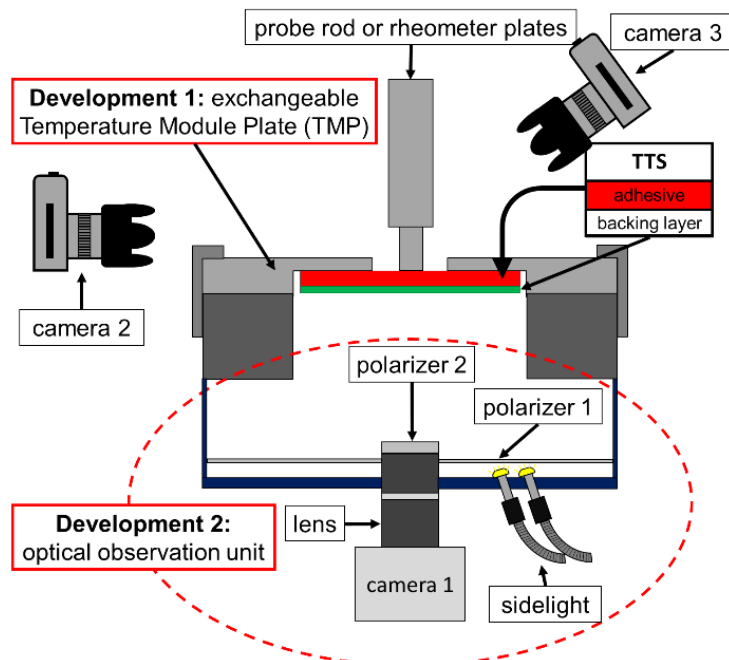


Fig. 37: Sketch of the *RheoTack* approach with the upper plate as the probe rod, the temperature module plate (TMP) for patch fixation as the lower plate, and the implemented optical observation unit for synchronized video monitoring from the bottom (90°, camera 1), lateral (0°, camera 2), and top (45°, camera 3) to the rheometer [101].

4.3.3. *RheoTack* data evaluation and results [101]

The *RheoTack* approach provides a force-retraction displacement ($F-h$) curve with synchronized visual information from video monitoring to obtain a deeper insight into the adhesion and detaching behavior of tapes/patches from the rod. Compared to the standardized probe tack test as a single point measurement [60], the *RheoTack* $F-h$ curve contains significantly more information, as the compression, stretching and fibrillation, and the detaching phase are recorded during tack testing. Furthermore, the following *RheoTack* quantities can be determined from the $F-h$ curve, **Fig. 38**:

- the slope of the $F-h$ curve at the displacement $h = 0$ represents the sample stiffness S ,
- during stretching and fibrillation phase, the initiation force of cavity or fibril formation $F_{\text{start fib}}$ and the corresponding displacement $h_{\text{start fib}}$ can be determined,
- the area under the $F-h$ curve until $F_{\text{start fib}}$ serves as the activation energy of cavity and/or fibril formation $E_{\text{start fib}}$,
- maximum force F_{max} and corresponding displacement h_{max} equals the maximum load capacity of the adhesion system,
- the integral of the entire $F-h$ curve corresponds to the adhesion energy E_{adh} and is a measure for the energy of the complete detaching process.

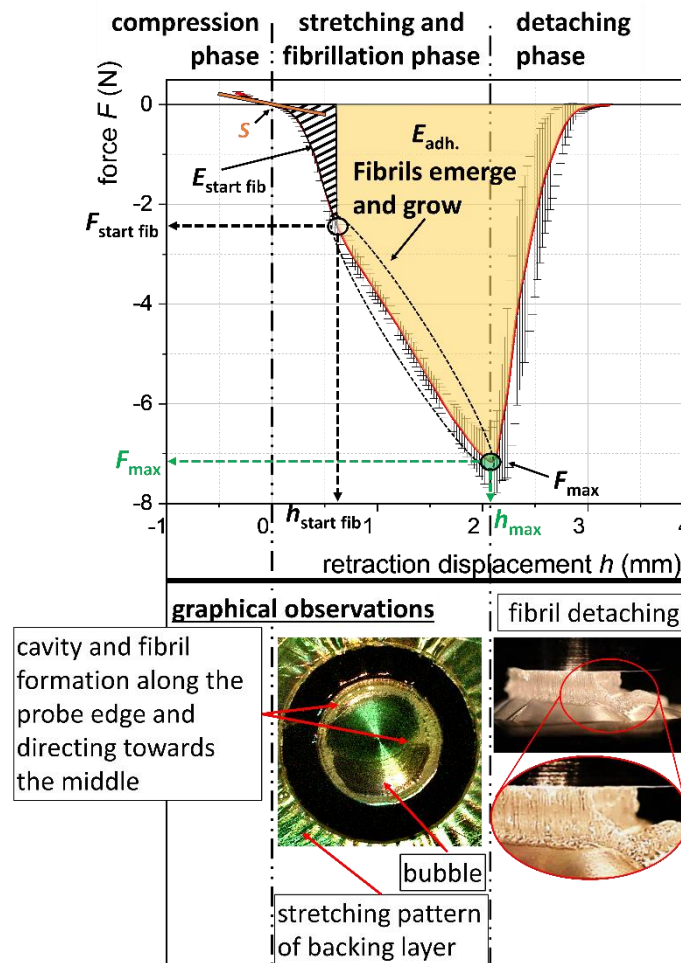


Fig. 38: Evaluation of $F-h$ curve from *RheoTack* testing with deformation phases and characteristic *RheoTack* quantities: S , $F_{\text{start fib}}$, $h_{\text{start fib}}$, $E_{\text{start fib}}$, F_{max} , h_{max} , E_{adh} and corresponding structures at $F_{\text{start fib}}$, and F_{max} (NAC-TTS) [101].

The influence of the following testing and material parameters on the TTS was investigated by evaluating the *RheoTack* quantities [101, 102]:

- retraction speed (v_{retract}),
- resin content (v_F),
- PSA-type (AC, NAC),
- probe rod geometry.

Influence of the retraction speed v_{retract} [101, 102]

In **Fig. 39** the influence of the retraction speed on NAC-TTS with $v_F = 49.1\%$ can be seen, displaying that an increasing v_{retract} causes higher negative forces at the same retraction displacement which is a clear demonstration of the viscoelastic behavior. Additionally, this behavior is also shown by increasing stiffness, decreasing retraction displacements, $h_{\text{start fib}}$, h_{max} , and decreasing adhesion energies $E_{\text{start fib}}$, E_{adh} , **Appendix Table C1**.

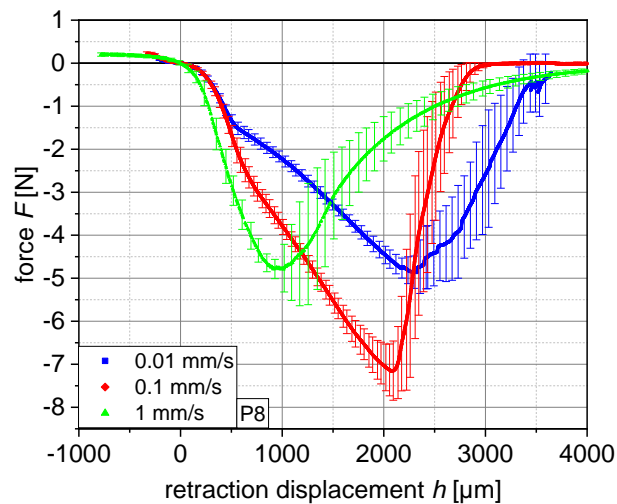


Fig. 39: Mean force F - h curves from *RheoTack* testing at retraction speeds of 0.01, 0.1 and 1 mm/s obtained for five different TTS samples (NAC-TTS 49.1 %) [101].

Furthermore, it was found that an increasing v_{retract} leads to shorter compression phases, **Table 6**, less time for the PSA to wet the probes surface, less mechanical anchorage, and therefore to lower tack values.

Table 6: Retraction speed dependent compression times [102].

Retraction speed [mm/s]	Compression time		
	[s]		
	P8	P5	R5
0.01	27.7	27.9	31.6
0.1	6.0	7.0	9.1
1	3.1	3.3	3.5

Influence of the PSA's resin content v_F [102]

An increasing amount of resin content v_F leads to decreasing force values, retraction displacements and adhesion energies, **Fig. 40**. As the resin serves as a crosslinking agent in the PSA, it causes a network creation during the polycondensation reaction and finally leads to a “bodied” silicone PSA [34, 35, 39]. Thus, with an increasing v_F , an increasing crosslinking density within the PSA can be expected and causes a stiffer material behavior of the resulting TTS. Furthermore, a higher cross-linking density leads to a higher viscosity and reduced wettability of a surface, resulting in a reduced mechanical anchorage of the PSA in the surface's pores. Therefore, the tack forces decrease with increasing v_F , **Appendix Fig. C1, C2 and Table C1**. Moreover, a higher v_F causes a decreased stretchability of the TTS's PSA that results in decreased retraction displacements and correlates with the increase of the cross-linking density.

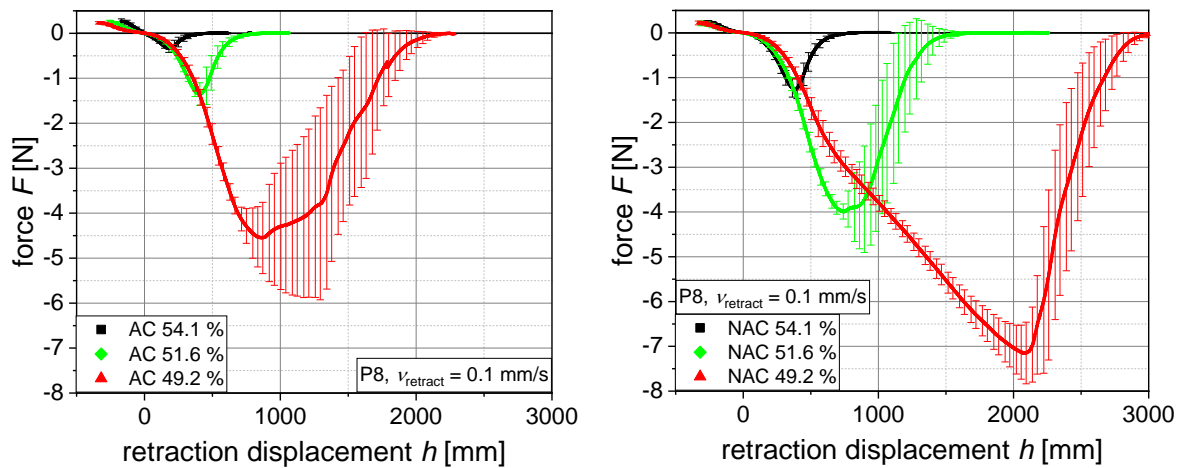


Fig. 40: F - h curves of AC- and NAC-TTS with $v_F = 54.2\%$, 51.6% and 49.1% , tested with retraction speed of $v_{\text{retract}} = 0.1$ mm/s with P8 [102].




Influence of the PSA type (AC, NAC) [102]

For the same v_F , NAC-TTS displays lower stiffness S , higher tack force values, retraction displacements, and adhesion energies than AC-TTS, **Appendix Fig. C1, C2 and Table C1**. This result can be explained by two effects. First, the polar OH-end groups of the NAC-TTS establish more polar interactions with the metal substrates compared to the CH₃-end groups, leading to a better adhesion and higher adhesion energies for the NAC-TTS. Second, the 2nd polycondensation step for the end-group replacement from –OH (NAC) to –CH₃ (AC) might affect the crosslinking density and therefore the viscosity, wettability, mechanical anchorage, stretchability, and tack force. As a consequence, the higher cross-linking density of AC would lead to a higher viscosity, which can be confirmed by rheological measurements within amplitude and temperature sweeps, **Appendix Fig. A1 and C3**.

Influence of the probe rod geometry and evaluation from the optical observations [101, 102]

As the *RheoTack* method allows for the installation of different rods, the following probe rod geometries were used within the performed *RheoTack* experiments, **Table 7**:

Table 7: Rod geometries used with their dimensions and surface roughness's (grid distance = 5 mm) [102].

Abbreviation	P8	P5	R5
Rod geometry	 Flat cylinder, large $A_{\text{contact}} \cong 50 \text{ mm}^2$	 Flat cylinder, small $A_{\text{contact}} \cong 20 \text{ mm}^2$	 Spherically rounded rod $D_{\text{sphere}} = 12 \text{ mm}$ $A_{\text{contact}} \approx 5 \text{ to } 10 \text{ mm}^2$
Diameter [mm]	8	5	5
Surface roughness Ra [μm]	0.43 ± 0.11	0.75 ± 0.41	0.24 ± 0.03

The rods reveal surface roughness's between 0.24 to 0.43 μm . However, the surface roughness of the three rods allow for comparison between the measurements, because Chiche et al. [132] found that debonding stresses of acrylic PSAs become constant for surface roughness below 0.060 μm . Similar to the probe tack testing, an initial compression force of $F = 0.2 \text{ N}$ for all rods was used for the *RheoTack* measurements, which is achieved when the rod pushes the flexible TTS, adhering to the TMP's bottom, downward, **Fig. 41**. This leads for the different rods to contact pressures of 4 kPa (P8), 10 kPa (P5), and 64 kPa (R5) due to decreasing contact diameters from P8 (8 mm) to P5 (5 mm) and R5 (2 mm).

Moreover, the decreasing contact diameters lead to increasing inclination angles of the TTS in the gap from R5 to P5 and P8. The flexible backing layer of the TTS causes an inhomogeneous stress field within the TTS for all rods. While at the flat rods the stresses increase from zero in the center to the highest value at the circumferential stripe, at the spherical rod the highest stresses occur in the center, which decreases to the outer ring where the TTS coincides with the tangent of the rod sphere. Hence, at the end of the dwell time, the retraction starts from the different tack and adhesion states with varying displacements, depending on the rod and also on the mechanical properties of the TTS (PSA and backing layer), **Fig. 41 and Appendix Table C2**. However, larger displacements during compression result in longer compression times, thus giving the PSA more time for establishing adhesion towards the rods.

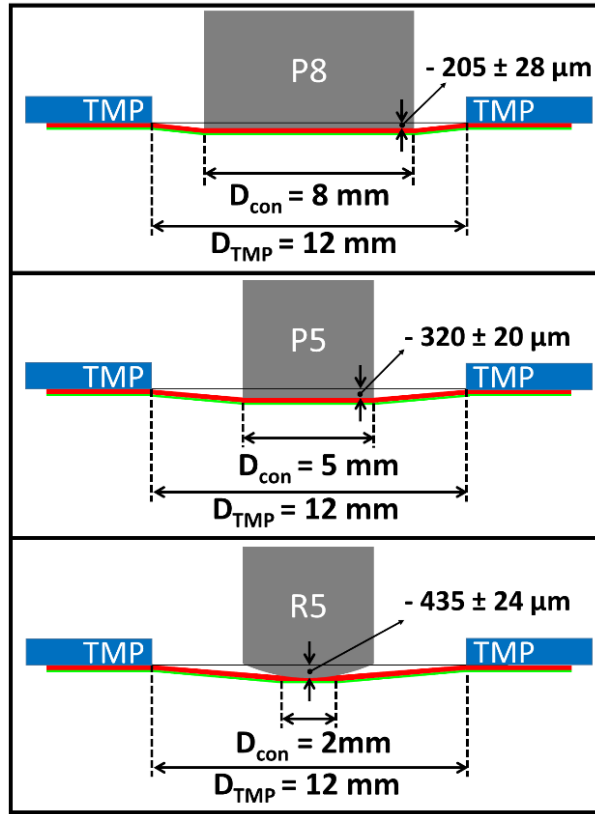


Fig. 41: Starting situation of the rods P8, P5 and R5 with the corresponding displacement and inclination angles at the end of the dwell time for NAC-TTS, $v_F = 49.1 \%$ [102]

The *RheoTack* measurements showed, **Appendix Fig. C1 and C2**, that the chosen rod geometries affect the retraction speed dependent $F-h$ -curves significantly. The shapes of the $F-h$ -curves from the flat rods P8 and P5 are qualitatively similar, while the shape of the $F-h$ -curves from the spherical rod R5 differs significantly due to the different stress fields below the rods. This results in a one-force-maximum for the flat rods, while for R5 a plateau or a second-force-maximum after F_{\max} can be detected. Furthermore, it was found that tack quantities could not be determined for the stiffer TTS at higher retraction speeds. Especially with P8 and P5 the tack cannot be determined on AC- and NAC-TTS with higher v_F , whereas R5 is able to measure the tack for all testing parameters. This is a consequence of the increasing contact pressures from P8 to P5 and R5. Therefore, the tack can be measured with R5 of TTS with the highest v_F and v_{retract} . For TTS with lower v_F , P8 exhibits the highest *RheoTack* quantities due to the largest contact diameter, and therefore the largest adhesion surface (although it applies the lowest contact pressure).

For an independent comparison of the various rods, the data were normalized by using the following normalization factors:

$$n_{P8} = \frac{A_{P5}}{A_{P8}} \quad \text{and} \quad n_{R5} = \frac{A_{P5}}{A_{R5}} \quad (29,30)$$

with the normalization factor for P8 n_{P8} , the contact area of P5 A_{P5} , the contact area of P8 A_{P8} , the normalization factor for R5 n_{R5} , and the contact area of R5 A_{R5} . Results in **Fig. 42** show normalized $F-h$ -curves of AC- and NAC-TTS with $v_F = 49.1 \%$. It is clearly visible that F_{\max} of P8 and P5 are in the same magnitude, whereas F_{\max} of R5 is larger for all v_{retract} . Furthermore,

with R5 the force in the stretching and fibrillation phase increases significantly faster than with the flat rods. The comparison of the stretching and fibrillation phase of P8 and P5 displays that the retraction displacement after the kink point is larger for P8, showing that the fibril creation and elongation occurs over a longer period of time than for P5. This might be an effect of the larger contact and the resulting higher mechanical anchorage between the adhesive and the rod for P8.

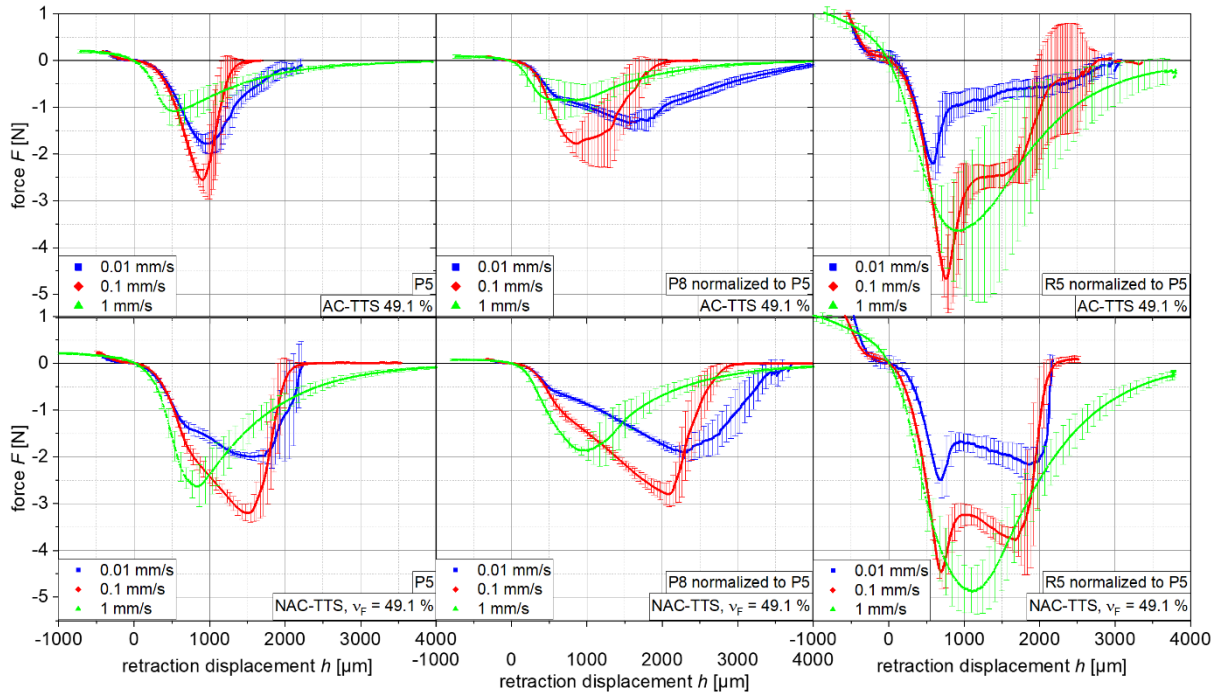


Fig. 42: Normalized F - h -curves (to P5) of P8, P5 and R5 for AC- (top) and NAC-TTS (bottom) with $v_F = 49.1\%$ [102].

During retraction, the inclined TTS in the gap forwards peel stresses to the rods, where the strength of the PSA is exceeded and causing the start of the failure at the contact line that propagates towards the interior of the PSA. Creton and Cicotti [133] stated that failure of a PSA consists of several steps, which start with nano-scaled cavitations. These cavitations dissipate deformation energy by large curvatures and stress concentration factors when the peel stresses of the PSA is exceeded. With further retraction the PSA has two options:

- crack propagation occurs perpendicular to the external load and causes catastrophic cohesive failure, or
- cavitations are lengthened and cause the reduction of local stress concentrations which leads to the start of fibril formation.

As described above, with P8 and P5 both failure options were observed. Especially TTS with higher v_F at the highest v_{retract} display the first option. From the synchronized optical observation at P8 and P5, it can be seen that the fibrils are created at the circumferential stripe of the rods. From here, the fibrils contract into the probe's middle, and cause simultaneous partial debonding that reduces the contact area of about 20 to 30 %, **Fig.43**. A further retraction results in elongation, thinning and strain hardening of the fibrils at the rods circumference, until the first fibrils start to break at F_{max} . Thus, the resin content dependent moduli and retraction speed dependent parameter F_{max} displays a measure for fibril strength, fibril orientation, PSA flowability, stress relaxation, disentangling, and the strain-hardening process [134-136].

Furthermore, for both flat rods the optical observation showed that the retraction causes stretching patterns of the TTS and its withdrawal from the TMP's bottom from the initial edge of TTS $R_{TTS,0}$ to the resulting TTS edge R_{TTS} , displaying that the PSA's shear strength is exceeded, **Fig. 43**.

Contrary to P8 and P5, for R5 only the fibril forming second option can be observed. As the contact area for R5 is in the range of only 2 to 2.5 mm, the transferred forces are relatively little and below the PSAs shear strength. Therefore, no visible stretching patterns and withdrawal of the TTS from the TMPs bottom can be observed, **Fig. 43**. At F_{max} the first fibrils break at the circumference. With ongoing retraction, the inner remaining fibrils are further elongated while the detaching moves in an orderly manner to the center of the rod. This process explains the moderate force decrease for AC-TTS after F_{max} , while for NAC-TTS a second maximum is observed. This can be explained by a higher strain hardening of the fibrils due to the higher interactions of the polymer chains among each other being caused by the polar OH- end-groups.

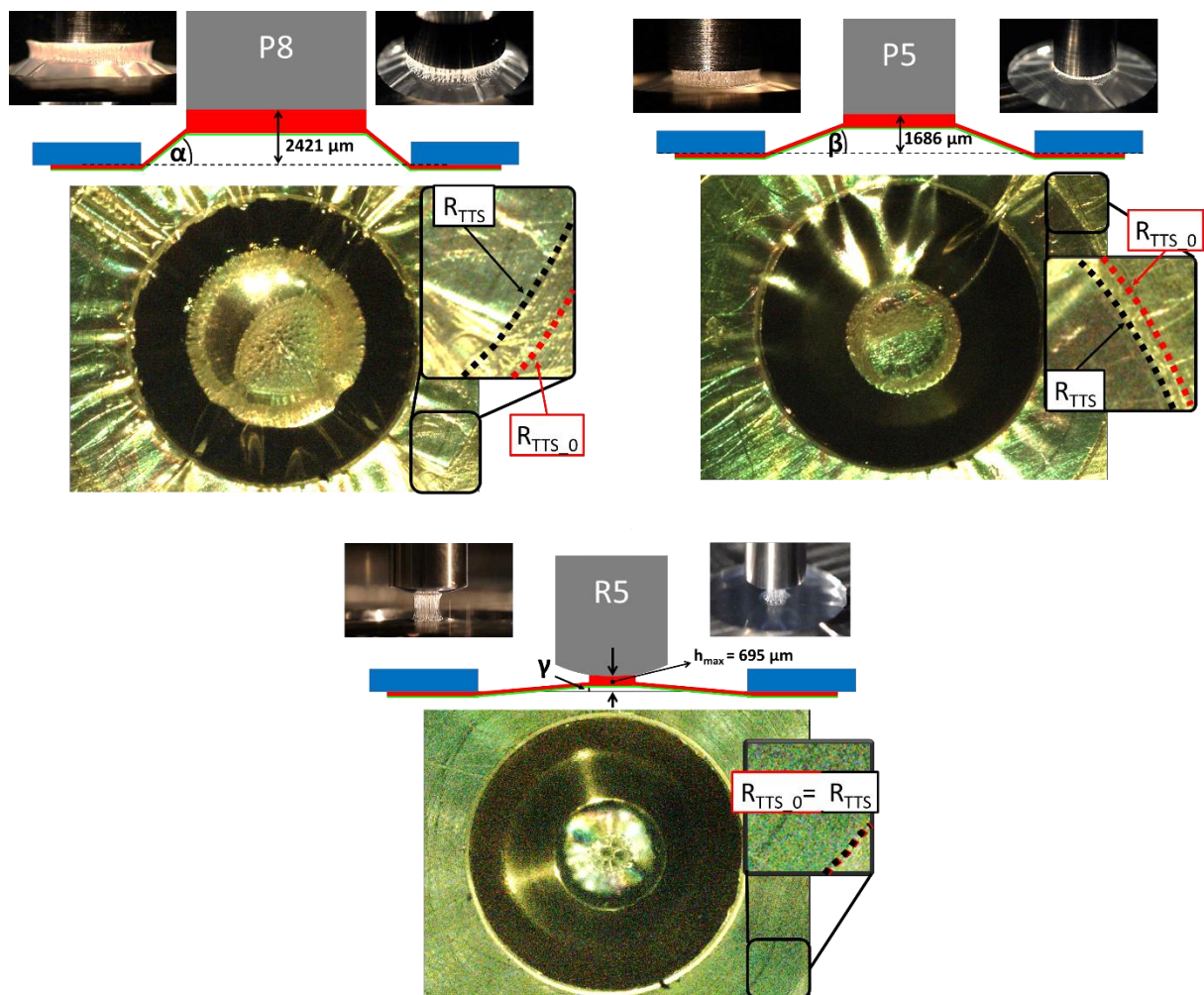


Fig. 43: State of bonding for P8 a), P5 b), and R5 c) at h_{max} (NAC-TTS, $v_F = 49.1\%$ and $v_{retract} = 0.01$ mm/s) with stretching patterns of the backing layer between the TMP and rods, the resulting angles of the TTS between TMP and rods: α for P8, β for P5 and γ for R5, and the TTS's retraction at the TMPs bottom from initial edge of TTS $R_{TTS,0}$ to the resulting edge of TTS R_{TTS} [102].

Additionally, further *RheoTack* evaluation displays the viscoelastic material behavior with increasing $v_{retract}$, which can also be seen by the optical observations, **Fig. 44**. These pictures show a higher $v_{retract}$ leads to a reduced stretchability, shorter fibrils and results also in a higher number of cavities, which decrease in size.

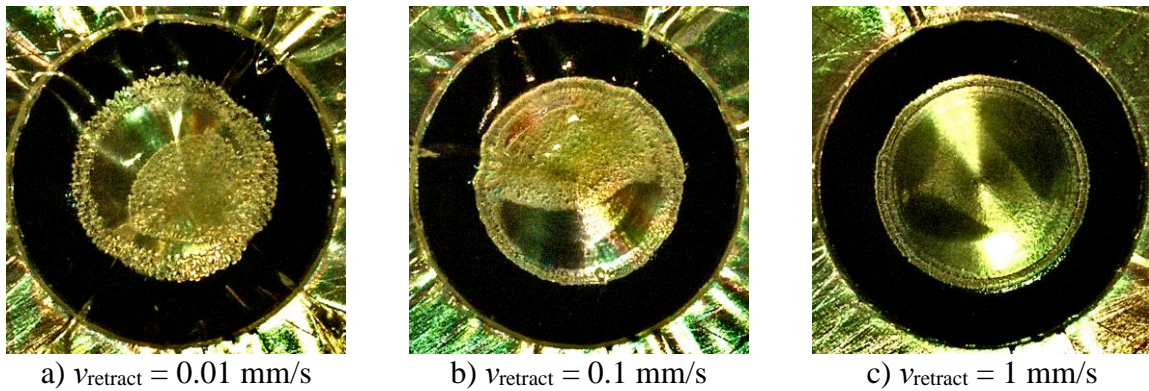


Fig. 44: Deformation structures as the stretching patterns of the TTS and cavity sizes observed with camera 1 under the probe rod in 90° , a) $v_{\text{retract}} = 0.01 \text{ mm/s}$, b) $v_{\text{retract}} = 0.1 \text{ mm/s}$, c) $v_{\text{retract}} = 1 \text{ mm/s}$ [101].

RheoTack with its optical observation presents a powerful testing tool for the tack characterization of TTS and other backing layer supported patches. The resin content, the retraction rate and the rod geometry clearly influence the *RheoTack* results. Thus *RheoTack*, compared to standardized testing procedures, provides more essential information about viscoelastic properties, the adhesion and release behavior of TTS and allows for utilization within TTS development and quality assurance.

5. Conclusion

In this doctoral thesis, pressure sensitive adhesives (PSA) and transdermal therapeutic systems (TTS) were tested with traditional and newly developed application-related methods. This includes the investigation of the PSA within large amplitude oscillatory shear measurements to correlate the materials behavior during the patient's motion. The dielectric measurements show the effect of diffusing water into the PSA and allows for the determination of the diffusion coefficient. The development of the *RheoTack* approach displayed a comprehensive characterization of the TTS's adhesion and release behavior with different rods and various testing parameters.

From the amplitude sweeps and Carreau-Yasuda-like modelling it can be concluded that all PSAs are located close to the gel point and their moduli increase with increasing resin content. Whereas, the storage moduli decrease more than the loss moduli within the nonlinear range, which eases in practice the removal of the TTS, while the viscous properties remain stable for establishing still good adhesion. From the nonlinear interpretation of the Fourier intensity ratio $I_{3/1}$ and the analysis of the Lissajous-Bowditch diagrams, it can be concluded that a consolidation of the gelled network occurs, which is stretched and released by increasing strain amplitudes. The evaluation of the elastic and viscous Lissajous-Bowditch diagrams reveal that an increasing resin content causes an increasing shear thickening and strain stiffening effect, indicating an increasing yielding and stretching of the PSAs microstructure.

The dielectric analysis was used for monitoring the diffusion properties of water and an isotonic NaCl-solution into the PSA, being dependent on the PSA's chemical composition, the resin content correlating with its free volume, and the size of the diffusing molecule. Moreover, the determination of the diffusion coefficient was in accordance with literature values. The contribution of diffusing ions determined by K_2 appears to be negligible, whereas thickness averaging revealed constant values for parameter A and Doolittle constant B being dependent on the resin content and chemical composition of the PSA. The DEA diffusion setup gives a deeper insight into the diffusion mechanisms within the PSA and allows for further investigation of the influence of released sweat and water of the patient.

The developed *RheoTack* approach with its optical observation unit revealed the role of TTS and PSA-composition, and testing conditions on the tack behavior. The PSA type and the resin content affect its flowability, mechanical anchorage and the resulting tack behavior and stretchability. Whereas the variation of the rod's retraction speed represents the PSA's viscoelastic material behavior, the rod geometry (with corresponding different stress fields) influences the detaching behavior. Testing of various TTS with the *RheoTack* approach showed that a low resin content with lower retraction speed causes high tackiness with long and stretched fibrils, while a high resin content and high retraction speed leads to non-adhesion or brittle and catastrophic failure of the TTS.

The thesis presents the newly developed and optimized application-related testing methods for an advanced product-oriented material testing, which allows for a significantly more reliable PSA and TTS characterization that can be utilized within further TTS development.

6. Contribution to Science & practice

Transdermal therapeutic systems (TTS) are modern patch medication systems which allow facilitated treatment of various diseases by improving the patient's compliance e.g. displacing pill intake and reducing gastric load. Although TTS are available on the market since the 80ths, patients still report about poor adhesion properties causing an incorrect medication or even a complete failure of the patch, and thus of the therapy. As TTS development and quality assurance tests are still based on testing methods originating from technical bonding purposes, adhesion and therapeutic improvements are limited.

As TTS consist of a drug containing pressure sensitive adhesive and a protective backing layer subjected to both small and large deformations during application, testing methods have to be improved in terms of considering the patient's motion, the influence of released water and sweat during the application and the evaluation of the TTS's entire adhesion and release behavior. This requires knowledge about pressure sensitive adhesives (PSAs) and their adhesion-molecule-structure-property relationship.

This doctoral thesis is focused on the development of new TTS application-related testing methods and the characterization according to them. A PSA composition dependent study of TTS adhesion and release behavior with correlated small and large amplitude shear investigations were performed. Additionally, the diffusion property analysis of liquid molecules into PSAs was investigated. The following outcomes of this doctoral thesis are considered as the most important contributions to both, science and practice, **Fig. 45**:

- 1) The PSAs large amplitude oscillatory shear testing allows for advanced material characterization within large deformations, which can be used to interpret the PSAs behavior at skin motion during the TTS's application.
- 2) The dielectric analysis of diffusing water and an isotonic NaCl solution within the PSA allows for a comprehensive characterization of the diffusion process and the determination of the diffusion coefficient. Knowledge acquainted with testing method provides a better insight into the diffusion mechanisms within the PSA, and represents an application related testing for further TTS development.
- 3) *RheoTack* approach provides reliable insight into the retraction rate dependent adhesion and release behavior of TTS. The determination of seven *RheoTack* parameters and recorded pictures being correlated with the force-retraction displacement curve during the adhesion and detaching process results in a significantly improved characterization of adhesion when compared to the standardized testing methods. Additionally, this knowledge can be used for the development and production of optimized TTS leading to a reduced therapy failure.

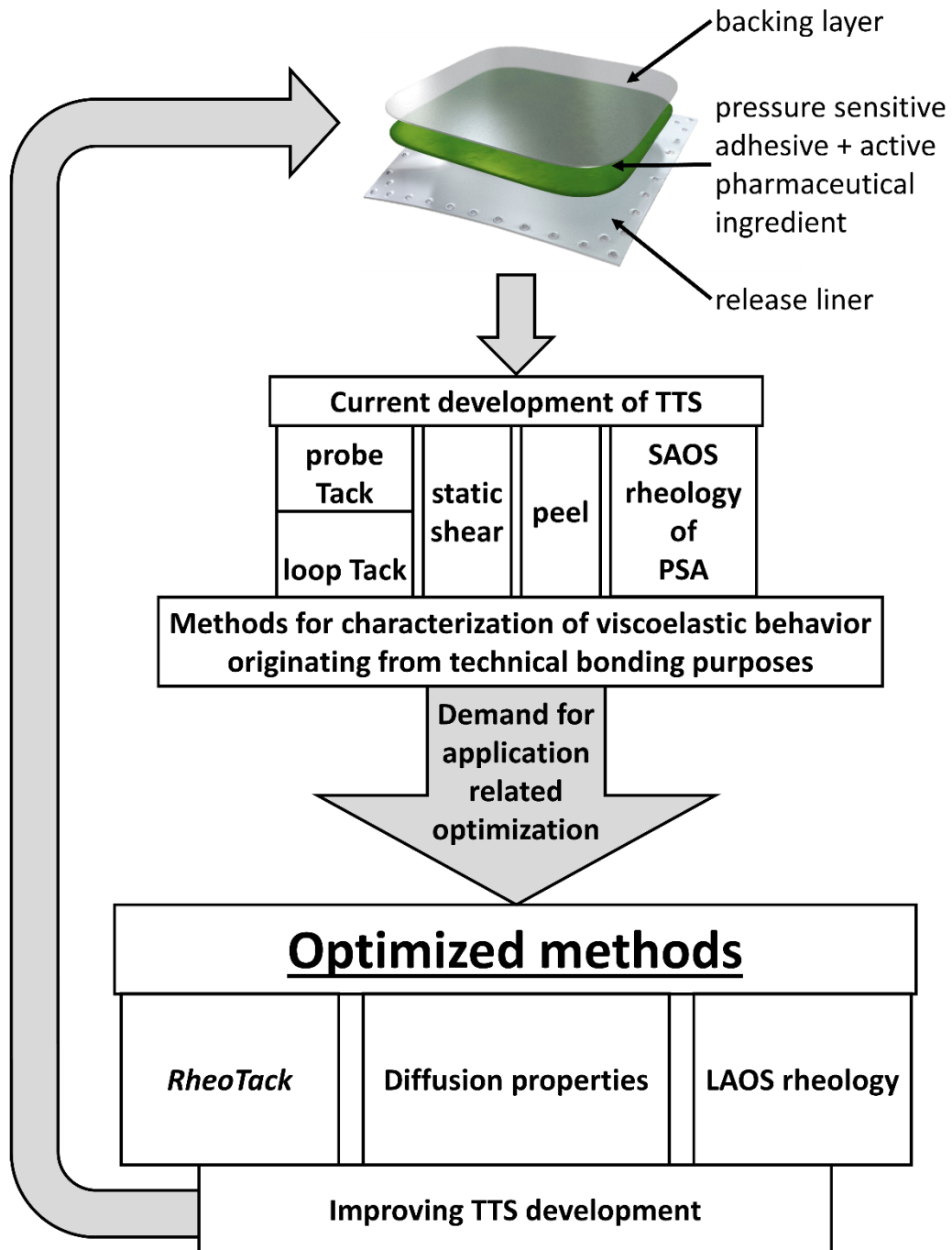


Fig. 45: Flow chart of the contribution to science and practice employed in the PhD. thesis [50].

References

[1]	M. N. Pastore, Y. N. Kalia, M. Horstmann, M.S. Roberts, Transdermal patches: history development and pharmacology, <i>Brit. J. Pharmacol.</i> 172 (2015), 2179-2209.
[2]	U.S. Department of Health and Human Services Food and Drug Administration, Transdermal and Topical Delivery Systems- Product Development and Quality Considerations – Guidance for Industry (2019) https://www.fda.gov last accessed 27 th November 2023.
[3]	European Medicines Agency, Guideline on Quality of Transdermal Patches (2015) https://www.ema.europa.eu , last accessed 27 th November 2023.
[4]	L. Webster, Recent developments in pressure-sensitive adhesives for medical applications, <i>Int. J. Adhes. Adhes.</i> 17 (1997) 69-73.
[5]	Y. W. Chien, Development of Transdermal Drug Delivery Systems, <i>Drug Dev. Ind. Pharm.</i> 13 (1987) 589-651.
[6]	C. H. LaWall, reviewed by E. Kremers, Four Thousand Years of Pharmacy: an Outline, History of Pharmacy and the Allied Sciences, <i>The American Historical Review</i> 33 (1928) 844-845.
[7]	G. A. Bender, R. A. Thom, Great Moments in Medicine and Pharmacy: a History of Medicine and Pharmacy in Pictures, 1966, Northwood Institute Press: Detroit.
[8]	W. F. Morgan, Poisoning by the External Application of Belladonna, <i>Br. Med. J.</i> 2 (1866) 621.
[9]	J. B. Harrison, The Effects of a Belladonna Plaster, <i>Br. Med. J.</i> 1 (1872) 520-521.
[10]	R. T. Johnstone, Occupational Medicine and Industrial Hygiene, 1948, CV Mosby, St. Louis, Mosby.
[11]	G. Martin-Bouyer, M. Toga, R. Lebreton, P. D. Stolley, J. Lockhart, Outbreak of Accidental Hexachlorophene Poisoning in France, <i>Lancet</i> 9 (1982) 91-95.
[12]	U. Wile, J. A. Elliot, Mode of Absorption of Mercury in the inunction Treatment of Syphilis, <i>Journal of the American Medical Association</i> 14 (1917) 1028-1028.
[13]	H. N. Cole, Excretion of Mercury After Intramuscular Injection of Mercuric Bromide, Inunction and Rectal Suppositories, <i>Arch. Dermatol.</i> 14 (1926) 683-692.
[14]	E. W. Brown, W. O. Scott, The Absorption of Methyl Salicylate by the Human Skin, <i>J. Pharmacol. Exp. Ther.</i> 50 (1934) 32-50.
[15]	C. R. Moore, J. K. Lamar, N. Beck, Cutaneous Absorption of Sex Hormones, <i>JAMA</i> 111 (1938) 11-14.
[16]	B. Zondek, B. Shapiro, S. Hestrin, Application of the Millon Reaction to the Determination of Chlorophenols in Body Fluids and Tissues, <i>Biochem. J.</i> 37 (1943) 589-591.
[17]	J. A. Davis, B. H. Wiesel, The Treatment of Angina Pectoris with a Nitroglycerin Ointment, <i>Am. J. Med. Sci.</i> 230 (1955) 259-263.
[18]	D. E. Wurster, S. F. Kramer, Investigation of some Factors Influencing Percutaneous Absorption, <i>J. Pharm. Sci.</i> 50 (1961) 288-293.
[19]	A. Zaffaroni, A. Calif, Bandage for Controlled Release of Vasodilators, US3,742,951, 3 rd July 1973.
[20]	A. Zaffaroni, A. Calif, Drug-Delivery System, US3,854,480, 17 th December 1974.
[21]	A. D. Keith, M. Fla, W. Snipes, Polymeric Diffusion Matrix Containing a Vasodilator, US4,291,015, 22 nd September 1981.
[22]	D. R. Sanvordeker, E. Grove, J. G. Cooney, D. Plaines, R. C. Wester, Transdermal Nitroglycerin Pad, US4,336,243, 22 nd June 1982.
[23]	D. A. Sica, R. Grubbs, Transdermal Clonidine: Therapeutic Considerations, <i>J. Clin. Hypertens</i> 7 (2005) 558-562.

[24]	R. M. Gale, R. G. Berggren, Transdermal Delivery System for Delivering Nitroglycerin at High Transdermal Fluxes, US4,615,699, 7 th October 1986.
[25]	R. M. Gale, V. Goetz, E. S. Lee, L. T. Taskovich, S. I. Yum, Transdermal Administration of Fentanyl and Device Therefor, US4,588,580, 13 th May 1986.
[26]	R. W. Baker, F. Kochinke, C. Huang, Novel Transdermal Nicotine Patch, US4,839,174, 13 th June 1989.
[27]	C. D. Ebert, D. Patel, W. Heiber, Method and Device for Transdermally Administering Testosterone Across Nonscrotal Skin at Therapeutically Effective Levels, US5,152,997, 6 th October 1992.
[28]	A. W. Meikle, N. A. Mazer, J. F. Moellmer, J. D. Stringham, K. G. Tolman, S. W. Sanders, W. D. Odell, Enhanced Transdermal Delivery of Testosterone Across Nonscrotal Skin Produces Physiological Concentrations of Testosterone and its Metabolites in Hypogonadal men, <i>J. Clin. Endocrinol. Metab.</i> 74 (1992) 623-628.
[29]	M.R. Prausnitz, S. Mitragotri, R. Langer, Current Status and Future Potential of Transdermal Drug Delivery, <i>Nat. Rev. Drug Discov.</i> 3 (2004) 115-124.
[30]	https://www.thepharmajournal.com , Recent Trends in Challenges and Opportunities in Transdermal Drug Delivery System, last accessed 27 th November 2023.
[31]	W. Y. Joeng, M. Kwon, H. E. Choi, K. S. Kim, Recent Advances in Transdermal Drug Delivery Systems: A Review, <i>Biomaterials Research</i> 25 (2021) 24.
[32]	M. Azmana, S. Mahmood, A. R. Hilles, U. K. Mandal, K. A. S. Al-Japairai, S. Raman, Transdermal Drug Delivery System Through Polymeric Microneedle: A Recent Update, <i>J. Drug. Deliv. Sci. Tec.</i> 60 (2020) 101877.
[33]	P. Minghetti, F. Cilurzo, A. Casiraghi, Measuring Adhesive Performance in Transdermal Delivery Systems, <i>Am. J. Drug Deliv.</i> 2 (2004) 193-206.
[34]	G.K. Schalaus II, A. Bobenrieth, R. O. Huber, L. S. Nartker, X. Thomas, Silicone Adhesives in Medical Applications, in: Applied Adhesive bonding on Science and Technology, 2018, Intech Open, London, DOI: 10.5772/intechopen.71817 .
[35]	I. Benedek, M. M. Feldstein, Silicone Pressure-Sensitive Adhesives, in: Technology of Pressure-Sensitive Adhesives and Products, 2009, CRC Press Taylor&Francis Group, Boca Raton, ISBN: 978-1-4200-5939-7.
[36]	L. Mestach, S. Huygens, A. Goossens, L. Gilissen, Allergic Contact Dermatitis caused by Acrylic-bases Medical Dressings and Adhesives, <i>Contact Dermatitis</i> 79 (2018) 81-84.
[37]	A. Kunst, Thermodynamic Activity in PSA Matrices: Determination and influence on Skin Permeation, <i>Dissertation</i> , 2015, Friedrich-Alexander-Universität Erlangen-Nürnberg.
[38]	D. Satas, Handbook of Pressure Sensitive Adhesive Technology, Springer Science & Business Media, New York, ISBN: 978-1-4757-0868-4.
[39]	https://www.dupont.com , Review of silicone adhesives in healthcare applications, last accessed 27 th November 2023.
[40]	K. R. Chadhuri, Crystallisation within transdermal rotigotine patch: is there cause for concern?, <i>Expert Opin. Drug. Del.</i> 5 (2008) 1169-1171.
[41]	V. V. Ranade, Drug Delivery Systems. 6. Transdermal Drug Delivery, <i>J. Clin. Pharmacol.</i> 31 (1991) 401-418.
[42]	G. Passoni, P. Casetta, P. Stefanelli, Adhesive Transdermal Formulations of Diclofenac Sodium, CA2 471 798, 10 th July 2003.
[43]	S. K. Govil, E. M. Rudnic, D. G. Sterner, Transdermal itroglycerine Patch with Penetration Enhancers, US5,262,165, 16 th November 1993.
[44]	C. A. Scarbrough, S. S. Scarbrough, J. Shubrook, Transdermal Delivery of Metformin, US2012/0283332A1, 8 th November 2012.

[45]	K. Sharma, S. D. Roy, E. J. Roos, Transdermal administration of buprenorphine, US5,069,909, 3 rd December 1991.
[46]	J. Zeltman, Transdermal Patch and Method for Delivery of Vitamin B12, EP 2 124 907 B1, 30 th May 2018.
[47]	A. Wypych, Handbook of Plasticizers, 2017, ChemTec Publishing, Toronto, ISBN 978-1-895198-97-3.
[48]	D. Douroumis, Hot-melt Extrusion: Pharmaceutical Applications, 2012, John Wiley & Sons Ltd., Chichester, ISBN 9780470711187.
[49]	T. Takayasu, I. Kakubari, N. Shikai, J. Kawakami, N. Nakajima, A. Uruno, Patch, US6,211,425 B1, 3 rd April 2001.
[50]	https://www.itslohmann.com , last accessed 27 th November 2023.
[51]	International Council on Harmonisation of Technical Requirements for Registration of Pharmaceuticals for Human Use, Pharmaceutical Development Q8(R2) (2009) https://www.ema.europa.eu , last accessed 27 th November 2023.
[52]	International Council on Harmonisation of Technical Requirements for Registration of Pharmaceuticals for Human Use, Validation of Analytical Procedures: Text and Methodology Q2(R1) (2005) https://www.ema.europa.eu , last accessed 27 th November 2023.
[53]	D. M. Herlach T. Palberg, I. Klassen, S. Klein, R. Kobold, Overview: Experimental studies of crystal nucleation: Metals and colloids, <i>J. Chem. Phys.</i> 145 (2016) 211701.
[54]	I. Rezaeian. P. Zahedi, A. Rezaeian, Rubber Adhesion to Different Substrates and Its Importance in Industrial Applications: A Review, <i>J. Adhes. Sci. Technol.</i> 26 (2012) 721-744.
[55]	T. H. Kim, Bonding in: The International Academy for Production Engineering, CIRP Encyclopedia of Production Engineering, 2014, Springer, Berlin, Heidelberg, ISBN 978-3-642-20618-4.
[56]	L. F. M. da Silva, A. Öchsner, R. D. Adams, Handbook of Adhesion Technology, 2011, Springer, Berlin, ISBN: 978-3-319-55410-5.
[57]	P. W. Atkins, J. de Paula, J. Keeler, Physical Chemistry, 2018, Oxford University Press, New York, ISBN: 9780198769866.
[58]	B. Erman, J. E. Mark, C. M. Roland, The Science and Technology of Rubber, 2013, Elsevier, Waltham, ISBN: 978-0-12-394584-6.
[59]	A. N. Gent, S. M. Lai, Adhesion and Autohesion of Rubber Compounds: Effect of Surface Roughness, <i>Rubber Chem. Technol.</i> 68 (1995) 13-25.
[60]	American Society for Testing and Materials (ASTM), Standard Test Method for Pressure-Sensitive Tack of Adhesive Using an Inverted Probe Machine – ASTM D 2979 Vol. 15-10, 2016, ASTM International West Conshohocken.
[61]	CEN European Committee for Standardization, Adhesives for paper and board, packaging and disposable sanitary products – Tack measurement for pressure sensitive adhesives – Determination of loop tack – DIN EN 1719:1998, 1998, Beuth Verlag GmbH, Berlin.
[62]	P. Tordjeman, E- Papon, J-J. Villenave, Tack Properties of Pressure-Sensitive Adhesives, <i>J. Polym. Sci. Pol. Phys.</i> 68 (1995) 13-25.
[63]	CEN European Committee for Standardization, Self-adhesive tapes - Determination of peel adhesion properties ISO 29862:2018, 2019, Beuth Verlag GmbH, Berlin.
[64]	https://www.instron.com/de , Seal Strength and Peel Testing of Packaging, last accessed 27 th November 2023.
[65]	CEN European Committee for Standardization, Self-adhesive tapes - Measurement of static shear adhesion ISO 29863:2018, 2019, Beuth Verlag GmbH, Berlin.

[66]	http://www.tainstruments.com , Pressure-Sensitive Adhesive Tack Using the ARES Rheometer, last accessed 27 th November 2023.
[67]	https://cdn.technologynetworks.com , Assessing tackiness and adhesion using a pull away test on a rotational rheometer, last accessed 27 th November 2023.
[68]	www.netzsch.com , Application note: Determination of Pressure-Sensitive Tack and Adhesion Using Axial Measurements on a Rotational Rheometer – Blu-Tack [®] , last accessed 27 th November 2023.
[69]	http://www.tainstruments.com , Rheological Analysis of Tack, last accessed 27 th November 2023.
[70]	German Institute for Standardization e.V., Rheometry- Measurement of rheological properties using rotational rheometers - Part 4: Oscillatory rheology – DIN 53019-4, 2016, Beuth Verlag GmbH, Berlin.
[71]	L. H. Sperling, Introduction to physical polymer science, 4th edition, 2006, Wiley, New Jersey, ISBN: 13 978-0-471-70606-9.
[72]	M. Michaelis, Characterization of Pressure Sensitive Adhesive Systems for Transdermal Patches, <i>Dissertation</i> , 2015, Universität Hamburg.
[73]	M. Kempf, D. Ahirwal, M. Cziep, M. Wilhelm, Synthesis and Linear and Nonlinear Melt Rheology of well-defined Comb Architectures of PS and PpMS with a low and Controlled Degree of long-chain Branching, <i>Macromolecules</i> , 46 (2013) 4978–4994.
[74]	D. Van Duschotten, M. Wilhelm, Increased torque transducer sensitivity via oversampling, <i>Rheol. Acta</i> 40 (2001) 395–399.
[75]	I. Natalia, R. H. Ewoldt, E. Koos, Questioning a fundamental assumption of rheology: observation of noninteger power expansions, <i>J. Rheol.</i> 64 (2020) 625–635.
[76]	K. Hyun, E. S. Baik, K. H. Ahn, S.J. Lee, M. Sugimoto, K. Koyama, Fourier-transform rheology under medium amplitude oscillatory shear for linear and branched polymer melts, <i>J. Rheol.</i> 51 (2007) 1319-1342.
[77]	R. Kádár, M. Abbasi, R. Figuli, M. Rigdahl, M. Wilhelm, Linear and nonlinear rheology combined with dielectric spectroscopy of hybrid polymer nanocomposites for semiconductive applications, <i>Nanomaterials</i> 7(2017) 23.
[78]	R. Kádár, K. Gaska, T. Gkourmpis, Nonlinear “oddities” at the percolation of 3D hierarchical graphene polymer nanocomposites, <i>Rheol. Acta</i> 59 (2020) 333–347.
[79]	A. Fick, Ueber Diffusion, <i>Ann. Phys.</i> 170 (1855) 59 .
[80]	J. Crank, The Mathematics of Diffusion, 1975, Oxford University Press, New York, ISBN 0 19 853344 6.
[81]	W. R. Vieth, Diffusion In and Trough Polymers, 1979, Oxford University Press, New York, ISBN 3-446-15574-0.
[82]	S. Wittchen, H. Kahl, D. Waltschew, I. Shahzad, M. Beiner, V. Cepus, Diffusion Coefficients of Polyurethane Coatings by Swelling Experiments using Dielectric Spectroscopy, <i>J. Appl. Polym. Sci.</i> 137 (2020) 49174.
[83]	J. E. Companik, S. A. Bidstrup, The Viscosity and Ion Conductivity of Polydimethylsiloxane systems: 1. Chain length and Ion size Effects, <i>Polymer</i> 35 (1994) 22.
[84]	G. T. Fieldson, T. A. Barbari, The use of FTi.r.-a.t.r. Spectroscopy to Characterize Penetrant Diffusion in Polymers, <i>Polymer</i> 34 (1993) 6.
[85]	A. McIlhagger, D. Brown, B. Hill, The development of a dielectric system for the on-line cure monitoring of the resin transfer moulding process, <i>Compos. Part A Appl. Sci. Manuf.</i> 31 (2000) 1373–1381.

[86]	J. Steinhaus, M. Frentzen, M. Rosentritt, B. Moeginger, Dielectric analysis of short-term and long-term curing of novel photo-curing dental filling materials, <i>Macromol. Symp.</i> 296 (2010) 622-625.
[87]	J. Steinhaus, B. Moeginger, M. Grossgarten, B. Hausnerova, Evaluation of dielectric curing monitoring investigating light-curing dental filling composites, <i>Mater. Eng.</i> 18 (2011) 28-33.
[88]	F. Starzyk, Parametrisation of Interdigit Comb Capacitor for Dielectric Impedance Spectroscopy, <i>Archiv. Mat. Sci. Eng.</i> 34 (2008) 31-34.
[89]	K. Zahouily, C. Decker, E. Kaisersberger, M. Gruener, Real-time UV cure monitoring, <i>Eur. Coating J.</i> 11 (2003) 245-249.
[90]	R. A. Pethrick, D. Hayward, Real time dielectric relaxation studies of dynamic polymeric systems, <i>Prog. Polym. Sci.</i> 27 (2002) 1983-2017.
[91]	M. G. Penon, S. J. Picken, M. Wübbenhorst, J. van Turnhout, Vapor Diffusion in Porous/Nonporous Polymer Coatings by Dielectric Sorption Analysis, <i>J. Appl. Polym. Sci.</i> 105 (2007) 1471-1479.
[92]	B. Gong, Y. Tu, Y. Zhou, R. Li, F. Zhang, Z. Xu, D. Liang, Moisture Absorption Characteristics of Silicone Rubber and Its Effect on Dielectric Properties, <i>Annual Report Conference on Electrical Insulation and Dielectric Phenomena</i> (2013) 430-433.
[93]	L. Ollivier-Lamarque, M. Lallart, N. Mary, T. Uchimoto, S. Livi, S. Marcelin, H. Miki, Dielectric Analysis of Water Uptake in Polymer Coating using Spatially Defined Fick's Law and Mixing Rule, <i>Prog. Org. Coat.</i> 148 (2020) 105846.
[94]	https://dupont.com , Liveo™ BIO-PSA 7-4201 silicone adhesives, last accessed 27 th November 2023.
[95]	https://dupont.com , Liveo™ BIO-PSA 7-4301 silicone adhesives, last accessed 27 th November 2023.
[96]	https://dupont.com , Liveo™ BIO-PSA 7-4501 silicone adhesives, last accessed 27 th November 2023.
[97]	https://dupont.com , Liveo™ BIO-PSA 7-4601 silicone adhesives, last accessed 27 th November 2023.
[98]	https://www.3m.com , 3M™ Scotchpak™ Polyester Backing Film Laminate, 9732, last accessed 20 th November 2023.
[99]	M. Meurer, R. Kádár, E. Ramakers-van Dorp, B. Möginger, B. Hausnerová, Nonlinear oscillatory shear tests of pressure-sensitive adhesives (PSAs) designed for transdermal therapeutic systems (TTS). <i>Rheol. Acta</i> , 60 (2021) 553–570.
[100]	M. Meurer, L. Retterath, E. Ramakers-van Dorp, B. Möginger, B. Hausnerová, Effects of resin content on water diffusion in two chemically different silicone based pressure sensitive adhesives (PSA) using dielectric analysis (DEA). Submitted to <i>APL Bioeng</i> , December 2023.
[101]	M. Meurer, T. Prescher, E. Ramakers-van Dorp, B. Möginger, B. Hausnerová, RheoTack—An approach to investigate retraction rate dependent detaching behavior of pressure sensitive adhesives. <i>J. Rheol.</i> 66 (2022) 505-514.
[102]	M. Meurer, G. Kamsu, C. Dresbach, E. Ramakers-van Dorp, B. Möginger, B. Hausnerová, Rate dependent tack behavior of silicone-based pressure sensitive adhesives for transdermal therapeutic systems. Submitted to <i>J. Ind. Eng. Chem.</i> November 2023
[103]	A.M. Wessendorf, D.J. Newman, Dynamic understanding of human skin movement and strain-field analysis. <i>IEEE Trans. Bio-Med. Eng.</i> 59 (2012) 3432–3438.

[104]	R. Maiti, L.C. Gerhardt, Z.S. Lee, R.A. Byers, D. Woods, J.A. Sanz-Herrera, S.E. Franklin, R. Lewis, S.J. Mather, M.J. Carré, In vivo measurement of skin surface strain and sub-surface layer deformation induced by natural tissue stretching. <i>J. Mech. Behav. Biomed.</i> 62 (2016) 556–569.
[105]	W. Ge, A. Sfara, B. Hians, Skin deformation during shoulder movements and upper extremity activities. <i>Clin. Biomech.</i> 47 (2017)1–6.
[106]	H.G. Sim, K.H. Ahn, S.J. Lee, Large amplitude oscillatory shear behavior of complex fluids investigated by a network model: a guideline for classification. <i>J. Non-Newton. Fluid.</i> 112 (2003) 237–250.
[107]	F.J. Stadler, D. Auhl, H. Münstedt, Influence of the molecular structure of polyolefins on the damping function in shear. <i>Macromolecules.</i> 41 (2008) 3720–3726.
[108]	E.P. Chang, Viscoelastic properties of pressure-sensitive adhesives. <i>J. Adhesion.</i> 60 (1997) 233–248.
[109]	C.A. Dahlquist, Pressure sensitive adhesives. In: Patrick RL (ed) Treatise on adhesion and adhesive, vol 2, 1969, Marcel Dekker, New York, pp 219–260
[110]	M.A. Cziep, M. Abbasi, M. Heck, L. Arens, M. Wilhelm, Effect of molecular weight, polydispersity, and monomer of linear homopolymer melts on the intrinsic mechanical nonlinearity $3Q_0(\omega)$ in MAOS. <i>Macromolecules</i> 49 (2016) 3566–3579.
[111]	L. Du, M. Namvari, F. Stadler, Large amplitude oscillatory shear behavior of graphene derivative/poly-dimethylsiloxane nanocomposites. <i>Rheol. Acta</i> 57 (2018) 429–443.
[112]	M. Kamkar, E. Aliabadian, A.S. Zeraati, U. Sundaraj, Application of nonlinear rheology to assess the effect of secondary nanofiller on network structure of hybrid polymer nanocomposites. <i>Phys. Fluids</i> 30 (2018) 023102.
[113]	M. Kamkar, Large amplitude oscillatory shear flow: microstructural assessment of polymer nanocomposites, hydrogels, and interfaces. Dissertation, 2020, University of Calgary.
[114]	K. Gaska, R. Kádár, Evidence of percolated network at the linear - nonlinear transition in oscillatory shear. <i>AIP Conf. Proc.</i> 2107 (2019) 050003.
[115]	T.B. Goudoulas, N. Germann, Concentration effect on the nonlinear measures of dense polyethylene oxide solutions under large amplitude oscillatory shear. <i>J. Rheol.</i> 62 (2018) 1299–1317.
[116]	E. Aliabadian, S. Sadeghi, M. Kamkar, Z. Chen, U. Sundararaj, Rheology of fumed silica nanoparticles/partially hydrolyzed polyacrylamide aqueous solutions under small and large amplitude oscillatory shear deformations. <i>J. Rheol.</i> 62 (2018)1197–1216.
[117]	S. Khandavalli, J.P. Rothstein, Large amplitude oscillatory shear of three different shear-thickening particle dispersions. <i>Rheol. Acta</i> 54 (2015) 601–618.
[118]	Z. Wang, D.Z. Jia, H.M. Fang, C.Z. Guan, Absorption and Permeation of Water and Aqueous Solutions of High-temperature Vulcanized Silicone Rubber. <i>IEEE T. Dielect. El. In.</i> 22 (2015) 6.
[119]	K. Asaoka, S. Hirano, Diffusion coefficient of water through dental composite resin. <i>Biomaterials.</i> 24 (2003) 975-979.
[120]	K. Zahouily, C. Decker, E. Kaisersberger, M. Gruener, Real-time UV cure monitoring. <i>Eur Coating J</i> ,11 (2003) 245-9.
[121]	G.T. Fieldson, T.A. Barbari, The use of FTi.r.-a.t.r.spectroscopy to characterize penetrant diffusion in polymers. <i>Polymer.</i> 34 (1993) 1146-1153.
[122]	H. Lee, The Handbook of Dielectric Analysis and Cure Monitoring. Vol 156, 2017, Lambert Technol LLC, Boston, MA.

[123]	B. V. Zeghbroek, Principles of Semiconductor Devices. Prentice Hall, New Jersey, 2002.
[124]	A. K. Doolittle, Studies in Newtonian Flow II. The Dependence of the Viscosity of Liquids on Free-Space. <i>J. Appl. Phys.</i> 22 (1951) 1471-1475.
[125]	F.J. Millero, G.K. Ward, K.F. Lepple, E.V. Hoff, Isothermal compressibility of aqueous sodium chloride, magnesium chloride, sodium sulfate, and magnesium sulfate solutions from 0 to 45.deg. at 1 atm. <i>J. Phys. Chem.</i> 78 (1974) 1636-1643.
[126]	Y. Marcus, Electrostriction, Ion Solvation, and Solvent Release on Ion Pairing. <i>J. Phys. Chem. B.</i> 109 (2005) 18541-18549.
[127]	J.C. Hindman, Nuclear Magnetic Resonance Effects in Aqueous Solutions of 1–1 Electrolytes. <i>J. Chem. Phys.</i> 36 (1962) 1000-1016.
[128]	R. W. Impey, P.A. Madden, I.R. McDonald, Hydration and Mobility of Ions in Solution. <i>J. Phys. Chem.-US.</i> 87 (1983) 25.
[129]	R. Heyrovská, Ionic Concentrations and Hydration Numbers of “Supporting Electrolytes”, <i>Electroanal.</i> 18 (2006) 351-361.
[130]	Z. Wang, Z.D. Jia, M.H. Fang, Z.C. Guan, Absorption and Permeation of Water and Aqueous Solutions of High-temperature Vulcanized Silicone Rubber. <i>IEEE T Dielect. El. In.</i> 22 (2015) 6.
[131]	J. Zhang, J. Cui, F. Wang, J. Xiang, Z. Cao, Q. Wang, Diffusion in Aqueous Solutions with Multivalent Cations and Especially in Cationic First Hydration Shell. <i>J. Phys. Chem. B.</i> , 126 (2022) 3585-3592.
[132]	A. Chiche, P. Pareige, C. Creton, Role of surface roughness in controlling the adhesion of a soft adhesive on a hard surface. <i>C. R. Acad- Sci. Paris.</i> 1 (2000) 1197-1204.
[133]	C. Creton, M. Cicotti, Fracture and adhesion of soft materials. <i>Rep. Prog. Phys.</i> 79 (2016) 046601.
[134]	K. Takahashi, O. Ryuto, K. Inaba, K. Kishimoto, Scaling effect on the detachment of pressure-sensitive adhesives through fibrillation characterized by a probe-tack test. <i>Soft Matter.</i> 16 (2020) 6493-6500.
[135]	M.A. Droesbeke, A. Simula, J.M. Asua, F.E. Du Prez, Biosourced terpenoids for the development of sustainable acrylic pressure-sensitive adhesives via emulsion polymerization. <i>Green Chem.</i> 22 (2020) 4561.
[136]	K. Takahashi, M. Shimizu, K. Inaba, K. Kishimoto, Y. Inao, T. Sugizaki, Tack performance of pressure-sensitive adhesive tapes under tensile loading. <i>Int. J. Adhes. Adhes.</i> 45 (2013) 90-97.

List of Figures

Fig. 1	Design of transdermal therapeutic systems (TTS) – a) drug-in-adhesive matrix type and b) drug reservoir type [2].
Fig. 2	General molecular structure of a methacrylic ester (monomer) with $R = CH_3$ and $R' =$ alkyl group (according to [35]).
Fig. 3	Polymerization of polyisobutylene (PIB) as a) homopolymer from isobutylene (IB), b) copolymer from IB and isoprene (IP) [35].
Fig. 4	Chemical structures of the non-amine compatible (NAC) and amine-compatible (AC) PSA and the steps of their synthesis (according to [39]).
Fig. 5	Scheme of TTS manufacturing with a coating head, drying zone and laminating zone (according to [50]).
Fig. 6	Schematic representation of models describing adhesive effects: a) adsorption contribution; b) mechanical anchoring; c) diffusive contribution; d) electrostatic contribution; e) chemical bonding.
Fig. 7	Scheme of a) probe tack test according to ASTM D2979 [60] and b) loop tack test according to DIN EN 1719 [61].
Fig. 8	Force-time curve of an instrumented tack test with a compressive force during loading and a tensile force during detaching [62].
Fig. 9	Scheme of the peel adhesion tests with peel angle 180° a) on a stainless steel plate and with peel angle 90° b) with a horizontally moveable stainless steel plate.
Fig. 10	Evaluation of an instrumented peel adhesion test (according to [64]).
Fig. 11	Scheme of a static shear testing device with a 2° twisted stainless steel plate and a 1000 g weight.
Fig. 12	Geometries of rotational rheometers: plate-plate, cone-plate (with the cone angle α) and Couette/Searle arrangement; the gap, where the sample is strained, indicated in blue.
Fig. 13	Scheme of the oscillatory shear measurement a) sample is loaded in an oscillatory manner between two plates, b) sinusoidal excitation (γ), response signal (τ) and phase angle(δ).
Fig. 14	G' and G'' being independent from strain amplitude γ_0 in the LVE or SAOS region and dependent from the strain amplitude γ_0 in the middle and large amplitude oscillatory shear region (MAOS, LAOS).
Fig. 15	Frequency dependent storage G' and loss modulus G'' of a PSA at $T = 30^\circ\text{C}$.
Fig. 16	Frequency dependent G' and G'' of a PSA and its correlation to bonding and debonding [72].
Fig. 17	Strain amplitude dependent moduli G' and G'' as well as $I_{3/1}$ – nonlinear behavior starts above strain amplitudes of 1%.
Fig. 18	Normalized elastic a) and viscous b) Lissajous-Bowditch diagrams for linear viscoelastic behavior (light grey) and nonlinear behavior (green) with determination of zero-strain modulus G'_M , maximum strain modulus G'_L , zero-rate dynamic viscosity η'_M , and maximum-rate dynamic viscosity η'_L .
Fig. 19	Sorption curves of a polymer sheet showing different percentages of sorption uptake [80].
Fig. 20	Measuring principle of the dielectric analysis (DEA) with moving ions and orienting dipoles forced by the applied alternating external electric field.
Fig. 21	Design of an IDEX sensor with intermeshing electrodes and resulting alternating electric field a). Microscopic picture of IDEX sensor with an electrode width $w \approx 100 \mu\text{m}$ and a distance between electrodes $b \approx 130 \mu\text{m}$ b).
Fig. 22	Effect of temperature on the ion viscosity during desorption [82].

Fig. 23	Desorption curve of polyurethane with different hardener quantities [82].
Fig. 24	Effect of variation of hardener amount on diffusion coefficients of two resin compositions [82].
Fig. 25	Strain amplitude dependent storage G' and loss moduli G'' of AC- and NAC-PSAs for $\omega = 1$ rad/s; symbols = measured data; lines = Carreau-Yasuda-like fits [99].
Fig. 26	Representation according to Chang and Dahlquist of SAOS data from AC- and NAC-PSAs [99].
Fig. 27	Strain amplitude dependent nonlinear parameter $I_{3/1}$ (γ_0) for AC- and NAC-PSAs [99].
Fig. 28	Strain amplitude and frequency dependent strain stiffening ratios S for AC- and NAC-PSAs [99].
Fig. 29	Strain amplitude and frequency dependent shear thickening ratios T for AC- and NAC-PSAs [99].
Fig. 30	Cross sectional sketch of the experimental setup with a temperature controlled metal block, sealing, the dielectric analysis mini IDEX-sensor, the fringe field of the DEA sensor, the PSA-film and the applied diffusant on the PSA-film a), stacked PSA-films are positioned on the mini-IDEX sensor, enclosed by the sealant b), water-temperature controlled aluminum-block with PTFE-covering plate, added onto the mini-IDEX sensor setup [100].
Fig. 31	Increasing water concentration in a PSA, depending on time and space [100].
Fig. 32	Time dependent η^{ion} -time curve from the DEA to monitor the process of diffusing water into a silicone PSA, with characteristic evaluated points [100].
Fig. 33	Ion viscosity (η^{ion}) as a function of time (t) for various film thickness of a) amine compatible (AC) and b) non-amine compatible (NAC) PSA-films (resin content of $v_F = 51.6$ %) [100].
Fig. 34	Influence of the resin content and the PSA-film thickness of amine compatible (AC) a) and non-amine compatible (NAC) PSA-films b) [100].
Fig. 35	Influence of the diffusant and the PSA-film thickness of amine compatible (AC) a) and non-amine compatible (NAC) PSA-films b) [100].
Fig. 36	Resin content dependent results from probe tack a) and peel adhesion strength testing for AC- and NAC-TTS.
Fig. 37	Sketch of the <i>RheoTack</i> approach with the upper plate as the probe rod, the temperature module plate (TMP) for patch fixation as the lower plate, and the implemented optical observation unit for synchronized video monitoring from the bottom (90° , camera 1), lateral (0° , camera 2), and top (45° , camera 3) to the rheometer [101].
Fig. 38	Evaluation of F - h curve from <i>RheoTack</i> testing with deformation phases and characteristic <i>RheoTack</i> quantities: S , $F_{\text{start fib}}$, $h_{\text{start fib}}$, $E_{\text{start fib}}$, F_{max} , h_{max} , E_{adh} and corresponding structures at $F_{\text{start fib}}$, and F_{max} (NAC-TTS) [101].
Fig. 39	Mean force F - h curves from <i>RheoTack</i> testing at retraction speeds of 0.01, 0.1 and 1 mm/s obtained for five different TTS samples (NAC-TTS 49.1 %) [101].
Fig. 40	F - h curves of AC- and NAC-TTS with $v_F = 54.2$ %, 51.6 % and 49.1 %, tested with retraction speed of $v_{\text{retract}} = 0.1$ mm/s with P8 [102].
Fig. 41	Starting situation of the rods P8, P5 and R5 with the corresponding displacement and inclination angles at the end of the dwell time for NAC-TTS, $v_F = 49.1$ % [102]
Fig. 42	Normalized F - h -curves (to P5) of P8, P5 and R5 for AC- (top) and NAC-TTS (bottom) with $v_F = 49.1$ % [102].
Fig. 43	State of bonding for P8 a), P5 b), and R5 c) at h_{max} (NAC-TTS, $v_F = 49.1$ % and $v_{\text{retract}} = 0.01$ mm/s) with stretching patterns of the backing layer between the TMP

	and rods, the resulting angles of the TTS between TMP and rods: α for P8, β for P5 and γ for R5, and the TTS's retraction at the TMPs bottom from initial edge of TTS R_{TTS_0} to the resulting edge of TTS R_{TTS} [102].
Fig. 44	Deformation structures as the stretching patterns of the TTS and cavity sizes observed with camera 1 under the probe rod in 90° , a) $v_{\text{retract}} = 0.01$ mm/s, b) $v_{\text{retract}} = 0.1$ mm/s, c) $v_{\text{retract}} = 1$ mm/s [101].
Fig. 45	Flow chart of the contribution to science and practice employed in the PhD. thesis [50].
Fig. A1	Strain amplitude dependent storage G' and loss moduli G'' of AC and NAC-PSAs at excitation frequencies of $\omega = 0.6, 1, 2,$ and 4 rad/s; symbols, measured data; lines, Carreau- Yasuda-like fits [99].
Fig. C1	Retraction speed dependent $F-h$ -curves of AC-TTS with resin contents of $v_F = 54.2$ %, 51.6 % and 49.1 % using P5, P8 and R5 [102].
Fig. C2	Retraction speed dependent $F-h$ -curves of NAC-TTS with resin contents of $v_F = 54.2$ %, 51.6 % and 49.1 % using P5, P8 and R5 [102].
Fig. C3	Temperature dependent loss moduli G'' (1 Hz) and loss factor $\tan(\delta)$ of AC-PSA (left) and NAC-PSA (right) with resin contents of $v_F = 54.2$ %, 51.6 % and 49.1 %; black arrow indicates ambient temperature [102]

List of Tables

Table 1	Pros and cons of PSAs that are used for TTS [35-37].
Table 2	Building blocks for silicones [35].
Table 3	Composition of PSA samples used. [94-98]
Table 4	Measured properties, determined quantities, tested samples and instruments.
Table 5	Resin content dependent thickness averages of parameter A , parameter B and diffusion coefficients D of AC- and NAC-PSAs [100].
Table 6	Retraction speed dependent compression times [102].
Table 7	Rod geometries used with their dimensions and surface roughness's (grid distance = 5 mm) [102].
Table B1	Characteristic quantities initial ion viscosity η_0^{ion} , final ion viscosity η_∞^{ion} , time $\tau_{25\%}$ at $\eta_{\tau_{25\%}}^{ion}$ and time $\tau_{63\%}$ at $\eta_{\tau_{63\%}}^{ion}$ taken from the time dependent DEA curves of AC- and NAC-PSAs for deionized water [100].
Table B2	Characteristic quantities initial ion viscosity η_0^{ion} , final ion viscosity η_∞^{ion} , time $\tau_{25\%}$ at $\eta_{\tau_{25\%}}^{ion}$ and time $\tau_{63\%}$ at $\eta_{\tau_{63\%}}^{ion}$ taken from the time dependent DEA curves of AC- and NAC-PSAs for 0.9 % NaCl solution [100].
Table B3	Resin content dependent glass temperatures T_g and CTE in the glassy state ($\alpha_{v,G}$) and liquid state ($\alpha_{v,L}$), relative free volume v_{free} and saturation levels m_∞ [100]
Table B4	Thickness and resin content dependent diffusion coefficients D of AC- and NAC-PSAs with correlation coefficients R^2 determined using parameters A , B and τ_{diff} for deionized water according to eq. 25 [100].
Table B5	Thickness and resin content dependent diffusion coefficients D of AC- and NAC-PSAs with correlation coefficients R^2 determined using parameters A , B and τ_{diff} for 0.9% NaCl solution according to eq. 25 [100].
Table B6	Thickness and resin content dependent diffusion coefficients D of AC- and NAC-PSAs with correlation coefficients R^2 determined using parameters A , B and τ_{diff} for 0.9% NaCl solution according to eq. 26 [100].
Table C1	RheoTack quantities measured with rod P8 [102].
Table C2	Resin content dependent displacements at end of dwell time h_{dwell} of AC-TTS and NAC-TTS and storage moduli [102].

Abbreviations and symbols

Abbreviations

AC	Amine compatible
API	Active pharmaceutical ingredients
CD	Controlled deformation mode
COP	Cross over point
CS	Controlled stress mode
CTE	Coefficient of thermal expansion
DEA	Dielectric analysis
EMA	European Medicines Agency
EVA	Ethylene vinyl acetate
FDA	Food and Drug Administration
IB	Isobutylene
ICH	International Council on Harmonisation of Technical Requirements for Registration of Pharmaceuticals for Human Use
IDEX	Interdigitated electrode
IP	Isoprene
LAOS	Large amplitude oscillatory shear
LVE	Linear viscoelastic region
TTS	Transdermal therapeutic systems
MAOS	Middle amplitude oscillatory shear
MN	Microneedles
NAC	Non-amine compatible
PDMS	Polydimethylsiloxane
PET	Polyethylene terephthalate
PIB	Polyisobutylene
PSA	Pressure sensitive adhesive
PU	Polyurethane
PTFE	Polytetrafluoroethylene
SAOS	Short amplitude oscillatory shear
TMP	Temperature module plate

Symbols

A	Contribution of the final ion concentration to the ion viscosity
A_{contact}	Contact area
A_{P5}	Contact area of P5
A_{P8}	Contact area of P8
A_{R5}	Contact area of R5
A_0	Pre-exponential factor
b	Distance between the electrodes
B	Doolittle constant
B'	Fractional free volume
$c_{\text{H}_2\text{O}}$	Initial water concentration
$c_{\text{H}_2\text{O}}(t)$	Time dependent water concentration
c_{ion}^0	Initial ion concentration
c_{∞}^{PSA}	Final water concentration in the PSA
C	Concentration of diffusing substance
C_1	Transition factor from linear to nonlinear viscoelastic region
C_2	Range of the transition factor
C_3	Strain amplitude dependency of G' and G'' within the nonlinear range
d_{max}	$3d_{\text{penetration}}$ = the sensitivity range of the mini IDEX sensor
d_{PSA}	Thickness of the PSA-layer
D	Diffusion coefficient
D_{con}	Contact diameter
D_{sphere}	Diameter of the sphere
D_{TMP}	TMP diameter
E_{adh}	Adhesion energy
$E_{\text{start fib}}$	Activation energy of cavity and/or fibril formation
E''	Loss modulus
f	Frequency
$F(h)$	Force
F_{max}	Maximum force
$F_{\text{start fib}}$	Initiation force of cavity and/or fibril formation
G_0	Surface energy
G	Fracture energy
G^*	Complex shear modulus
G'	Storage modulus
G'_0	Initial storage moduli

$G'_M(\gamma)$	Zero-strain modulus
$G'_L(\gamma)$	Maximum-strain modulus
G''	Loss modulus
h	Retraction displacement
h_{\max}	Retraction displacement at F_{\max}
$h_{\text{start fib}}$	Retraction displacement at $F_{\text{start fib}}$
I_1	1 st harmonic from Fourier analysis
I_3	3 rd harmonic from Fourier analysis
I_5	5 th harmonic from Fourier analysis
$I_{3/1}$	Ratio of 3 rd and 1 st harmonic from Fourier analysis
J	Flow density of diffusing substance
k_2	Constant
K_2	Constant
l	Length / thickness
M_t	Time dependent relative mass of diffusant
M_∞	Relative mass at saturation
m_∞	Saturation level of water uptake
n	Order of terms of Fourier series
n_{P8}	Normalization factor for P8
n_{R5}	Normalization factor for R5
P5	Rod with $\varnothing = 5$ mm
P8	Rod with $\varnothing = 8$ mm
Δp	Pressure difference
p_D	Penetration depth
\dot{Q}	Volume flow
R	Radius of capillary
R_{TTS}	Resulting TTS edge
$R_{TTS,0}$	Initial edge of TTS
R5	Rounded shaped rod with $\varnothing = 5$ mm and $D_{\text{sphere}} = 5$ mm
$S(\gamma_0)$	Strain stiffening ratio
S	Stiffness
$\tan(\delta)$	Loss factor
T_g	Glass transition temperature
Δt	Time difference
$T(\gamma_0)$	Shear thickening ratio
ΔV	Volume difference
w	Electrode width
x	Space coordinate

Greek symbols

α	Cone's angle
$\alpha_{L,G}$	Coefficient of thermal expansion in the glassy state, before T_g
$\alpha_{L,L}$	Coefficient of thermal expansion in the liquid state, after T_g
$\gamma_0(\omega)$	Deformation amplitude
γ_{OC}	Limit of LVE
$\dot{\gamma}$	Shear rate
$\dot{\gamma}(t)$	Time dependent shear rate
$\dot{\gamma}_0$	Shear rate amplitude
δ	Phase angle
ε''	Dielectric loss
ε_0	Dielectric constant
η	Viscosity
η_{shear}	Shear viscosity
$\eta^{\text{ion}}(f, t)$	Ion viscosity dependent on frequency or time
$\eta_{\text{rel}}^{\text{ion}}$	Normalized ion viscosity
η_0^{ion}	Constant initial ion viscosity
η_∞^{ion}	Final ion viscosity
$\eta_{\tau 25\%}^{\text{ion}}$	Ion viscosity, 25 % below η_0^{ion}
$\eta_{\tau 63\%}^{\text{ion}}$	Ion viscosity, 63 % below η_0^{ion}
$\eta'_M(\dot{\gamma})$	Zero-rate dynamic viscosity
$\eta'_L(\dot{\gamma})$	Maximum-rate dynamic viscosity
v_F	Resin content
v_{retract}	Retraction speed
v_{free}	Relative free volume
ρ_{solv}	Density of the solvent
σ	Ion conductivity
$\tau(\dot{\gamma})$	Shear stress
τ_{diff}	Diffusion time constant
$\tau_{25\%}$	Time at $\eta_{\tau 25\%}^{\text{ion}}$
$\tau_{63\%}$	Time at $\eta_{\tau 63\%}^{\text{ion}}$
ψ	Adsorption energy
ω	Angular frequency

Publications, Posters and Presentations

Publications in a context of this doctoral work:

- Michael Meurer, Roland Kádár, Esther Ramakers-van Dorp, Bernhard Möglinger, Berenika Hausnerová, **Nonlinear oscillatory shear tests of pressure-sensitive adhesives (PSAs) designed for transdermal therapeutic systems (TTS)**. *Rheol. Acta* 2021, 60, 553–570.
- Michael Meurer, Tim Prescher, Esther Ramakers-van Dorp, Bernhard Möglinger, Berenika Hausnerová, **RheoTack—An approach to investigate retraction rate dependent detaching behavior of pressure sensitive adhesives**. *J. Rheol.* 2022, 66, 505-514.
- Michael Meurer, Gatien Kamsu, Christian Dresbach, Esther Ramakers-van Dorp, Bernhard Möglinger, Berenika Hausnerová, **Rate dependent tack behavior of silicone-based pressure sensitive adhesives for transdermal therapeutic systems**. Submitted to *J. ind. Eng. Chem.* November 2023.
- Michael Meurer, Lucca Retterath, Esther Ramakers-van Dorp, Bernhard Möglinger, Berenika Hausnerová, **Effects of resin content on water diffusion in two chemically different silicone based pressure sensitive adhesives (PSA) using dielectric analysis (DEA)**. Submitted to *APL Biong*. December 2023.

Conference Publications:

- **Improved Tack-Measurements of Transdermal Therapeutic System**, *Annual European Rheology Conference*, Portoroz, Slovenia, April 2019, poster presentation.
- **Nonlinear oscillatory shear tests of Pressure Sensitive Adhesives designed for Transdermal Therapeutic Systems**, *Nordic Rheology Conference*, Gothenburg, Sweden 2019, oral presentation.
- **Large Amplitude Oscillatory Shear Tests of Pressure Sensitive Adhesives Designed for Transdermal Therapeutic Systems**, *International Congress on Rheology*, online (Rio de Janeiro, Brazil), 2020, oral presentation.
- **RheoTack - a new comprehensive tack test method for adhesive tapes**, *Times of Polymer and Composites*, Ischia, Italy 2021, oral presentation.
- **RheoTack - rate dependent tack behavior of pressure sensitive adhesives – effect of composition and probe geometry**, *20th ICEM International Conference on Experimental Mechanics*, Porto, Portugal 2022, oral presentation.

Curriculum Vitae

Date and place of birth June 9th, 1987 in Andernach, Germany
Permanent address University of Applied Sciences Bonn-Rhein-Sieg
Von-Liebig-Str. 20
D-53359 Rheinbach, Germany
Tel: (+49) 2241 865 755
E-mail: Michael.Meurer@h-brs.de

Education

since 10/2017 **Ph.D. studies at Tomas Bata University in Zlín,**
Faculty of Technology, Department of Production Engineering
09/2011 – 10/2013 **M.Sc. Applied Polymer Sciences, FH-Aachen- University of Applied Sciences,**
Department of Chemistry and Biotechnology
09/2008 – 05/2011 **B.Sc. Chemistry with material sciences at University of Applied Sciences Bonn-Rhein-Sieg,**
Department of Natural Sciences

Work experience

Since 08/2016 **Scientific assistant at University of Applied Sciences Bonn-Rhein-Sieg, Rheinbach,**
Faculty of Applied Sciences
Since 09/2017 **Management board within the TREE-institute, University of Applied Sciences Bonn-Rhein-Sieg, Rheinbach and St. Augustin**
01/2014-08/2016 **Product development engineer, AKRO-PLASTIC GmbH,**
Niederzissen, Germany

Appendix A

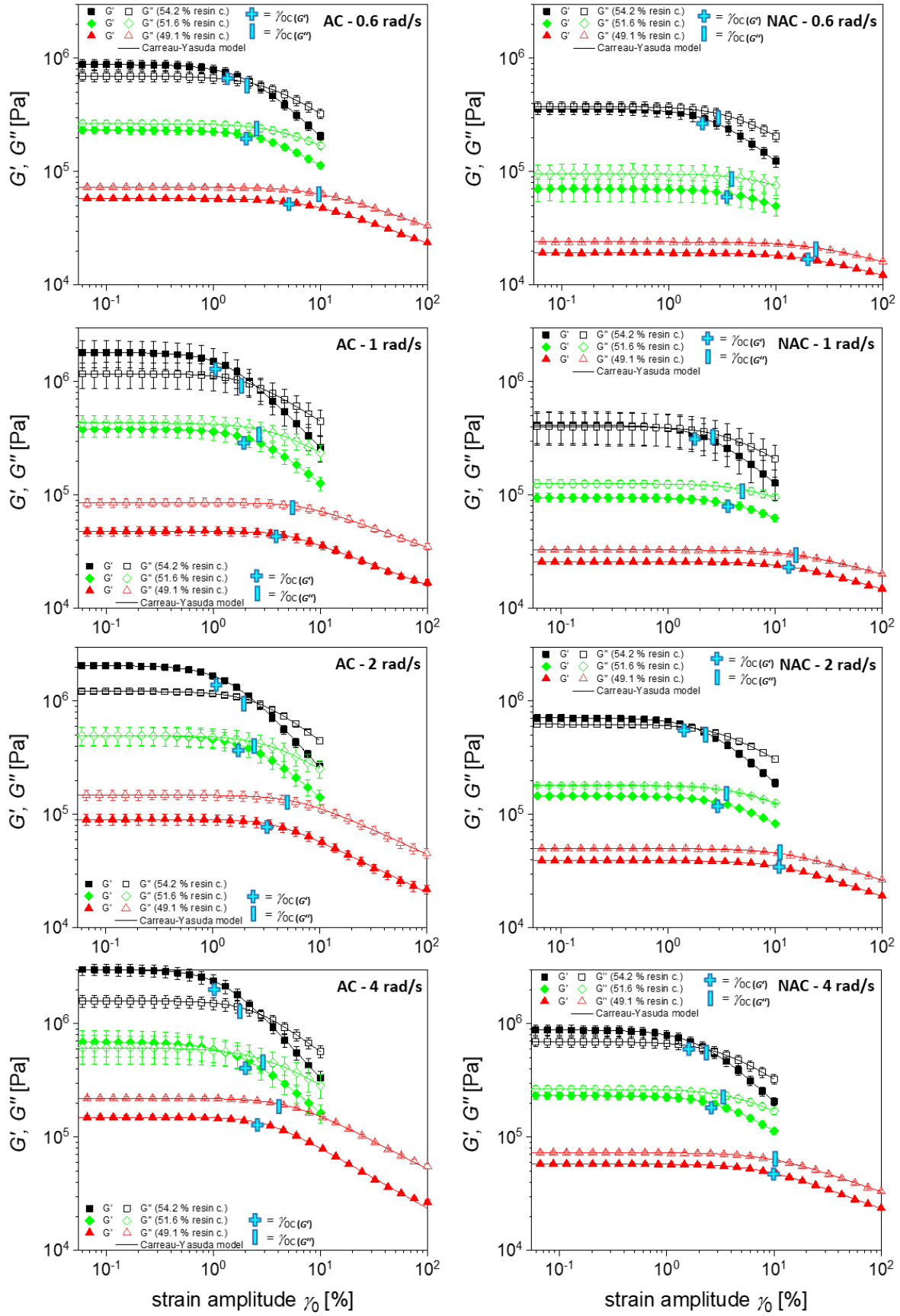


Fig. A1: Strain amplitude dependent storage G' and loss moduli G'' of AC and NAC-PSAs at excitation frequencies of $\omega = 0.6, 1, 2,$ and 4 rad/s; symbols, measured data; lines, Carreau- Yasuda-like fits [99].

Appendix B

Table B1: Characteristic quantities *initial ion viscosity* η_0^{ion} , *final ion viscosity* η_∞^{ion} , *time* $\tau_{25\%}$ at $\eta_{\tau_{25\%}}^{\text{ion}}$ and *time* $\tau_{63\%}$ at $\eta_{\tau_{63\%}}^{\text{ion}}$ taken from the time dependent DEA curves of AC- and NAC-PSAs for deionized water [100].

v_F	Amine compatible-PSA (AC) for deionized water					Non-amine compatible-PSA (NAC) for deionized water		
		$300 \mu m$	$600 \mu m$	$900 \mu m$		$300 \mu m$	$600 \mu m$	$900 \mu m$
54.2 %	η_0^{ion}	10^{11} $\Omega \cdot \text{cm}$	16 ± 3	8 ± 5	4	13 ± 2	14 ± 10	6 ± 4
	η_∞^{ion}	$10^7 \Omega \cdot \text{cm}$	32 ± 18	20 ± 10	19 ± 8	80 ± 66	35 ± 24	7 ± 5
	$\tau_{25\%}$	[s]	28 ± 13	39 ± 13	171 ± 31	43 ± 9	55 ± 17	168 ± 6
	$\tau_{63\%}$	[s]	51 ± 8	86 ± 14	244 ± 47	82 ± 2	162 ± 25	255 ± 28
51,6 %	η_0^{ion}	10^{11} $\Omega \cdot \text{cm}$	13 ± 4	17 ± 3	14 ± 11	9 ± 7	2.1 ± 0.3	9 ± 4
	η_∞^{ion}	$10^7 \Omega \cdot \text{cm}$	12 ± 11	2.4 ± 0.2	100 ± 58	3.0 ± 2.1	0.5 ± 0.3	8.1 ± 0.3
	$\tau_{25\%}$	[s]	16 ± 8	33 ± 7	115 ± 50	54 ± 2	102 ± 12	172 ± 110
	$\tau_{63\%}$	[s]	23 ± 9	66 ± 21	232 ± 41	69 ± 1	153 ± 22	276 ± 108
49.1 %	η_0^{ion}	10^{11} $\Omega \cdot \text{cm}$	10 ± 7	10 ± 6	3 ± 2	8 ± 1	9 ± 3	7 ± 3
	η_∞^{ion}	$10^7 \Omega \cdot \text{cm}$	13 ± 5	8 ± 5	4 ± 2	10 ± 3	8 ± 6	11 ± 4
	$\tau_{25\%}$	[s]	13 ± 5	32 ± 5	35 ± 9	55 ± 4	105 ± 34	572 ± 278
	$\tau_{63\%}$	[s]	23 ± 4	65 ± 15	78 ± 15	84 ± 17	260 ± 121	1105 ± 354

Table B2: Characteristic quantities *initial ion viscosity* η_0^{ion} , *final ion viscosity* $\eta_{\infty}^{\text{ion}}$, *time* $\tau_{25\%}$ at $\eta_{\tau_{25\%}}^{\text{ion}}$ and *time* $\tau_{63\%}$ at $\eta_{\tau_{63\%}}^{\text{ion}}$ taken from the time dependent DEA curves of AC- and NAC-PSAs for 0.9 % NaCl solution [100].

v_F	Amine compatible-PSA (AC) for 0.9% NaCl solution					Non-amine compatible-PSA (NAC) for 0.9% NaCl solution		
		300 μm	600 μm	900 μm		300 μm	600 μm	900 μm
54.2 %	η_0^{ion}	10^{11} $\Omega^* \text{cm}$	18 ± 3	23 ± 1	12	20 ± 4	17 ± 2	11 ± 2
	$\eta_{\infty}^{\text{ion}}$	$10^7 \Omega^* \text{cm}$	11 ± 6	6 ± 4	6 ± 4	22 ± 14	14 ± 5	9 ± 1
	$\tau_{25\%}$	[s]	18 ± 9	39 ± 10	155 ± 84	20 ± 2	79 ± 34	189 ± 70
	$\tau_{63\%}$	[s]	29 ± 13	78 ± 28	227 ± 107	53 ± 18	133 ± 49	412 ± 113
51,6 %	η_0^{ion}	10^{11} $\Omega^* \text{cm}$	9 ± 5	10 ± 5	18 ± 8	3 ± 1	10 ± 7	7 ± 5
	$\eta_{\infty}^{\text{ion}}$	$10^7 \Omega^* \text{cm}$	1.3 ± 0.6	1.1 ± 0.3	31.7 ± 29.4	1.1 ± 0.7	3.4 ± 2.6	11 ± 3
	$\tau_{25\%}$	[s]	14 ± 3	38 ± 4	77 ± 18	36 ± 14	112 ± 60	361 ± 276
	$\tau_{63\%}$	[s]	19 ± 4	60 ± 6	218 ± 80	53 ± 16	178 ± 59	578 ± 359
49.1 %	η_0^{ion}	10^{11} $\Omega^* \text{cm}$	16 ± 4	19 ± 3	5 ± 3	21 ± 2	17 ± 2	7 ± 3
	$\eta_{\infty}^{\text{ion}}$	$10^7 \Omega^* \text{cm}$	6 ± 1	7 ± 2	5 ± 4	13 ± 11	13 ± 4	6 ± 3
	$\tau_{25\%}$	[s]	7 ± 3	22 ± 6	57 ± 28	42 ± 7	188 ± 33	450 ± 244
	$\tau_{63\%}$	[s]	18 ± 2	71 ± 15	107 ± 57	55 ± 12	241 ± 51	776 ± 358

Table B3: Resin content dependent glass temperatures T_g and CTE in the glassy state ($\alpha_{v,G}$) and liquid state ($\alpha_{v,L}$), relative free volume v_{free} and saturation levels m_{∞} [100].

v_F	unit	Amine compatible-PSA (AC)			Non-amine compatible-PSA (NAC)		
		54.2 %	51. %	49.1 %	54.2 %	51. %	49.1 %
T_g (max E'')	$^{\circ}\text{C}$	-145 ± 3	-139 ± 4	-137 ± 3	-142 ± 0	-141 ± 1	-138 ± 1
T_g (max $\tan\delta$)	$^{\circ}\text{C}$	-122 ± 3	-122 ± 1	-118 ± 11	-121 ± 1	-120 ± 1	-121 ± 2
$\alpha_{v,G}$ ($T < T_g$)	$10^{-6}/\text{K}$	405 ± 42	422 ± 6	443 ± 11	399 ± 21	467 ± 11	530 ± 23
$\alpha_{v,L}$ ($T > T_g$)	$10^{-6}/\text{K}$	903 ± 76	857 ± 15	899 ± 32	882 ± 140	933 ± 8	975 ± 8
v_{free}	%	10.1 ± 2.0	9.1 ± 0.4	9.2 ± 1.1	9.8 ± 2.5	9.5 ± 0.3	9.2 ± 0.6
m_{∞}^* deionized H_2O	μg	80 ± 50	220 ± 170	230 ± 210	970 ± 270	1150 ± 760	1410 ± 570
m_{∞}^* 0.9 % NaCl-solution	μg	120 ± 70	70 ± 40	50 ± 30	470 ± 120	530 ± 290	520 ± 70

Table B4: Thickness and resin content dependent diffusion coefficients D of AC- and NAC-PSAs with correlation coefficients R^2 determined using parameters A , B and τ_{diff} for deionized water according to eq. 25 [100].

v_F	Amine compatible-PSA (AC) for deionized water					Non-amine compatible-PSA (NAC) for deionized water		
			300 μm	600 μm	900 μm	300 μm	600 μm	900 μm
54.2 %	τ_{diff}	s	333 \pm 147	1084 \pm 381	2013 \pm 441	308 \pm 10	1041 \pm 81	2625 \pm 260
	A	-	3.0 \pm 0.7	6.3 \pm 1.4	7.7 \pm 0.1	4.9 \pm 1.3	6.7 \pm 1.0	5.8 \pm 1.1
	B	$\cdot 10^{-2}$	103 \pm 5	15 \pm 2	10 \pm 4	41 \pm 13	38 \pm 4	19 \pm 8
	D	$10^{-8}\text{cm}^2/\text{s}$	122 \pm 43	144 \pm 50	168 \pm 35	119 \pm 4	141 \pm 11	126 \pm 12
	R^2_{corr}	-	0.94	0.96	0.98	0.91	0.99	0.99
51.6 %	τ_{diff}	s	149 \pm 33	598 \pm 93	1543 \pm 722	181 \pm 32	808 \pm 73	1830 \pm 426
	A	-	5.0 \pm 0.8	6.4 \pm 0.4	6.5 \pm 0.7	5.0 \pm 1.6	5.4 \pm 0.5	5.1 \pm 0.7
	B	$\cdot 10^{-2}$	45 \pm 16	14 \pm 6	13 \pm 4	60 \pm 23	20 \pm 11	44 \pm 10
	D	$10^{-8}\text{cm}^2/\text{s}$	252 \pm 50	248 \pm 37	239 \pm 112	187 \pm 24	182 \pm 17	187 \pm 47
	R^2_{corr}	-	0.99	0.98	0.90	1.00	1.00	1.00
49.1 %	τ_{diff}	s	121 \pm 32	376 \pm 19	1181 \pm 291	206 \pm 72	756 \pm 135	2023 \pm 1028
	A	-	5.0 \pm 1.1	5.2 \pm 0.3	6.0 \pm 0.2	5.3 \pm 2.5	3.5 \pm 1.5	2.2 \pm 0.2
	B	$\cdot 10^{-2}$	68 \pm 29	32 \pm 3	21 \pm 1	63 \pm 30	68 \pm 22	53 \pm 11
	D	$10^{-8}\text{cm}^2/\text{s}$	320 \pm 95	389 \pm 20	287 \pm 71	197 \pm 82	196 \pm 35	187 \pm 95
	R^2_{corr}	-	0.99	0.99	0.98	0.99	0.96	0.98

Table B5: Thickness and resin content dependent diffusion coefficients D of AC- and NAC-PSAs with correlation coefficients R^2 determined using parameters A , B and τ_{diff} for 0.9% NaCl solution according to eq. 25 [100].

v_F	Amine compatible-PSA (AC) for 0.9% NaCl-solution					Non-amine compatible-PSA (NAC) for 0.9% NaCl-solution		
			300 μm	600 μm	900 μm	300 μm	600 μm	900 μm
54.2 %	τ_{diff}	s	400 \pm 44	1253 \pm 196	2863 \pm 175	393 \pm 97	1437 \pm 81	3665 \pm 952
	A	-	6.6 \pm 0.2	5.5 \pm 1.3	6.6 \pm 1.0	6.4 \pm 1.1	6.7 \pm 0.8	6.5 \pm 0.8
	B	$\cdot 10^{-2}$	15 \pm 5	20 \pm 9	11 \pm 6	20 \pm 16	8 \pm 2	12 \pm 7
	D	$10^{-8}\text{cm}^2/\text{s}$	92 \pm 10	119 \pm 20	115 \pm 7	96 \pm 24	102 \pm 6	94 \pm 25
	R^2_{corr}	-	0.94	0.96	1.00	0.99	0.94	0.99
51,6 %	τ_{diff}	s	290 \pm 59	787 \pm 108	2938 \pm 635	316 \pm 67	1272 \pm 191	3317 \pm 800
	A	-	4.8 \pm 0.3	4.7 \pm 1.9	7.9 \pm 0.2	4.7 \pm 0.8	5.9 \pm 0.4	6.8 \pm 0.9
	B	$\cdot 10^{-2}$	22 \pm 2	23 \pm 19	5 \pm 2	26 \pm 6	22 \pm 13	12 \pm 7
	D	$10^{-8}\text{cm}^2/\text{s}$	130 \pm 30	188 \pm 25	115 \pm 25	119 \pm 26	116 \pm 16	103 \pm 26
	R^2_{corr}	-	1.00	1.00	0.96	1.00	0.99	0.99
49.1 %	τ_{diff}	s	161 \pm 39	694 \pm 229	1510 \pm 272	227 \pm 60	801 \pm 112	2209 \pm 319
	A	-	5.0 \pm 1.1	4.7 \pm 1.8	6.3 \pm 1.0	6.1 \pm 1.3	6.0 \pm 1.1	4.3 \pm 3.3
	B	$\cdot 10^{-2}$	29 \pm 12	33 \pm 20	11 \pm 1	33 \pm 27	22 \pm 15	66 \pm 23
	D	$10^{-8}\text{cm}^2/\text{s}$	235 \pm 52	227 \pm 78	222 \pm 38	170 \pm 53	184 \pm 26	151 \pm 22
	R^2_{corr}	-	1.00	1.00	0.96	0.98	0.90	0.98

Table B6: Thickness and resin content dependent diffusion coefficients D of AC- and NAC-PSAs with correlation coefficients R^2 determined using parameters A , B and τ_{diff} for 0.9% NaCl solution according to eq. 26 [100].

v_F	Amine compatible-PSA (AC) for 0,9% NaCl-solution					Non-amine compatible-PSA (NAC) for 0,9% NaCl-solution		
			300 μm	600 μm	900 μm	300 μm	600 μm	900 μm
54.2 %	τ_{diff}	s	342 \pm 107	1362 \pm 5	2845 \pm 166	391 \pm 93	1387	3290 \pm 489
	A	-	6.6 \pm 0.1	6.2 \pm 0.1	6.6 \pm 1.0	6.4 \pm 0.8	6.7	6.5 \pm 0.8
	B	$\cdot 10^{-2}$	18 \pm 7	15 \pm 0	11 \pm 6	19 \pm 16	6	12 \pm 7
	K_2	$\cdot 10^{-2}$	0 \pm 0	0 \pm 0	0 \pm 0	0 \pm 0	0.7	0 \pm 0
	D	$10^{-8} \text{cm}^2/\text{s}$	115 \pm 42	107 \pm 0	116 \pm 7	96 \pm 23	105	102 \pm 16
	R^2_{corr}	-	0.99	0.98	1.00	0.99	0.88	0.99
51,6 %	τ_{diff}	s	289 \pm 57	779 \pm 100	2806 \pm 813	316 \pm 67	1269 \pm 199	3301 \pm 803
	A	-	4.8 \pm 0.3	4.7 \pm 1.9	7.9 \pm 0.2	4.7 \pm 0.9	5.0 \pm 1.6	6.8 \pm 0.9
	B	$\cdot 10^{-2}$	22 \pm 2	23 \pm 19	9 \pm 1	26 \pm 6	22 \pm 13	12 \pm 8
	K_2	$\cdot 10^{-2}$	1.3 \pm 1.2	1.4 \pm 1.1	0.3 \pm 0.2	0 \pm 0	2.4 \pm 1.7	1.2 \pm 1.1
	D	$10^{-8} \text{cm}^2/\text{s}$	130 \pm 29	190 \pm 24	122 \pm 35	119 \pm 26	117 \pm 17	104 \pm 27
	R^2_{corr}	-	0.99	1.00	0.96	1.00	0.99	0.99
49.1 %	τ_{diff}	s	161 \pm 39	713 \pm 198	1382 \pm 427	225 \pm 59	727 \pm 8	2153 \pm 372
	A	-	5.0 \pm 1.1	4.7 \pm 1.8	6.3 \pm 1.0	4.8 \pm 2.3	6.0 \pm 1.1	4.3 \pm 2.3
	B	$\cdot 10^{-2}$	29 \pm 12	27 \pm 14	4 \pm 1	33 \pm 27	22 \pm 14	47 \pm 36
	K_2	$\cdot 10^{-2}$	2.6 \pm 2.5	1.5 \pm 1.4	0 \pm 0	3.9 \pm 3.7	0 \pm 0	1.8 \pm 1.1
	D	$10^{-8} \text{cm}^2/\text{s}$	236 \pm 53	216 \pm 58	256 \pm 88	172 \pm 54	201 \pm 2	156 \pm 27
	R^2_{corr}	-	0.99	1.00	0.96	0.98	0.92	0.98

Appendix C

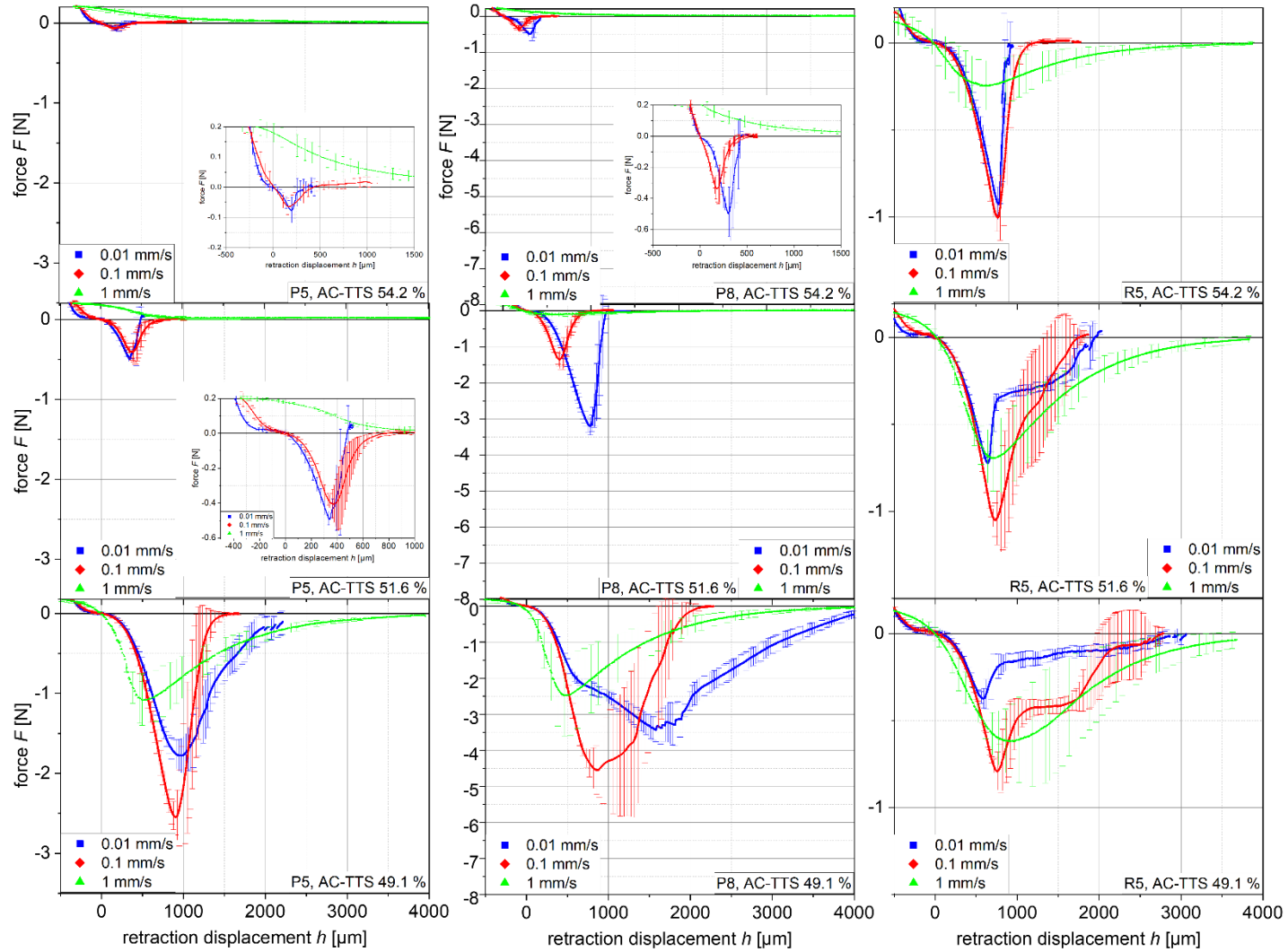


Fig. C1: Retraction speed dependent F - h -curves of AC-TTS with resin contents of $v_F = 54.2\%$, 51.6% and 49.1% using P5, P8 and R5 [102].

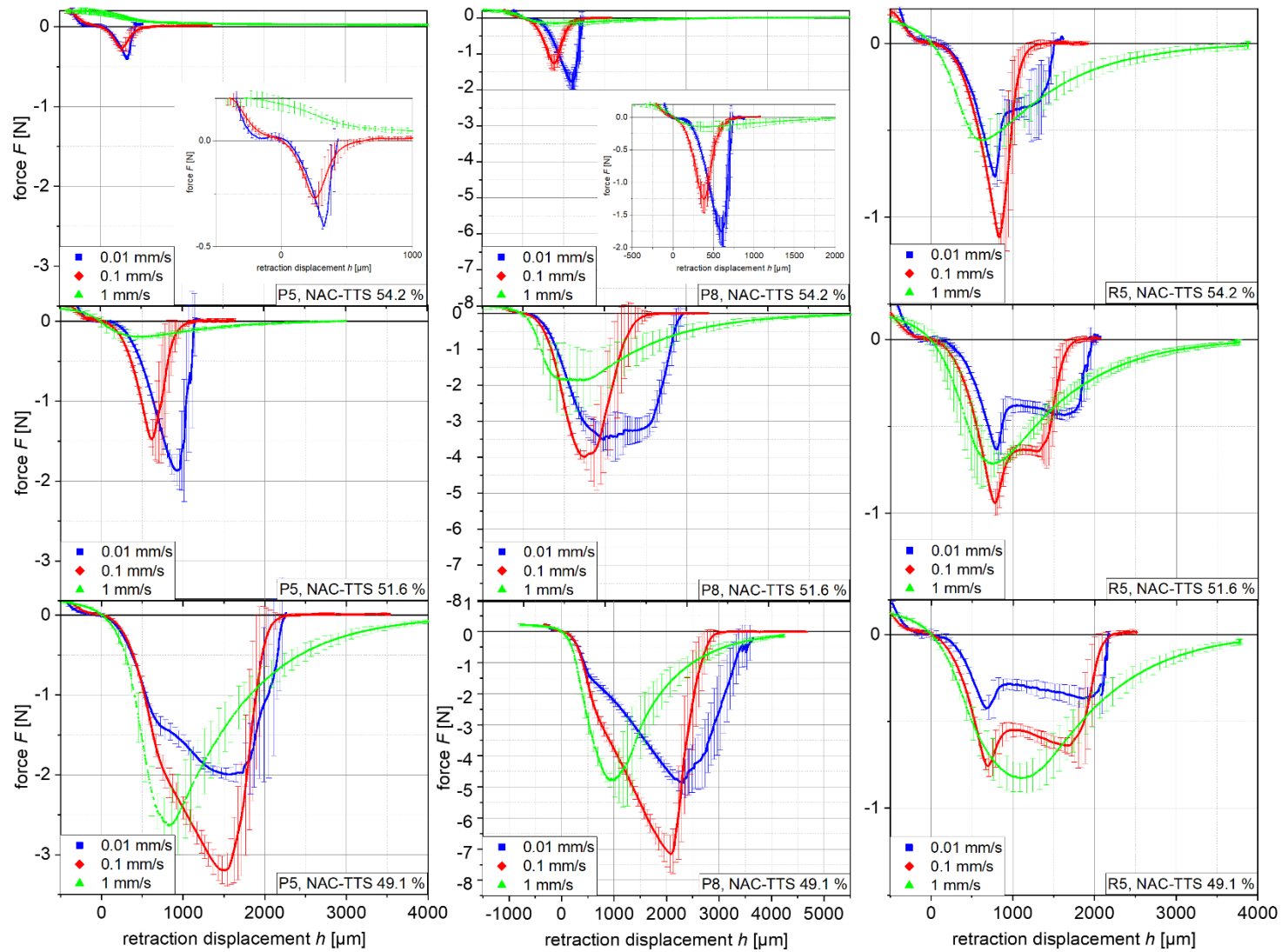


Fig. C2: Retraction speed dependent F - h -curves of NAC-TTS with resin contents of $v_F = 54.2\%$, 51.6% and 49.1% using P5, P8 and R5 [102].

Table C1: *RheoTack* quantities measured with rod P8 [102].

		AC			NAC		
		54.2	51.6	49.1	54.2	51.6	49.1
0.01 mm/s	S (mN/mm)	804 ± 124	259 ± 81	224 ± 48	273 ± 6	247 ± 112	238 ± 31
	$h_{\text{start fib}}$ (μm)	151 ± 20	272 ± 31	619 ± 93	252 ± 40	730 ± 63	535 ± 61
	$F_{\text{start fib}}$ (N)	0.1 ± 0.0	0.3 ± 0.1	2.1 ± 0.3	0.2 ± 0.0	3.0 ± 0.3	1.5 ± 0.2
	$E_{\text{start fib}}$ (μJ)	9 ± 3	37 ± 9	548 ± 178	19 ± 7	754 ± 131	269 ± 53
	h_{max} (μm)	304 ± 28	809 ± 65	1752 ± 114	615 ± 52	1073 ± 116	2421 ± 264
	F_{max} (N)	0.6 ± 0.1	3.3 ± 0.2	3.6 ± 0.4	1.7 ± 0.2	3.5 ± 0.4	5.0 ± 0.3
	E_{adh} (μJ)	89 ± 22	1223 ± 102	6870 ± 215	493 ± 83	4077 ± 386	9290 ± 1077
0.1 mm/s	S (mN/mm)	1334 ± 88	610 ± 115	396 ± 69	565 ± 81	461 ± 74	431 ± 33
	$h_{\text{start fib}}$ (μm)	106 ± 16	150 ± 12	723 ± 63	132 ± 33	209 ± 25	649 ± 74
	$F_{\text{start fib}}$ (N)	0.1 ± 0.0	0.2 ± 0.0	4.0 ± 0.2	0.2 ± 0.0	0.3 ± 0.0	2.6 ± 0.2
	$E_{\text{start fib}}$ (μJ)	8 ± 3	18 ± 3	989 ± 158	16 ± 6	48 ± 7	551 ± 128
	h_{max} (μm)	211 ± 26	399 ± 25	898 ± 139	375 ± 29	777 ± 101	2121 ± 129
	F_{max} (N)	0.4 ± 0.1	1.4 ± 0.2	4.7 ± 0.6	1.3 ± 0.2	4.1 ± 0.2	7.3 ± 0.7
	E_{adh} (μJ)	74 ± 18	381 ± 64	4622 ± 1357	335 ± 57	2666 ± 593	10176 ± 1233
1 mm/s	S (mN/mm)	-	1085 ± 91	944 ± 52	1275 ± 67	1208 ± 83	1228 ± 45
	$h_{\text{start fib}}$ (μm)	-	81 ± 21	129 ± 14	-	107 ± 18	527 ± 42
	$F_{\text{start fib}}$ (N)	-	0.1 ± 0.0	0.2 ± 0.1	-	0.20 ± 0.06	3.0 ± 0.3
	$E_{\text{start fib}}$ (μJ)	-	3 ± 1	22 ± 7	-	18 ± 6	612 ± 118
	h_{max} (μm)	-	351 ± 79	550 ± 12	385 ± 28	505 ± 42	1016 ± 108
	F_{max} (N)	-	0.1 ± 0.0	2.5 ± 0.3	0.17 ± 0.03	1.9 ± 0.3	4.8 ± 0.2
	E_{adh} (μJ)	-	131 ± 74	3523 ± 866	169 ± 31	2797 ± 671	7263 ± 1190

4

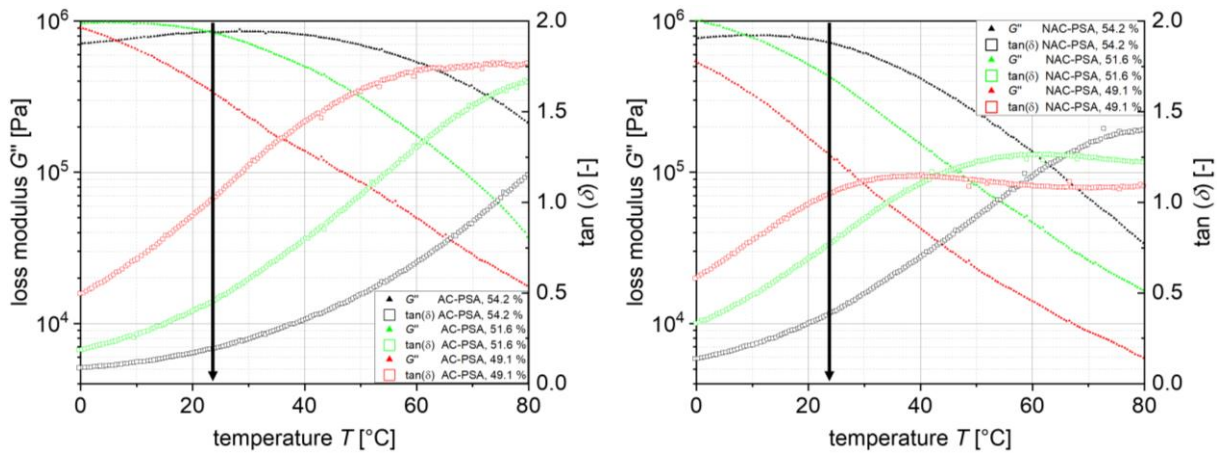


Fig. C3: Temperature dependent loss moduli G'' (1 Hz) and loss factor $\tan(\delta)$ of AC-PSA (left) and NAC-PSA (right) with resin contents of $\nu_F = 54.2 \%$, 51.6% and 49.1% ; black arrow indicates ambient temperature [102].

Table C2: Resin content dependent displacements at end of dwell time h_{dwell} of AC-TTS and NAC-TTS and storage moduli [102].

PSA type	Resin content	h_{dwell} (P8)	h_{dwell} (P5)	h_{dwell} (R5)	G' (1 Hz)
	%	μm	μm	μm	kPa
AC	49.1	209 \pm 31	318 \pm 25	436 \pm 35	330
	51.6	172 \pm 18	250 \pm 23	381 \pm 26	1,950
	54.2	124 \pm 20	234 \pm 20	345 \pm 16	4,300
NAC	49.1	205 \pm 28	320 \pm 20	435 \pm 24	120
	51.6	186 \pm 20	289 \pm 17	408 \pm 15	570
	54.2	164 \pm 14	246 \pm 16	374 \pm 25	2,000